Delft University of Technology
Faculty of Electrical Engineering,
Mathematics and Computer Science
Mekelweg 4
2628 CD Delft

THESIS

Design of a Wideband Wide-Scan Connected Slot Array Antenna Using Artificial Dielectrics.

Alexander J. van Katwijk

November 19, 2018 - August 29, 2019

Design of a Wideband Wide-Scan Connected Slot Array Antenna Using Artificial Dielectrics.

Copyright © 2019 Alexander J. van Katwijk

All rights reserved.

Acknowledgments

I would like to thank my supervisor, dr. Daniele Cavallo, for introducing me to this subject, which captured my interest. Your guidance and insight made this thesis possible, and working together has inspired me to seek further knowledge in this field.

My gratitude also goes to Prof. dr. Andrea Neto, for providing a place in this group for me to do my thesis. The atmosphere in this group makes it a great place to work, and the people in it make me look forward to spending the next four years here. My thanks also goes to Kevin and Cyrus, with whom I had a lot of fun in the students room, and to the other students in the student room, for providing an environment where we could also work hard.

Janine, thank you, I love you.

Finally, I would like to thank my parents for their love and support. Thank you for always supporting my decisions. I truly cannot wish for better parents.

Design of a Wideband Wide-Scan Connected Slot Array Antenna Using Artificial Dielectrics

by

Alexander Jacob van Katwijk

to obtain the degree of Master of Science
at the Delft University of Technology,
to be defended publicly on Thursday August 29, 2019 at 13:00.

Student number:	4334264
Project duration:	November 19, 2018 - August 29, 2019
Thesis committee:	Prof.dr. Andrea Neto
	Dr. Daniele Cavallo
	Dr. Masoud Babaie

Contents

Chapter 1

Introduction

1.1 Antenna Systems for Space-limited Applications

Wide-band wide-scan have been of increasing interest over the past decades, for both defense and commercial applications. As the need for bandwidth and the density of electronic systems increase there is a large push towards antennas that can offer multi-octave bandwidths while also offering wide scan capabilities. Communications systems must support an increasing number functionalities and protocols within a single module, while also offering increased data throughput and directionality. Similarly, military systems such as naval platforms must support an enormous range of different functionalities, and efforts are made to integrate these functionalities into fewer ultra-wideband systems.

In the past, these systems are each implemented using separate antenna systems, which each have their own limited bandwidth. The inclusion of many of these systems together, along with high-power radar systems introduces significant interference between the systems.

In space- and weight-limited applications such as satellite systems or airborne platforms, the integration of several of these into a single wide-band wide-scan antenna array can significantly reduce the size and weight of the RF front end.

1.2 State of the Art

Several different concepts have been proposed to realize wide-band wide-scan antenna arrays. These concepts include Vivaldi [1–3], stacked patches [4], stacked discs [5], double dipoles [6]. There is also an increasing interest into possible practical implementations of the theoretical current sheet array concept proposed by Wheeler [7]. Proposed implementations are largely based on the use of tightly coupled antennas using various base elements such as dipoles [8–11], octagonal ring elements [12], non-symmetric ball-and-cup dipoles [13], and connected slots [14]. Many of these arrangements require a balun to implement the transition from a balanced antenna element to an unbalanced feeding line, which is often bulky and limits the bandwidth of the array. [15]

Several of these different approaches use vertical elements to enable the improvement of bandwidth by offering a third dimension (depth). Fig. 1.1 shows such an arrangement, where 324 vertical antenna elements are placed in an egg-crate arrangement to form an array. This means that they are unsuitable for conformal installations and are costly and complex to fabricate. The use of planar technology enables a reduction in cost, complexity, weight and size of the antenna array. The connected slot array technology proposed in [16] enables the development of planar arrays using PCB technology and greatly simplifies fabrication due to their planar design. The bandwidth shown for backed connected slots is only 40% [16], but this can be improved through the use of an impedance transformation [14]. The constant current distribution is highlighted in Fig. 1.2, where the current distribution of resonant slots and those of connected slots are illustrated.

The use of this impedance transformation improves the bandwidth as well the front-to-back ratio of the antenna by offering a denser dielectric above the radiating element, meaning most of

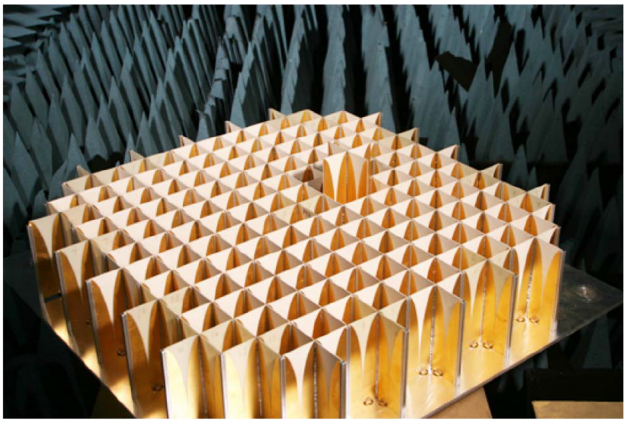

Figure 1.1: A 324-element Vivaldi antenna array [3].

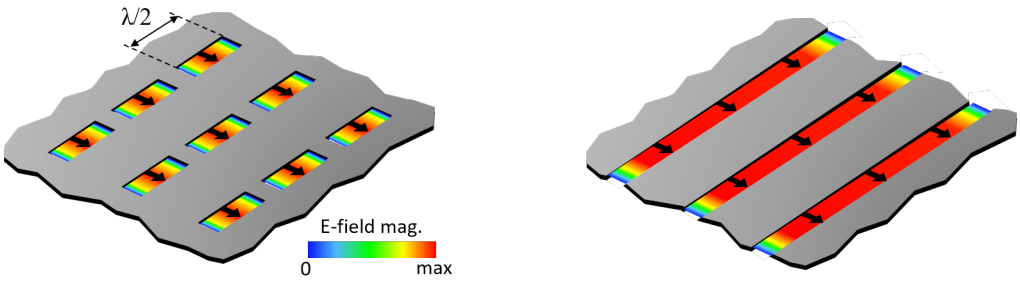

Figure 1.2: Illustration of the current distribution in (a) resonant and (b) connected slots.

the power is radiated into the dielectric found above the antenna. This allows a reduction of the distance to the backing reflector without significantly reducing bandwidth, which in turn means that the feeding network can be implemented using vias. However, this dielectric superstrate supports surface waves, which is illustrated in Fig. **??**. These surface waves can be avoided by realizing an ideal substrate that has a refractive index that decreases with scan angle such that this critical angle is never achieved. The high refraction index for normal incidence offers the antenna a high-permittivity superstrate, while the low refractive index for high scan angles prevents surface waves. This property is not available in current homogeneous materials, but it can be realized using artificial dielectrics.

This effect is realized by using a planar array of square metal patches [17], of which the behavior of the refractive index as a function of incidence angle is shown in Fig. 1.3. As such, these artificial dielectric layers (ADLs) effectively implement this ideal superstrate, as illustrated in Fig. **??**. An additional advantage of the use of the combination of connected arrays and the square metal patch-based artificial dielectric is that there are analytical expressions for both of them. These allow simulation of the structures in a fraction of the time that it would take in commercial solvers, facilitating a rapid design process.

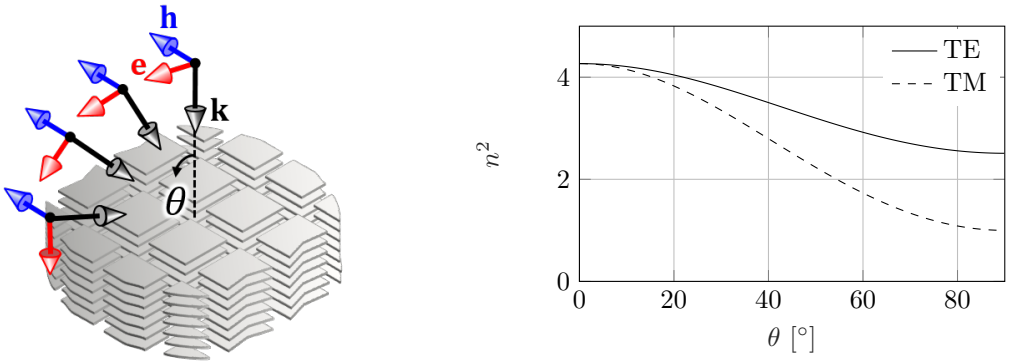

Figure 1.3: Refractive index of an ADL for TE and TM incidence at angles from 0 to 90 degrees.

Figure 1.4: Illustration of the enhancement of the front-to-back ratio using (a) homogeneous dielectrics and (b) an artificial dielectric superstrate.

1.3 Objectives of the Project

The main goal of this project is to design an antenna array with a 5:1 −10 dB bandwidth, with the ability to scan up to 60°. The antenna array is to consist of an array of connected slots, of which the bandwidth will enhanced using a superstrate based on ADLs. The ADL superstrate will implement a multisection impedance transformation to provide a smooth transition from the impedance of the feeding network to that of free space. The design is done using the analytical formulations available in [16, 18–21], which are implemented in a MATLAB tool to enable rapid iteration of various designs.

To rapidly develop ADL-based impedance transformers and investigate the effects of adjustments to its design parameters, it is useful to be able to synthesize ADLs automatically. As such, a synthesis process must be developed to select the parameters of an ADL slab such that it represents a certain given impedance. This can then be used to implement the sections of the multisection impedance transformer.

The connected array of slots must be designed such that it realizes the desired bandwidth when combined with the impedance transformer. For this, the impact of the design parameters of the slots must be investigated. Using this impact, the performance of the array when scanning to a given angle is studied and optimized. The analytical solution of the connected array of slots is valid only for a single-polarized array. Therefore, the design must be extended to dual-polarized operation using a commercial solver.

Several restrictions on the fabrication process are present, and the impact of each must be studied. The problems that arise from these restrictions must be detailed and solved. The analytical model of the ADLs must be extended to enable introduction of realistic materials in the design process, which will enable the synthesis process to account for their impact. The effect of tolerances in the manufacturing process must be studied and its effect on the array quantified.

A feeding network must be designed that supports the 5:1 bandwidth of the connected array of slots, while guiding power from a feeding port in the backing reflector plane to the feeding point

in the plane of the slots. This network must adhere to the restrictions imposed on the fabrication process.

1.4 Outline of the Thesis

This thesis consists of 6 chapters:

- Chapter 1 gives an introduction into the subject and provides the motivation for this project.
- Chapter 2 shows the analytical expressions that are used to simulate the connected array of slots, as well as those used to simulate the ADLs. These expressions are then combined to form a model for the combination of the two. The implementation of these equations is validated using a commercial solver for the connected array and ADLs separately, as well as when they are combined.
- Chapter 3 describes the impedance transformation that is to be placed over the slots. Several common impedance transformations are discussed, and the process used to design a set of ADLs such that they implement this impedance transition is detailed. An example is given, which shows the accuracy of the developed method.
- Chapter 4 gives the steps to design a wideband wide-scan connected slot antenna array. The free parameters of the impedance transformation and their impact are discussed, after which the design of the unit cell of the slot is shown. The effect of scanning this array is shown, and the extension to a dual-polarized design is given.
- Chapter 5 shows the impact of the limitations imposed by the fabrication of the array on its performance. The effect of realistic materials on the ADL and its transmission line model are shown. A study is done of the tolerances on the manufacturing process, and their impact on the performance of the designed array. The feeding network is designed, and a final design is presented. The performance of this final design is shown using various metrics.
- Chapter 6 finishes the report by providing conclusions and suggestions for future work.

Chapter 2

Connected Arrays and Artificial Dielectrics

This chapter will detail the analytical formulations used for the design of the antenna array. First, the equations used for the Connected Arrays are given in Section 2.1. Next, the model used to analyze the Artificial Dielectric Layers (ADLs) is given in Section 2.2. Finally, the two are combined in Section 2.3.

2.1 Connected Arrays

The connected array antenna is modeled using an analytical solution for the input impedance of the connected slot element in a doubly infinite periodic environment. Such an array is shown in Fig. 2.1 and consists of an infinite number of slots in y, periodically fed and extending infinitely in the x-direction. The active input impedance of a connected array of x-oriented slots is given in [22] to be

$$z_{slot} = -\frac{1}{d_x} \sum_{m_x=-\infty}^{\infty} \frac{\mathrm{sinc}^2(k_{xm}\delta_s/2)}{D_\infty(k_{xm})}, \tag{2.1}$$

which is an infinite sum of Floquet modes that accounts for the periodicity along the x-axis. The values k_{xm} and k_{ym} represent the Floquet wavenumbers of the slots and are given by

$$k_{xm} = k_{x0} - \frac{2\pi m_x}{d_x} \tag{2.2}$$

where $k_{x0} = k_0 \sin\theta \cos\phi$, k_0 is the free-space wavenumber and θ and ϕ indicate the scan angles.

D_∞ is the transverse connected array Green's function [22] that accounts for the infinite periodicity of the slots in the y-direction and the stratification along z, and is given by a summation of Floquet modes as

$$D_\infty(k_{xm}) = \frac{1}{d_y} \sum_{m_y=-\infty}^{\infty} G_{xx}(k_{xm}, k_{ym}) J_0\left(\frac{k_{ym} w_s}{2}\right), \tag{2.3}$$

where

$$k_{ym} = k_{y0} - \frac{2\pi m_y}{d_y} \tag{2.4}$$

with $k_{y0} = k_0 \sin\theta \sin\phi$. In (2.3), J_0 is a Bessel function of the 0th order, which is the Fourier transform of the edge-singular distribution of the magnetic current along the slot. G_{xx} is the spectral Green's function accounting for the vertical stratification.

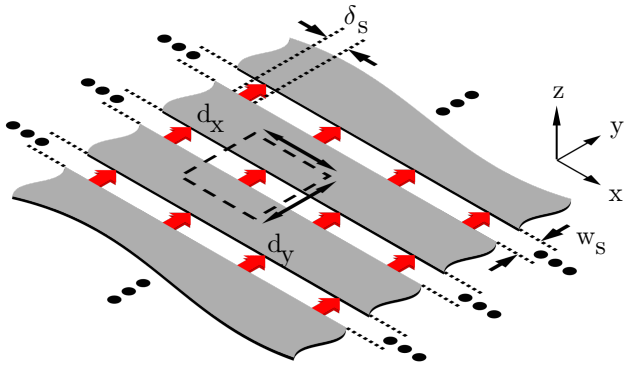

Figure 2.1: Illustration of an infinite array of infinitely long slots. The slots are infinitely long in the x-direction and have a width of w_s. They are fed periodically with a period of d_x, where each feed is δ_s wide. There are an infinite number of slots placed at a distance d_y from each other.

The spectral Green's function relates the radiated field with the magnetic currents present on the slot, where the xx-component gives the x-component of the field radiated by x-oriented elementary magnetic dipoles. It is assumed that the slot is narrow, and thus there are only x-oriented magnetic currents. G_{xx} depends on the stratification above and below the slot and is given by [23]

$$\begin{aligned} G_{xx}(k_x,k_y) &= G_{xx,up}(k_x,k_y) + G_{xx,down}(k_x,k_y) \\ &= -\frac{I_{TE,up}(k_x,k_y)k_x^2 + I_{TM,up}(k_x,k_y)k_y^2}{k_\rho^2} - \frac{I_{TE,down}(k_x,k_y)k_x^2 + I_{TM,down}(k_x,k_y)k_y^2}{k_\rho^2}, \end{aligned} \tag{2.5}$$

where I_{TE} and I_{TM} are the currents in the transmission line model representing the stratified medium above and below the slot plane and $k_\rho^2 = k_x^2 + k_y^2$. The currents are found by determining the input impedance of this transmission line of the stratification above and below the slot. The currents are given by

$$I_{TE} = \frac{1}{Z_{up,TE}} + \frac{1}{Z_{down,TE}} \tag{2.6}$$

$$I_{TM} = \frac{1}{Z_{up,TM}} + \frac{1}{Z_{down,TM}}, \tag{2.7}$$

where $Z_{up/down,TE/TM}$ are found by determining the input impedance of the given stratification for the given polarization.

Validation

To ensure the correct implementation of the equations given above, they are validated by checking the results against the results obtained using a commercial solver. Two scenarios are analyzed, one with a slot in free space, and one with a slot above a quarter-wave backing reflector. Figures 2.2 and 2.3 show that the result of the analytical implementation is very close to those obtained using CST. The dimensions used in both simulations are shown in Table 2.1 and they are given in terms of the wavelength λ_0, which corresponds to the frequency f_0.

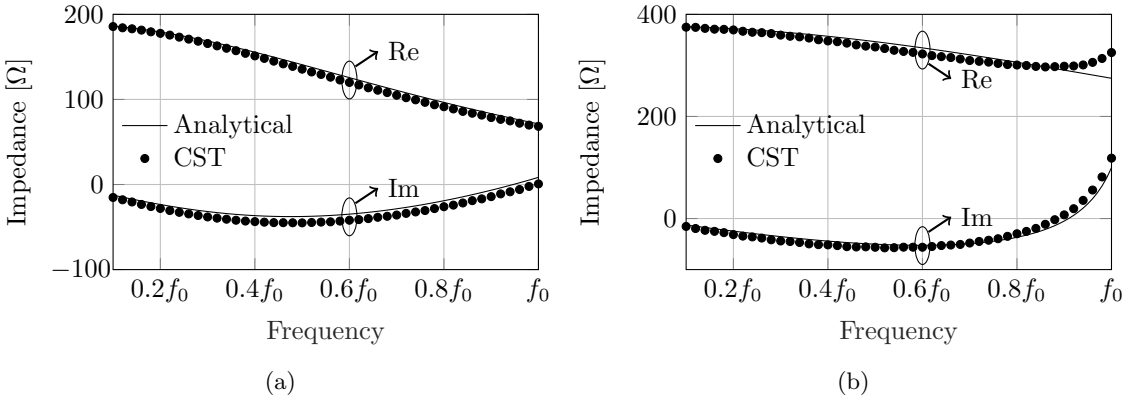

Figure 2.2: Analytical results of an infinite array of slots in free space, compared to those obtained using CST. (a) Broadside and (b) Scanning to 60°. Slot parameters are shown in Table 2.1.

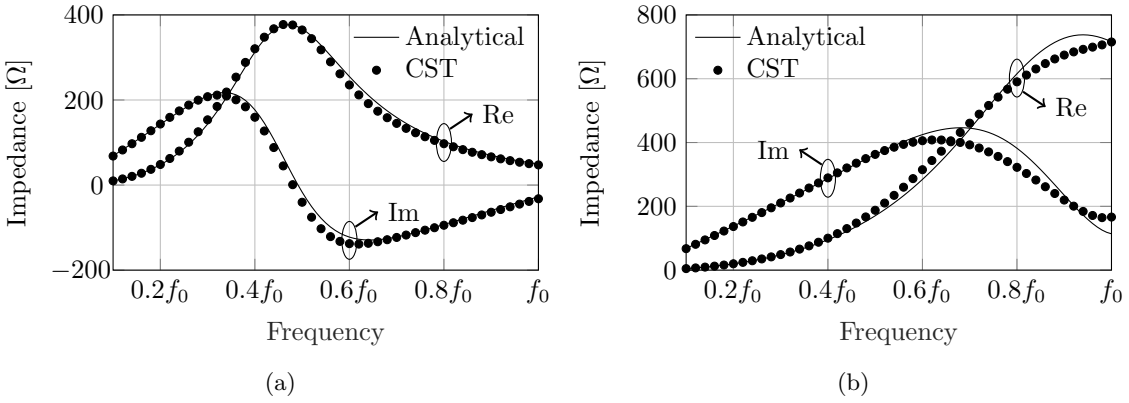

Figure 2.3: Analytical results of an infinite array of slots with a backing reflector, compared to those obtained using CST. (a) Broadside and (b) Scanning to 60°. Slot parameters are shown in Table 2.1.

Table 2.1: Parameters used for validation of implementation connected slot equations.

Parameter	Value	Description
d_x	$0.5\lambda_0$	Unit cell size
d_y	$0.5\lambda_0$	Unit cell size
w_s	$0.1\lambda_0$	Slot width
δ_s	$0.1\lambda_0$	Feed length
h_{BR}	$0.25\lambda_0$	Backing reflector distance

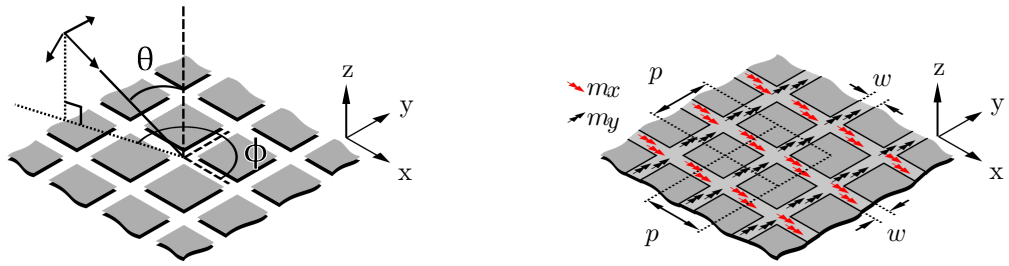

(a) (b)

Figure 2.4: Single layer of infinitely periodic square metal patches, with (a) plane wave incidence and (b) equivalent problem with geometric parameters.

2.2 Artificial Dielectrics

The transmission line model used to simulate the ADLs was developed over multiple papers. First, a single layer under plane wave incidence was analyzed in [18]. Next, multiple aligned layers were described in [19], which was then extended to non-aligned layers in [24], [20]. Finally, the formulation for non-periodic layers was given in [21]. This order will be kept in this section, where the derivation for the single layer is first given, which is then extended to multiple non-aligned, non-periodic layers.

Single Metal Layer

The analysis of the behavior of a stack of Artificial Dielectric Layers (ADLs) starts with a single layer. An analytical solution for a periodic array consisting of thin metal patches was derived in [18]. Since the full derivation of the analytical solution is available in [18] and [24], this section will only very briefly show the steps of the derivation and the relevant equations.

Fig. 2.4a shows the initial problem of a wave incident on a sheet of metal patches, characterized by a magnetic field $\mathbf{h}_i$. By applying the equivalence theorem, equivalent electric and magnetic current densities $\mathbf{j}_0$ and $\mathbf{m}_0$ can be placed in the gaps between the patches. The gaps can be filled with perfectly electric conductor (PEC), resulting in Fig. 2.4b, where only the magnetic currents are present. The electric currents do not radiate in the presence of this PEC and can be neglected. Due to the continuity of the electric field on the array plane, the electric field above and below the plane are equal, that is, $\mathbf{e}^+ = \mathbf{e}^-$. Therefore the magnetic currents above and below the plane are given by $\mathbf{m}_0^+ = \mathbf{e}^+ \times \hat{\mathbf{z}}$ and $\mathbf{m}_0^- = \mathbf{e}^- \times (-\hat{\mathbf{z}})$, which yields $\mathbf{m}_0^+ = -\mathbf{m}_0^- = \mathbf{m}_0$.

Due to the continuity of the magnetic field, the field $\mathbf{h}^+$ just above the layer and the field $\mathbf{h}^-$ just below are equal:

$$\mathbf{h}^+ = \mathbf{h}^- \,. \tag{2.8}$$

The field $\mathbf{h}^+$ is the sum of the incident, reflected field and the field scattered by the magnetic currents above the layer. The field $\mathbf{h}^-$ is only given by the field scattered by the current below the layer. Thus, (2.8) becomes

$$\mathbf{h}_{\text{scatt}}\{\mathbf{m}_0\} + (1+\Gamma)\mathbf{h}_i = \mathbf{h}_{\text{scatt}}\{-\mathbf{m}_0\}, \tag{2.9}$$

where Γ is the reflection coefficient of the magnetic field and is equal to 1 for PEC. By expressing the scattered field as a convolution, one can write

$$2\mathbf{m}_0(\rho) * \mathbf{g}_{\text{PEC}}(\rho) = -2\mathbf{h}_i, \tag{2.10}$$

where $\mathbf{g}_{\text{PEC}}$ is the dyadic Green's function in the presence of a PEC plane and $\rho = (x, y)$ is a point on the $z = 0$ plane. Applying the image theorem and indicating with $\mathbf{g}_{\text{fs}}$ the free-space Green's

function, one obtains

$$4\mathbf{m}_0(\rho) * \mathbf{g}_{\text{fs}}(\rho) = -2\mathbf{h}_i\,. \tag{2.11}$$

To find the unknown magnetic current density $\mathbf{m}_0$, two basis functions are chosen for both the x-slot and for the y-slot. The magnetic current can be written in terms of these basis functions as

$$\mathbf{m}_0(\rho) = \left[v_1 f_1(\rho) + v_3 f_3(\rho)\right]\hat{\mathbf{x}} + \left[v_2 f_2(\rho) + v_4 f_4(\rho)\right]\hat{\mathbf{y}}, \tag{2.12}$$

where

$$f_1(\rho) = m_t(y)e^{-jk_{x0}x} \tag{2.13}$$

$$\begin{aligned} f_3(\rho) = m_t(y)\big(&- \left(e^{jk_0x} + \Gamma e^{-jk_0x}\right)\text{rect}_{[-p/2,-w/2)}(x) \\ &+ \left(e^{-jk_0x} + \Gamma e^{jk_0x}\right)\text{rect}_{(w/2,p/2]}(x) + C\big) \end{aligned} \tag{2.14}$$

with

$$m_t(x) = \frac{1}{w}\text{rect}_{[-w/2,w/2]}(x) \tag{2.15}$$

$$\Gamma = -e^{-jk_0p} \tag{2.16}$$

$$C = \frac{2}{w}\left(e^{-jk_0w/2} + \Gamma e^{jk_0w/2}\right). \tag{2.17}$$

Here, f_3 is chosen such to satisfy the Kirchhoff law at the junction between the slots. Its Fourier transform is known in closed form. The transverse distribution in (2.15) is chosen as constant for the sake of simplicity of formulation. The functions f_2 and f_4 are found by interchanging x and y in f_1 and f_3, respectively.

To find the unknowns v_i, (2.12) is substituted in (2.11), after which Galerkin projection is applied to find a linear system of equations

$$\left.\begin{aligned} v_1Y_{11} + v_2Y_{12} + v_3Y_{13} + v_4Y_{14} &= i_1 \\ v_1Y_{21} + v_2Y_{22} + v_3Y_{23} + v_4Y_{24} &= i_2 \\ v_1Y_{31} + v_2Y_{32} + v_3Y_{33} + v_4Y_{34} &= i_3 \\ v_1Y_{41} + v_2Y_{42} + v_3Y_{43} + v_4Y_{44} &= i_4 \end{aligned}\right\} \mathbf{Yv} = \mathbf{i}\,. \tag{2.18}$$

In this set of equations, Y_{pq} are the mutual admittances given by the projection of the field resulting from the p-th basis function onto the q-th test function, so

$$Y_{pq} = \langle \mathbf{f}_p(\rho) * \mathbf{g}(\rho), \mathbf{f}_q(\rho)\rangle\,, \tag{2.19}$$

where $\mathbf{g} = 4\mathbf{g}_{\text{fs}}$ and the notation $\langle\cdot,\cdot\rangle$ refers to the projection operator. The currents are given by the projection of the incident field onto the q-th test function, so $i_q = \langle 2\mathbf{h}_i(\rho), \mathbf{f}_q(\rho)\rangle$.

To more easily solve the convolution integrals present in (2.19), the projection is expressed in the spectral domain as

$$Y_{pq} = -\frac{1}{p^2}\sum_{m_x=-\infty}^{\infty}\sum_{m_y=-\infty}^{\infty}\mathbf{F}_p(k_{xm}, k_{ym})\mathbf{G}(k_{xm}, k_{ym})\cdot\mathbf{F}_q^*(-k_{xm}, -k_{ym})\,. \tag{2.20}$$

Since the projection of the field radiated by f_1 on the odd function f_3 is zero, the terms $Y_{13} = Y_{31} = 0$ and, similarly, $Y_{24} = Y_{42} = 0$. The projection $i_{3,4}$ of the incident plane wave $\mathbf{h}_i$ onto the odd functions $f_{3,4}$ are also zero, so $i_3 = i_4 = 0$. The linear equations in (2.18) can be written in matrix form as

$$\begin{bmatrix} Y_{11} & Y_{12} & 0 & Y_{14} \\ Y_{21} & Y_{22} & Y_{23} & 0 \\ 0 & Y_{32} & Y_{33} & Y_{34} \\ Y_{41} & 0 & Y_{43} & Y_{44} \end{bmatrix} \cdot \begin{bmatrix} v_1 \\ v_2 \\ v_3 \\ v_4 \end{bmatrix} = \begin{bmatrix} i_1 \\ i_2 \\ 0 \\ 0 \end{bmatrix} \tag{2.21}$$

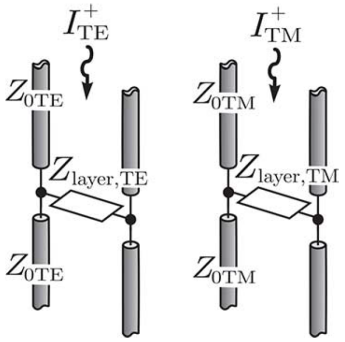

Figure 2.5: Equivalent transmission line models for TE and TM incidence on a single layer of infinitely periodic metal patches.

which is reduced to $\mathbf{Y}_{red}\mathbf{v} = \mathbf{i}$ as

$$\begin{bmatrix} Y_{11} - \frac{Y_{41}Y_{14}Y_{33}}{Y_{33}^2 - Y_{34}Y_{43}} & Y_{12} - \frac{Y_{32}Y_{43}Y_{14}}{Y_{33}^2 - Y_{34}Y_{43}} \\ Y_{21} - \frac{Y_{41}Y_{23}Y_{34}}{Y_{33}^2 - Y_{34}Y_{43}} & Y_{12} - \frac{Y_{32}Y_{23}Y_{33}}{Y_{33}^2 - Y_{34}Y_{43}} \end{bmatrix} \cdot \begin{bmatrix} v_1 \\ v_2 \end{bmatrix} = \begin{bmatrix} i_1 \\ i_2 \end{bmatrix}. \tag{2.22}$$

Applying the rotation matrix $\mathbf{R}$ gives the final notation

$$\mathbf{R}\mathbf{Y}_{\mathrm{red}}\mathbf{R}^T\mathbf{R}\begin{bmatrix} v_1 \\ v_2 \end{bmatrix} = \mathbf{R}\begin{bmatrix} v_1 \\ v_2 \end{bmatrix} \tag{2.23}$$

$$\mathbf{Y}_{\mathrm{TETM}}\begin{bmatrix} v_{\mathrm{TE}} \\ v_{\mathrm{TM}} \end{bmatrix} = \begin{bmatrix} i_{\mathrm{TE}} \\ i_{\mathrm{TM}} \end{bmatrix} \tag{2.24}$$

where

$$\mathbf{R} = \begin{bmatrix} \cos\phi & \sin\phi \\ -\sin\phi & \cos\phi \end{bmatrix} \tag{2.25}$$

and

$$\mathbf{Y}_{\mathrm{TETM}} = \mathbf{Y}_{\mathrm{TL}} + \mathbf{Y}_{\mathrm{ADL}} = \begin{bmatrix} \frac{2}{Z_{0\mathrm{TE}}} & 0 \\ 0 & \frac{2}{Z_{0\mathrm{TM}}} \end{bmatrix} + \begin{bmatrix} jB_{\mathrm{SL}}\left(1 - \frac{\sin^2\theta}{2}\right) & 0 \\ 0 & jB_{\mathrm{SL}} \end{bmatrix}. \tag{2.26}$$

The impedances in $\mathbf{Y}_{\mathrm{TL}}$ are the TE and TM characteristic impedances of the hosting medium of the ADL with relative permittivity ε_r, given by $Z_{0\mathrm{TE}} = \zeta_d k_0/k_{z0}$ and $Z_{0\mathrm{TM}} = \zeta_d k_{z0}/k_0$, with $k_{z0} = k_0\cos\theta$ and $\zeta_d = 120\pi/\sqrt{\varepsilon_r}$. The factor 2 in the matrix $\mathbf{Y}_{\mathrm{TL}}$ arises from the parallel of the two transmission lines representing the upper and lower half spaces. It can be noted that the matrix $\mathbf{Y}_{\mathrm{TETM}}$ is diagonal in the low frequency approximation (sub-wavelength patches) [18]. This means that the TE and TM components of the scattering from a layer of electrically small patches are decoupled. Moreover, since the terms of the matrix $\mathbf{Y}_{\mathrm{TETM}}$ do not depend on ϕ, the scattering from the structure under consideration is azimuthally independent.

The matrix $\mathbf{Y}_{\mathrm{ADL}}$ represents the equivalent reactance of the layer and depends on the susceptance of the single layer B_{SL}

$$B_{\mathrm{SL}} \approx \frac{\omega\varepsilon_0\varepsilon_r p}{\pi}\sum_{m\neq 0}\frac{\left|\mathrm{sinc}(\pi m w/p)\right|^2}{|m|}, \tag{2.27}$$

Fig. 2.5 shows the equivalent transmission line model, where the line represents $\mathbf{Y}_{\mathrm{TL}}$ and the shunt impedance represents $\mathbf{Y}_{\mathrm{ADL}}$. The shunt impedance is given by

$$Z_{\mathrm{layer,TE}} = -\frac{j}{B_{\mathrm{SL}}}\frac{1}{1 - k_\rho^2/(2k_{\mathrm{host}}^2)} \tag{2.28}$$

$$Z_{\mathrm{layer,TM}} = -\frac{j}{B_{\mathrm{SL}}}, \tag{2.29}$$

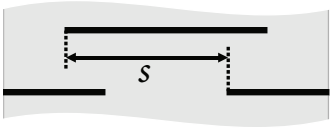

Figure 2.6: Two metal layers of an ADL slab, with a shift between them which is highlighted by the parameter s.

where $k_\rho = k_{\text{host}} \sin\theta$ and k_{host} is the wavenumber in the host medium of the ADL.

In these equations, it is assumed that the period of the ADL is equal in the x- and y-direction and equal to p.

Multiple Layers

The model shown above was extended for multiple layers in [19], and then for non-aligned layers in [20]. To account for the multiple layers, two changes are made to the model. To account for the interaction between layers, the susceptance B_{SL} is replaced by two different expressions. The first, B_∞, is used for all internal layers, which have a layer both above and below them. The second, $B_{\text{semi}-\infty}$, is used for the layers on top and bottom of the stack. This model assumes that the parameters of the ADL are constant throughout the layer stack.

The susceptance of the layers in the middle of the stack, B_∞ is similar to the susceptance of the single layer in (2.27), where a coupling term is added that accounts for higher-order (reactive) interaction with the layers above and below. For aligned layers and $d_x = d_y = p$, it is given by

$$B_{\infty,\text{aligned}} \approx \frac{\omega\varepsilon_0\varepsilon_r p}{\pi} \sum_{m\neq 0} \frac{\left|\text{sinc}(\pi m w/p)\right|^2}{|m|} \cdot j \tan\left(-\frac{j\pi\,|m|\,d_z}{p}\right). \tag{2.30}$$

The susceptance $B_{\text{semi}-\infty}$ is also similar to the single-layer expression as seen in (2.27), with the inclusion of a term accounting for the reactive coupling with the adjacent layer. For aligned layers, it is given by

$$B_{\text{semi}-\infty,\text{aligned}} \approx \frac{\omega\varepsilon_0\varepsilon_r p}{\pi} \sum_{m\neq 0} \frac{\left|\text{sinc}(\pi m w/p)\right|^2}{|m|} \cdot \left(\frac{1}{2} + \frac{j}{2}\tan\left(-\frac{j\pi\,|m|\,d_z}{p}\right)\right).$$

When the layers are no longer aligned, the expression is generalized to account for the phase shift between the layers, indicated by s in Fig. 2.6. This results in

$$B_\infty \approx \frac{\omega\varepsilon_0\varepsilon_r p}{\pi} \sum_{m\neq 0} \frac{\left|\text{sinc}(\pi m w/p)\right|^2}{|m|} \Bigg(-j\cot\left(-\frac{j2\pi\,|m|\,d_z}{p}\right) + j\exp\left(\frac{j2\pi m s}{p}\right)\csc\left(-\frac{j2\pi\,|m|\,d_z}{p}\right)\Bigg). \tag{2.31}$$

The susceptance for the top and bottom layer of the non-aligned ADL is given by the solution of the semi-infinite cascade, which gives

$$B_{\text{semi}-\infty} \approx \frac{\omega\varepsilon_0\varepsilon_r p}{\pi} \sum_{m\neq 0} \frac{\left|\text{sinc}(\pi m w/p)\right|^2}{|m|} \left(\frac{1}{2} - \frac{j}{2}\cot\left(-\frac{j2\pi\,|m|\,d_z}{p}\right) + \frac{j}{2}\exp\left(\frac{j2\pi m s}{p}\right)\csc\left(-\frac{j2\pi\,|m|\,d_z}{p}\right)\right). \tag{2.32}$$

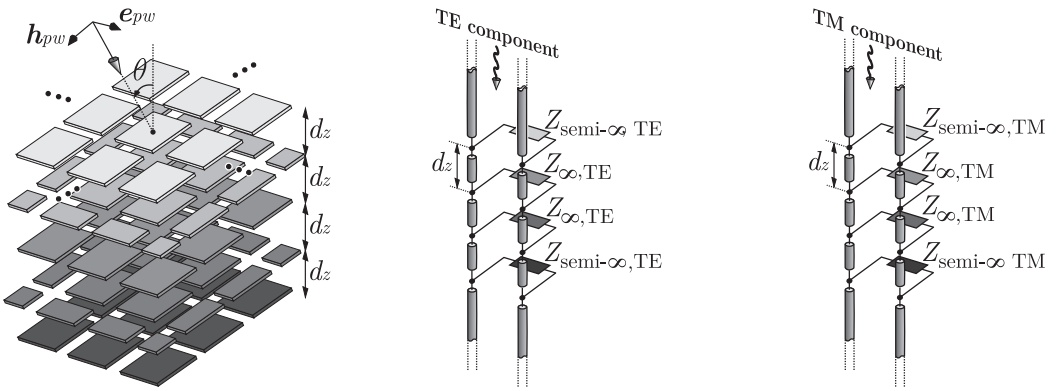

(a) (b) (c)

Figure 2.7: Multi-layered ADL stack with (a) an example stratification and (b) the equivalent transmission line model for TE and (c) TM incidence.

The transmission line model of the multi-layered ADL follows from the model for the single layer shown in Fig. 2.5. The model is shown in Fig. 2.7, where the length of each transmission line section is given by d_z, and the impedances are given by

$$Z_{\text{TE,semi}-\infty} = -\frac{j}{B_{\text{semi}-\infty}} \frac{1}{1-k_\rho^2/(2k_{\text{host}}^2)} \qquad Z_{\text{TM,semi}-\infty} = -\frac{j}{B_{\text{semi}-\infty}} \tag{2.33}$$

$$Z_{\text{TE},\infty} = -\frac{j}{B_\infty} \frac{1}{1-k_\rho^2/(2k_{\text{host}}^2)} \qquad Z_{\text{TM},\infty} = -\frac{j}{B_\infty} \tag{2.34}$$

Non-periodic Layers

The model described above assumes that the ADL is periodic in that all layers have the same geometrical parameters, aside from a constant shift between the layers. Relaxing this requirement and following the same steps as used previously, the layer susceptance can be altered to account for different shifts and distances between a layer and its neighbors. The geometry of such an ADL is shown in Fig. 2.8.

The susceptance of the n-th layer is given by

$$\begin{aligned} B_n = \frac{jp}{\zeta_0\lambda_0} \sum_{m\neq 0} \{ & S_m(w_n)\left[f_m(d_{n,n+1}) + f_m(d_{n-1,n})\right] + \\ & S_m(w_{n+1}) g_m(s_{n,n+1}, d_{n,n+1}) + \\ & S_m(w_{n-1}) g_m(s_{n-1,n}, d_{n-1,n})\}, \end{aligned} \tag{2.35}$$

where the functions $S_m(w)$, $f_m(d)$, and $g_m(s,d)$ are given by

$$S_m(w) = \frac{\left|\operatorname{sinc}\left(\frac{\pi m w}{p}\right)\right|^2}{|m|} \tag{2.36}$$

$$f_m(d) = \cot\left(\frac{-j2\pi\,|m|\,d}{p}\right) \tag{2.37}$$

$$g_m(s,d) = \exp\left(\frac{-j2\pi m s}{p}\right) \csc\left(\frac{-j2\pi\,|m|\,d}{p}\right). \tag{2.38}$$

Here, the period p is assumed to be constant throughout the stratification and is therefore omitted in the definition of the functions. The susceptance of the first and last layers ($n = 1$ and $n = N$)

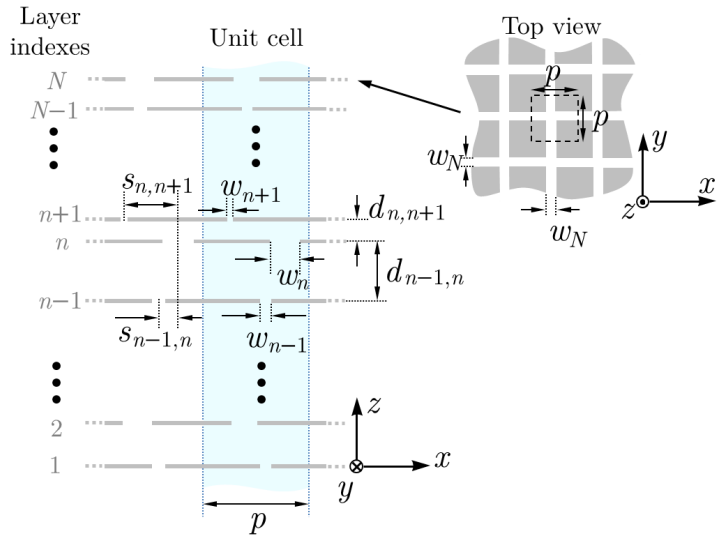

Figure 2.8: Illustration of a non-periodic non-aligned multilayer ADL with geometrical parameters.

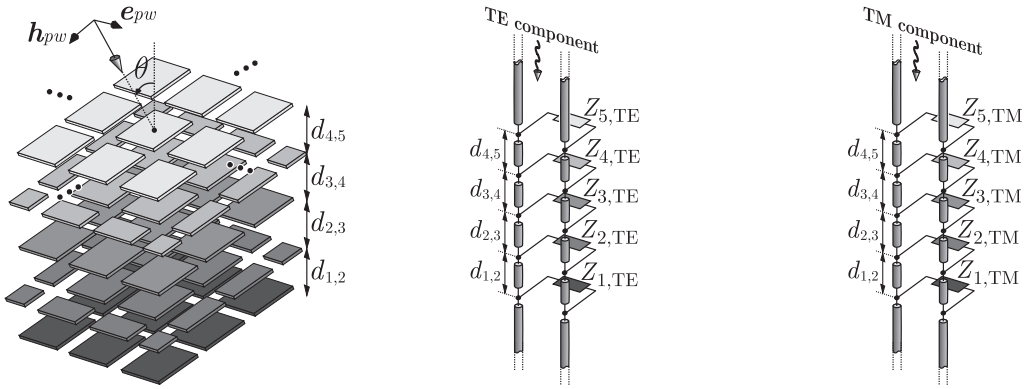

(a) (b) (c)

Figure 2.9: Multi-layered non-periodic ADL stack with (a) an example stratification and (b) the equivalent transmission line model for TE and (c) TM incidence.

is given by

$$B_1 = \frac{jp}{\zeta_0 \lambda_0} \sum_{m \neq 0} \{S_m(w_1)\,[f_m(d_{1,2}) - j] + S_m(w_2) g_m(s_{1,2}, d_{1,2})\}, \tag{2.39}$$

$$B_N = \frac{jp}{\zeta_0 \lambda_0} \sum_{m \neq 0} \{S_m(w_N)\,[-j + f_m(d_{N-1,N})] + S_m(w_{N-1}) g_m(s_{N-1,N}, d_{N-1,N})\}, \tag{2.40}$$

due to the absence of one of their adjacent layers.

The equivalent transmission line model for this scenario is similar to that of the periodic case, except that instead of the two susceptances $B_{\text{semi}-\infty}$ and B_∞, there is now a unique susceptance B_n for every layer n. This means that there is a unique impedance $Z_{n,TE/TM}$ for each layer. The distance between layers can also vary, so each transmission line has its own length $d_{n,n+1}$. The transmission lines connecting different layers represent the fundamental Floquet wave propagating through the ADL structure. The resulting model is shown in Fig. 2.9.

In this work, when computing the scattering parameters of an ADL structure, a transmission

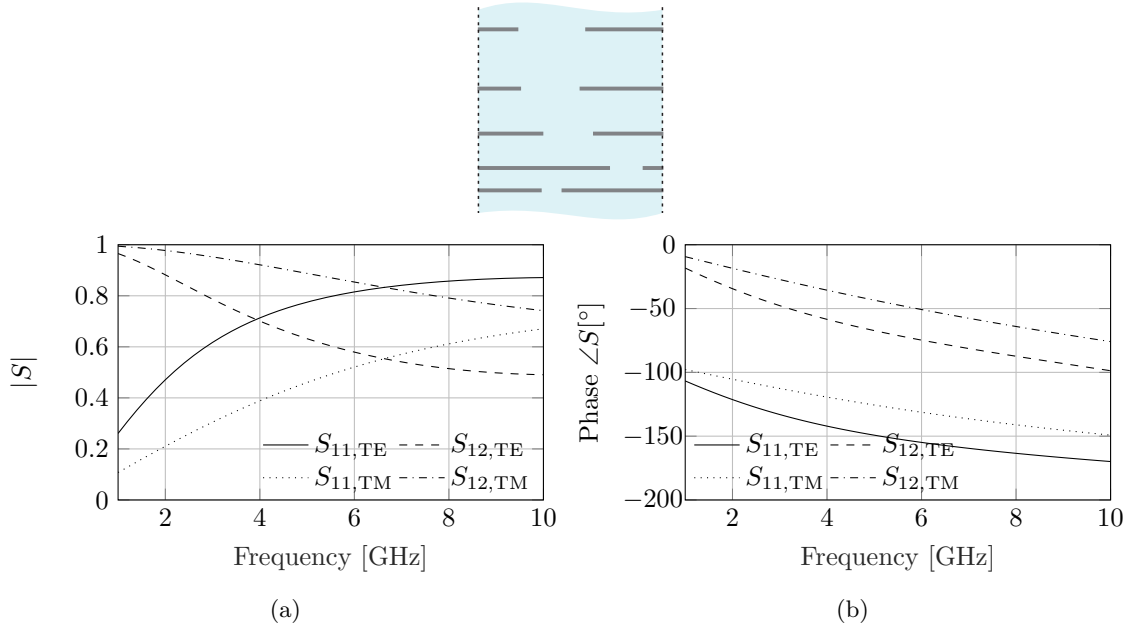

(a) (b)

Figure 2.10: (a) Amplitude and (b) phase of the reflection and transmission coefficients of a plane wave incident on the 5-layer ADL from [21, fig.6]. The period is $p = 0.0785\lambda_0$ and the other geometrical parameters are changing throughout the structure: $w_n = (0.01, 0.015, 0.02, 0.025, 0.03)\lambda_0$, $s_{n,n+1} = (0.4, 0.3, 0.1, 0.0)p$, and $d_{n,n+1} = (0.01, 0.015, 0.02, 0.025)\lambda_0$. λ_0 is the free space wavelength at 5 GHz. The angle of incidence is $\theta = 60°$.

line is placed above the topmost layer with a height of $d = d_{N-1,N}/2$ and a line below the bottommost layer with a height of $d = d_{1,2}/2$. Such gaps are also considered when cascading multiple ADL slabs to implement multi-section transformers. When these structures are simulated using a commercial solver, the host medium of the ADL is extended by these same heights above and below the top- and bottommost layers.

Validation

To validate the implementation of the equations shown above, an example given in an earlier paper is reproduced, [21, fig.6]. In this example, there are 5 layers ($N = 5$) and the width of the gap between the patches varies per layer n, w_n is given by $w_n = (0.01, 0.015, 0.02, 0.025, 0.03)\lambda_0$. The unit cell is $p = 0.0785\lambda_0$, the distance between layers is $d_{n,n+1} = 0.012\lambda_0$, and there is no shift $s_{n,n+1} = 0$. The angle of incidence is $\theta = 60°$. Fig. 2.10 shows the magnitude and phase of the reflection and transmission parameters S_{11} and S_{21} for TE and TM incidence. It is seen that the results obtained here agree with those shown in [21].

2.3 Combination of Connected Arrays and Artificial Dielectrics

The formulations for the connected arrays and the ADLs can be combined to simulate the active input impedance of a connected array unit cell loaded with ADLs. The expressions (2.1) to (2.7) can be applied by considering the transmission model for the stratified medium including the ADLs. This requires solving for the TE and TM currents (2.6) and (2.7) which are solutions of the equivalent transmission lines depicted in Fig. 2.11. The figure also shows the transmission line model for the backing reflector, which is assumed to be located below the connected slot plane.

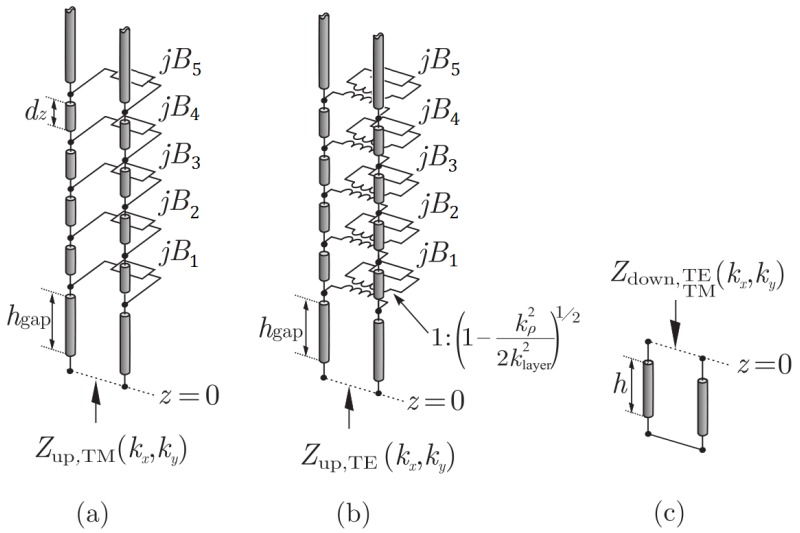

Figure 2.11: Equivalent transmission line model for a connected array of slots in the presence of a backing reflector and an ADL.

The expression of the ADLs were given for plane wave incidence. When the ADL is illuminated by a connected array located in the near field, the analysis can still be used by expanding the field radiated by the connected array into a spectrum of waves (Floquet modes). To account for the reactive interaction between the connected slot radiating elements and the ADL slab, the term k_ρ^2 in (2.28) is replaced with the transverse wavenumber of the Floquet mode for the connected array unit cell $k_{\rho m}^2 = k_{xm}^2 + k_{ym}^2$. This allows to treat also the cases of non-homogeneous plane waves (higher order Floquet modes).

As an example, Fig. 2.12 shows a comparison between the active input impedance and the active reflection coefficient calculated using the analytical formulations and CST. There is a good agreement between the two methods. The parameters used for the slot and the ADL transformer for the given example are shown in Appendix A in Table A.2 and Table A.3, respectively.

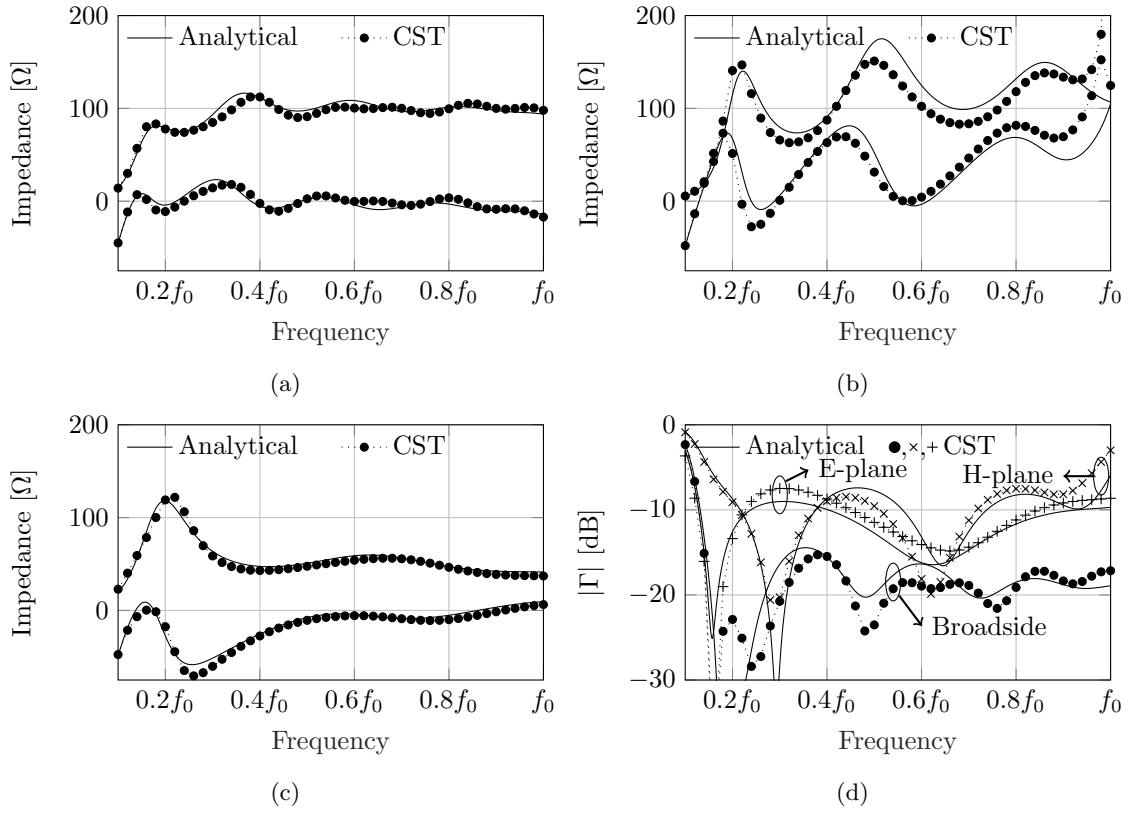

Figure 2.12: Comparison between results obtained using analytical formulations of the slot array and ADL stack, and those obtained using CST. Input impedance is shown for (a) broadside, scanning to 60° in the (b) H- and (c) E-plane. (d) Reflection coefficients when matched to 80 Ω.

Chapter 3

ADL Synthesis

This chapter will outline the process used to design a set of ADLs such that they function as an impedance transformer. First, several ideal impedance transformers are shown and compared in Section 3.1. Then, the relationship between the ADLs and dielectrics is shown in Section 3.2. Next, the process used to design the metal layers is shown in Section 3.3. Finally, an example design is shown in Section 3.4 to show the accuracy of the described method.

3.1 Transformers

This section will discuss various impedance transformers that can be used in the realization of the impedance transformation that is required to achieve the desired bandwidth using a connected slot array. First, the quarter-wave transformer is discussed, which is then extended to multi-section transformers. Next, the Chebyshev transformer is discussed, after which two ideal continuous transformers and their discretization are discussed. Finally, the shown transformers are compared by using each of them to design a 1 to 5 impedance transformer with a 1 to 5 bandwidth.

3.1.1 Quarter-Wave Transformer

The most widely used impedance transformer is the quarter-wave transformer. It is usually a single-section matching layer that is used to match a transmission line to a real load. It provides perfect matching at a given frequency f_0, and a bandwidth Δf that depends on the difference between the line and load impedances.

For a single-section quarter-wave transformer the impedance of the matching section is given by

$$Z_1 = \sqrt{Z_0 Z_L}, \tag{3.1}$$

where Z_0 is the line impedance and Z_L is the load impedance. The input impedance seen from the line is

$$Z_{\text{in}} = Z_1 \frac{Z_L + jZ_1 \tan(\beta l)}{Z_1 + jZ_L \tan(\beta l)} = Z_1 \frac{Z_L + jZ_1 \tan(\frac{\pi}{2}\frac{f}{f_0})}{Z_1 + jZ_L \tan(\frac{\pi}{2}\frac{f}{f_0})}, \tag{3.2}$$

where β is the propagation constant at frequency f. Expanding these equations to obtain the fractional bandwidth is done in [25, p.247] and results in

$$\frac{\Delta f}{f_0} = 2 - \frac{4}{\pi} \cos^{-1}\left[\frac{\Gamma_m}{\sqrt{1-\Gamma_m^2}} \frac{2\sqrt{Z_0 Z_L}}{|Z_L - Z_0|} \right], \tag{3.3}$$

where Γ_m is the desired reflection coefficient magnitude.

As an example, the $-10\,\text{dB}$ bandwidth of a quarter-wave transformer for a 1 to 5 impedance transformation is obtained from (3.3) as

$$\frac{\Delta f}{f_0} = 2 - \frac{4}{\pi}\cos^{-1}\left[\frac{10^{-\frac{10}{20}}}{\sqrt{1-10^{-2\frac{10}{20}}}}\frac{2\sqrt{1\cdot 5}}{|5-1|}\right] = 0.5472 \tag{3.4}$$

3.1.2 Multi-Section Transformer

To obtain a wider bandwidth, several quarter-wave transformers can be cascaded. The impedance of these sections can be designed such that specific characteristics are obtained, such as a maximally flat passband (Binomial) or maximum bandwidth (Chebyshev). Since the bandwidth of the Chebyshev transformer is larger than that of the Binomial [25], the Chebyshev transformer is preferred for this application, and is detailed in Section 3.1.3.

The response of a multi-section transformer is derived in [25, p.251] and can be written as

$$\begin{aligned}\Gamma(\theta) = 2e^{-jN\theta}\Big[&\Gamma_0\cos N\theta + \Gamma_1\cos(N-2)\theta + \cdots \\ &+ \Gamma_n\cos(N-2n)\,\theta + \cdots + \frac{1}{2}\Gamma_{N/2}\Big]\end{aligned} \qquad \text{for even } N \tag{3.5a}$$

$$\begin{aligned}\Gamma(\theta) = 2e^{-jN\theta}\Big[&\Gamma_0\cos N\theta + \Gamma_1\cos(N-2)\,\theta + \cdots \\ &+ \Gamma_n\cos(N-2n)\,\theta + \cdots + \frac{1}{2}\Gamma_{(N-1)/2}\cos\theta\Big]\end{aligned} \qquad \text{for odd } N, \tag{3.5b}$$

where Γ_n is the reflection coefficient at the boundary between sections n and $n+1$. These equations will be used in the definition of the impedances used by the Chebyshev transformer in Section 3.1.3.

3.1.3 Chebyshev Transformer

The Chebyshev transformer is based on the Chebyshev polynomials, of which the first four are given by

$$T_1(x) = x \tag{3.6a}$$
$$T_2(x) = 2x^2 - 1 \tag{3.6b}$$
$$T_3(x) = 4x^3 - 3x \tag{3.6c}$$
$$T_4(x) = 8x^4 - 8x^2 + 1, \tag{3.6d}$$

and higher order polynomials are obtained using

$$T_n(x) = 2xT_{n-1}(x) - T_{n-2}(x). \tag{3.7}$$

A property of the Chebyshev polynomials is that for $|x| < 1$, $|T_n(x)| < 1$. This is exploited to obtain an equal-ripple passband by mapping θ_m to $x = -1$ and $\pi - \theta_m$ to $x = 1$. To do this, x is substituted by $x = \cos\theta\sec\theta_m$, resulting in

$$T_1(\sec\theta_m\cos\theta) = \sec\theta_m\cos\theta \tag{3.8a}$$
$$T_2(\sec\theta_m\cos\theta) = 2\sec^2\theta_m\cos^2\theta - 1 \tag{3.8b}$$
$$T_3(\sec\theta_m\cos\theta) = 4\sec^3\theta_m\cos^3\theta - 3\sec\theta_m\cos\theta \tag{3.8c}$$
$$T_4(\sec\theta_m\cos\theta) = 8\sec^4\theta_m\cos^4\theta - 8\sec^2\theta_m\cos^2\theta + 1, \tag{3.8d}$$

where $\cos^n\theta$ is expanded in terms of $\cos(n\theta)$ using

$$\cos^n\theta = \frac{1}{2^n}\binom{n}{\frac{n}{2}} + \frac{1}{2^{1-n}}\sum_{k=0}^{\frac{n}{2}-1}\binom{n}{k}\cos(n-2k)\,\theta \qquad \text{for even } n \tag{3.9a}$$

$$\cos^n\theta = \frac{1}{2^{1-n}}\sum_{k=0}^{\frac{n-1}{2}}\binom{n}{k}\cos(n-2k)\,\theta \qquad \text{for odd } n. \tag{3.9b}$$

This results in

$$T_1(\sec\theta_m\cos\theta) = \sec\theta_m\cos\theta \tag{3.10a}$$

$$T_2(\sec\theta_m\cos\theta) = 2\sec^2\theta_m\,(\cos 2\theta + 1) - 1 \tag{3.10b}$$

$$T_3(\sec\theta_m\cos\theta) = 4\sec^3\theta_m\,(\cos 3\theta + 3\cos\theta) - 3\sec\theta_m\cos\theta \tag{3.10c}$$

$$T_4(\sec\theta_m\cos\theta) = 8\sec^4\theta_m\,(\cos 4\theta + 4\cos 2\theta + 3) - 8\sec^2\theta_m\,(\cos 2\theta + 1) + 1, \tag{3.10d}$$

where higher order polynomials are obtained by substituting $x = \sec\theta_m\cos\theta$ in (3.7). The resulting expression for the n-th order Chebyshev transformer is

$$T_n(\sec\theta_m\cos\theta) = 2\,(\sec\theta_m\cos\theta)\cdot T_{n-1}(\sec\theta_m\cos\theta) - T_{n-2}(\sec\theta_m\cos\theta). \tag{3.11}$$

The equal-ripple passband in an N-section Chebyshev transformer is obtained by equating (3.5) and (3.11)

$$\Gamma(\theta) = 2e^{-jN\theta}\left[\Gamma_0\cos N\theta + \Gamma_1\cos(N-2)\,\theta + \cdots + \Gamma_n\cos(N-2n)\,\theta + \cdots\right] \tag{3.12}$$

$$= Ae^{-jN\theta}T_N\left(\sec\theta_m\cos\theta\right), \tag{3.13}$$

and grouping similar terms of $\cos(n\theta)$. Solving for $\Gamma(0)$ yields

$$\Gamma(0) = \frac{Z_L - Z_0}{Z_L + Z_0} = AT_N(\sec\theta_m) \tag{3.14}$$

from which it follows that

$$A = \frac{Z_L - Z_0}{Z_L + Z_0}\frac{1}{T_N(\sec\theta_m)}. \tag{3.15}$$

Since the maximum value of $T_N\sec\theta_m\cos\theta$ is 1, setting the maximum reflection coefficient in the passband to be Γ_m yields that $|A| = \Gamma_m$. It follows that

$$T_N(\sec\theta_m) = \frac{1}{\sec\theta_m}\left|\frac{Z_L - Z_0}{Z_L + Z_0}\right|, \tag{3.16}$$

from which we can determine θ_m as

$$\sec\theta_m = \cosh\left[\frac{1}{N}\cosh^{-1}\left(\frac{1}{\Gamma_m}\left|\frac{Z_L - Z_0}{Z_L + Z_0}\right|\right)\right]. \tag{3.17}$$

Finally, Z_n is determined using

$$Z_n = Z_{n-1}\cdot e^{2\Gamma_n}, \tag{3.18}$$

where Γ_n is obtained by solving (3.12) for terms of $\cos n\theta$. The fractional bandwidth of a Chebyshev transformer is found from (3.17) to be

$$\frac{\Delta f(\Gamma_m)}{f_0} = \frac{2(f_0 - f_m)}{f_0} = 2 - \frac{2f_m}{f_0} = 2 - \frac{4\theta_m}{\pi}, \tag{3.19}$$

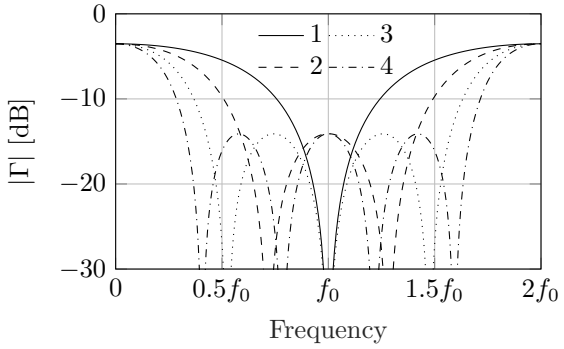

Figure 3.1: Reflection coefficient versus frequency of a 1- to 4-section Chebyshev transformer where $\Gamma_m = 0.05$.

where f_m is related to the reflection coefficient Γ_m through $f_m = (2\theta_m f_0)/\pi$ and (3.17). The reflection coefficients for a 1- to 4-section, 1 to 5 Chebyshev transformer are shown in Fig. 3.1, where $\Gamma_m = 0.05$ is used.

The $-10\,\text{dB}$ bandwidth of a Chebyshev transformer for the 1 to 5 impedance transformation is obtained from (3.19) as

$$\begin{aligned}\frac{\Delta f}{f_0} &= 2 - \frac{4}{\pi}\sec^{-1}\left(\cosh\left[\frac{1}{N}\cosh^{-1}\left(\frac{1}{\Gamma}\left|\frac{Z_L - Z_0}{Z_L + Z_0}\right|\right)\right]\right) \\ &= 2 - \frac{4}{\pi}\sec^{-1}\left(\cosh\left[\frac{1}{N}\cosh^{-1}\left(\frac{1}{10^{-\frac{10}{20}}}\left|\frac{5-1}{5+1}\right|\right)\right]\right) \\ &= 2 - \frac{4}{\pi}\sec^{-1}\left(\cosh\frac{1.37728}{N}\right). \end{aligned} \tag{3.20}$$

3.1.4 Tapered Transformer

Another form of transformer is one where the impedance changes as a continuous function of position. As will be seen below, this type of transformer has an infinite bandwidth due to its monotonously decreasing reflection coefficient peak height. Many functions can be used for the tapering of the impedance from one value to another. Here, two different tapers and their performance will be considered. First, the exponential taper and the method to discretize it is discussed, after which the triangular taper and its discretization are shown.

Exponential Transformer

The exponential transformer varies its impedance in a continuous manner as a function of distance, according to

$$Z(z) = Z_0 e^{az} \quad \text{for } 0 < z < L, \tag{3.21}$$

where a determines the impedance at $z = L$. Since we desire the impedance at the end of the taper to be equal to the load impedance ($Z(L) = Z_L$), we use

$$a = \frac{1}{L}\log\frac{Z_L}{Z_0}. \tag{3.22}$$

This function is shown in Fig. 3.2a to smoothly vary from the input impedance Z_0 to the load impedance Z_L. Using the theory of small reflections [25, eq. 5.67], the total reflection coefficient at $z = 0$ can be determined as

$$\Gamma(\theta) = \frac{1}{2}\int_{z=0}^{L} e^{-2j\beta z}\frac{d}{dz}\log\left(\frac{Z}{Z_0}\right). \tag{3.23}$$

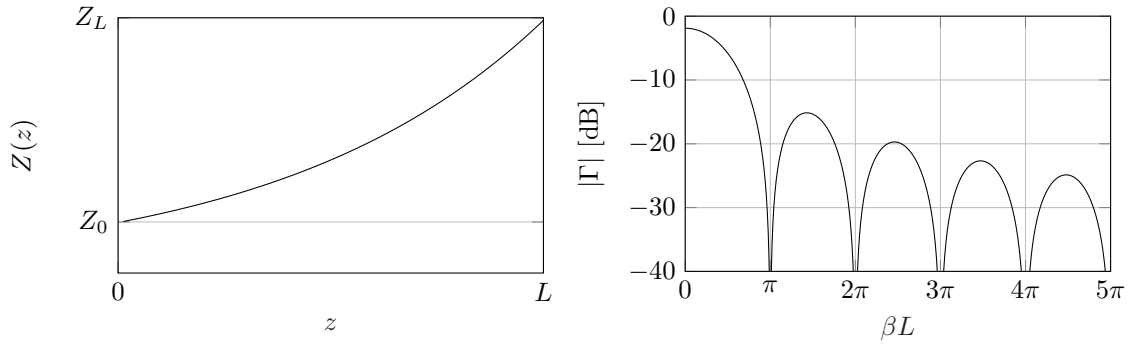

(a) (b)

Figure 3.2: (a) Impedance profile and (b) reflection coefficient versus frequency of an exponential transformer.

Substituting Z in this equation with $Z(z)$ yields

$$\begin{aligned}\Gamma(\theta) &= \frac{1}{2}\int_{z=0}^{L} e^{-2j\beta z}\frac{d}{dz}\log\left(e^{az}\right) \\ &= \frac{\log Z_L/Z_0}{2}e^{-j\beta L}\frac{\sin\beta L}{\beta L},\end{aligned} \tag{3.24}$$

which is shown in Fig. 3.2b. It can be seen that the first null is found at $\beta L = \pi$, which is the point where the total length of the transformer is half-wave ($L = \lambda/2$). The level of each consecutive sidelobe is seen to be continuously decreasing.

The $-10\,\text{dB}$ bandwidth of an ideal continuous 1 to 5 exponential transformer is obtained using (3.24) and ranges from $\beta L = 0.68\pi$ to infinity. This gives an infinite fractional bandwidth.

Discretization of the Exponential Transformer

Since a continuous impedance taper cannot be synthesized by an artificial dielectric slab, it must be discretized and built using multiple sections. We define an N-section transformer where the impedance of the nth section is given by

$$Z_n = Z\left(\frac{n-0.5}{N}L\right) = Z_0\exp\left(a\frac{n-0.5}{N}L\right), \tag{3.25}$$

for $1 \leq n \leq N$, where a is as defined in (3.22). The reflection coefficient for this discretized exponential transformer is obtained by summing the reflection at each interface between sections as

$$\Gamma(\theta) = \sum_{n=0}^{N}\Gamma_n \tag{3.26}$$

$$= \sum_{n=0}^{N}\frac{Z_{n+1}-Z_n}{Z_{n+1}+Z_n}\exp\left(-j2k_0\frac{n}{N}L\right). \tag{3.27}$$

The impedance profile and resulting reflection coefficient for a 5-section 1 to 5 discretized exponential transformer are shown in Fig. 3.3. It is seen that instead of the continuously decreasing sidelobe levels of the continuous case, the discretized transformer becomes mismatched at the point $\beta L = N\pi$. At this point, the length of each discretization section becomes $\lambda/2$.

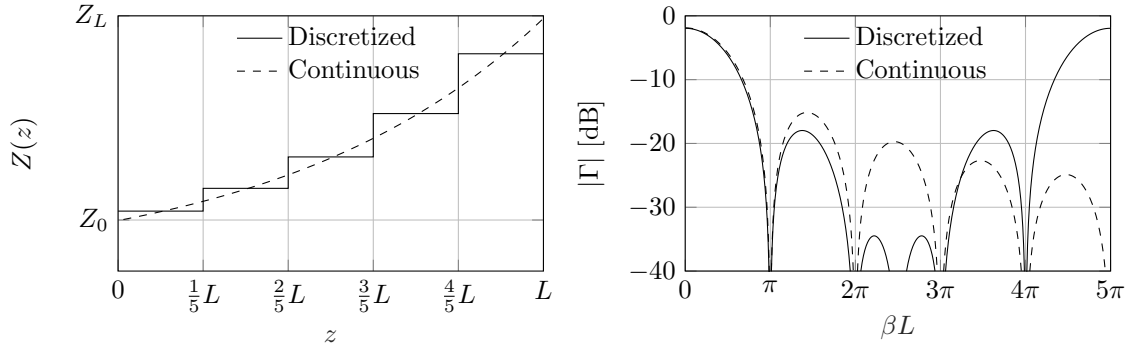

(a) (b)

Figure 3.3: (a) Impedance profile and (b) reflection coefficient versus frequency of a 5-section discretized exponential transformer.

The $-10\,\mathrm{dB}$ bandwidth of an N-section 1 to 5 discretized exponential transformer is obtained using (3.27) and ranges from $\beta L = 0.68\pi$ to $\beta L = (N-0.68)\pi$. From this, the fractional bandwidth is obtained as

$$\frac{\Delta f}{f_0} = \frac{N - 2 \cdot 0.68}{2L/\lambda_0}. \tag{3.28}$$

Triangular Transformer

The triangular transformer derives its name from the fact that the derivative of the log of the ratio of the impedance ($d(\log Z/Z_0)/dz$) is triangular in shape. It offers lower peaks in the reflection coefficient than the exponential taper, but the lower edge of the passband shifts up, as will be seen below. The impedance of the triangular taper is given by

$$Z(z) = \begin{cases} Z_0 \exp\left(2\frac{z^2}{L^2}\right) \log Z_L/Z_0 & \text{for } 0 \le z \le L/2 \\ Z_0 \exp\left(4\frac{z}{L} - 2\frac{z^2}{L^2} - 1\right) \log Z_L/Z_0 & \text{for } L/2 \le z \le L, \end{cases} \tag{3.29}$$

and is shown in Fig. 3.4a. The reflection coefficient can again be evaluated using (3.23) and is found to be

$$\Gamma(\theta) = \frac{1}{2} e^{-j\beta L} \log\left(\frac{Z_L}{Z_0}\right) \left[\frac{\sin(\beta L/2)}{\beta L/2}\right]^2, \tag{3.30}$$

which is shown in Fig. 3.4b.

The $-10\,\mathrm{dB}$ bandwidth of an ideal 1 to 5 triangular transformer is obtained using (3.30) and ranges from $\beta L = \pi$ to infinity. This means that to obtain the same bandwidth as the exponential transformer, the triangular transformer's length L must be 50% higher.

Discretization of the Triangular Transformer

The process used to discretize the triangular transformer is very similar to the process used for the exponential transformer. We again define an N-section transformer where the impedance of the

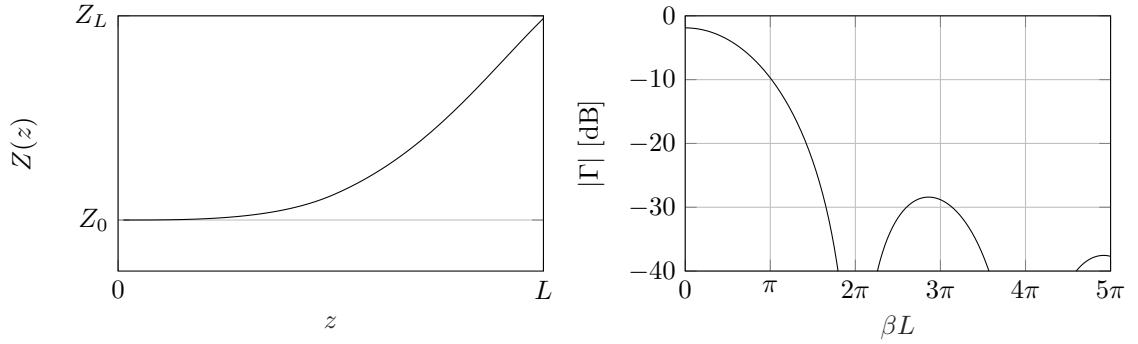

(a) (b)

Figure 3.4: (a) Impedance profile and (b) reflection coefficient versus frequency of a 1 to 5 triangular transformer.

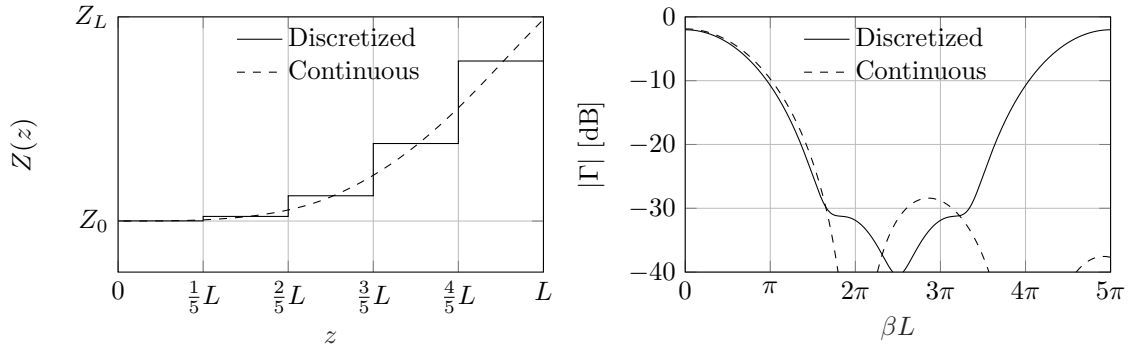

(a) (b)

Figure 3.5: (a) Impedance profile and (b) reflection coefficient versus frequency of a 5-section discretized triangular transformer.

nth section is given by

$$Z_n = Z\left(\frac{n-0.5}{N}L\right) \tag{3.31}$$

$$= \begin{cases} Z_0 \exp\left(2\left(\frac{n-0.5}{N}\right)^2\right) \log Z_L/Z_0 & \text{for } 0 \le n < N/2 \\ Z_0 \exp\left(4\frac{n-0.5}{N} - 2\left(\frac{n-0.5}{N}\right)^2 - 1\right) \log Z_L/Z_0 & \text{for } N/2 \le n \le N, \end{cases} \tag{3.32}$$

for $1 \le n \le N$. The reflection coefficient is then calculated as in (3.27). The impedance profile and resulting reflection coefficient for a 5-section discretized triangular transformer are shown in Fig. 3.5.

The $-10\,\text{dB}$ bandwidth of an N-section 1 to 5 discretized triangular transformer is obtained using (3.27) and ranges from $\beta L = 0.96\pi$ to $\beta L = (N-0.96)\pi$. From this, the fractional bandwidth is obtained as

$$\frac{\Delta f}{f_0} = \frac{N - 2 \cdot 0.96}{2L/\lambda_0}. \tag{3.33}$$

Table 3.1: Comparison of required parameters to achieve a 1 to 5 bandwidth for a 1 to 5 impedance transformation using a Chebyshev transformer, or with a discretized Exponential or Triangular transformer.

	Chebyshev	Exponential	Triangular
Required Length L	$1.25\lambda_0$	$1.7\lambda_0$	$2.6\lambda_0$
Required Sections N	3	5	7
Passband Depth	$-10\,\mathrm{dB}$	$-18\,\mathrm{dB}$	$-31\,\mathrm{dB}$

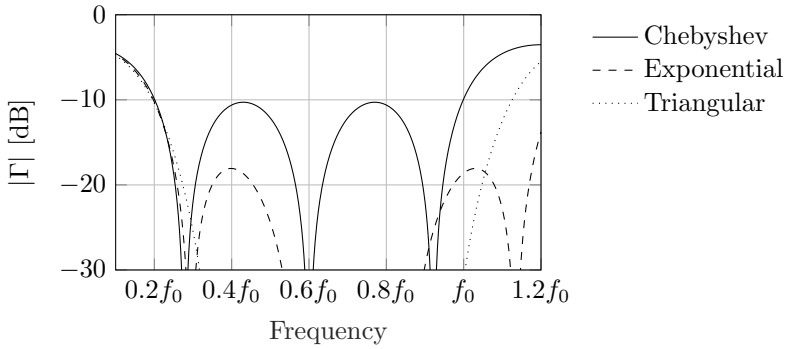

Figure 3.6: Reflection coefficient versus frequency of a 1 to 5 impedance transformation using the transformers and parameters listed in Table 3.1.

3.1.5 Transformer Comparison

The transformers described in this chapter each have their own advantages and disadvantages. The transformers are compared by their requirements when at least a $0.2f_0$ to f_0 bandwidth is to be obtained with a 1 to 5 impedance transformation. Table 3.1 shows the parameters required to achieve the desired bandwidth for the Chebyshev, discretized Exponential, and discretized Triangular transformers.

The length L of the discretized exponential and triangular transformer is given by the lower edge of the bandwidth. A certain choice of L sets the lower edge of the bandwidth irrespective of N. The upper band is then given by the number of layers N, which is set such that the reflection coefficient is still $<-10\,\mathrm{dB}$ at f_0. Fig. 3.6 shows that the upper band of these transformers is higher than is required for a 1 to 5 bandwidth, but fewer layers would not achieve the desired bandwidth. It is seen that the Chebyshev transformer achieves a similar bandwidth with fewer required sections and a lower overall length.

However, when the reflection coefficient is calculated for each of these transformers, as seen in Fig. 3.6, it is seen that the matching of the Chebyshev transformer is right at $-10\,\mathrm{dB}$ around $0.4f_0$ and $0.8f_0$ and at the edge of the target bandwidth. Since a mismatch will be introduced when the transformer is coupled to the connected array antenna elements and when fabrication uncertainties are considered, the exponential transformer is chosen for the initial design of the array.

3.2 Homogenization of a Structure

As shown in Section 2.2, the metal layers in the ADL affect the behavior of a plane wave that travels through it. It is shown that the TE and TM component of the scattering from a layer of metal patches are decoupled, and that the ADL is azimuthally independent. As such, the ADL can be considered bi-anisotropic and the effective constitutive parameters can be extracted using S-parameters determined from plane-wave incidence. These parameters then allow the ADL to be

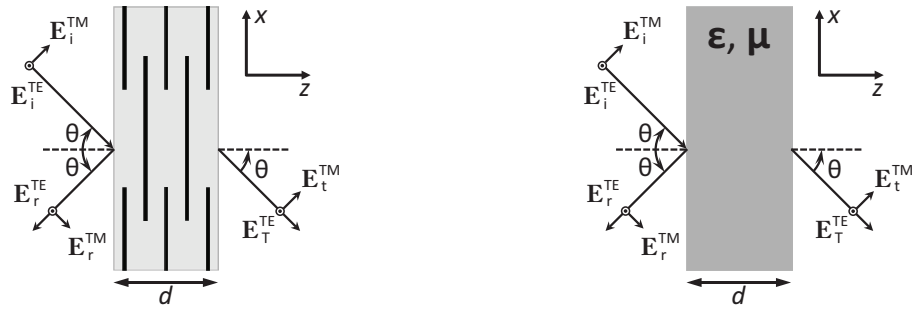

Figure 3.7: Example of (a) an ADL slab and (b) its homogeneous equivalent dielectric.

modeled as a homogeneous dielectric with permittivity and permeability matrices given by

$$\varepsilon = \begin{bmatrix} \varepsilon_x & 0 & 0 \\ 0 & \varepsilon_y & 0 \\ 0 & 0 & \varepsilon_z \end{bmatrix} \tag{3.34}$$

$$\mu = \begin{bmatrix} \mu_x & 0 & 0 \\ 0 & \mu_y & 0 \\ 0 & 0 & \mu_z \end{bmatrix}. \tag{3.35}$$

The method to extract these parameters from an arbitrary bi-anisotropic stratification that is infinite in two directions is described in [26]. It uses the S-parameters for two polarizations (TE and TM) from oblique and normal incidence to extract the relevant parameters necessary to populate the matrices given in (3.34) and (3.35). The equations for the extraction of the parameters are given in Appendix B. Fig. 3.7a shows an ADL slab of height d under test, for which the equivalent homogeneous dielectric slab is shown in Fig. 3.7b.

The azimuthal independence of the ADL means that the ADL behaves identically irrespective of the azimuth of the incident wave. This means that $\varepsilon_x = \varepsilon_y$. The vertical component of the electric field of an incident wave does not interact with the horizontal planar metal patches, which means that the z-component of the permittivity is equal to that of the host medium, $\varepsilon_z = \varepsilon_{\text{host}}$. It is shown in [24] that there is a strong diamagnetic effect that occurs in the ADL structure due to loop currents excited in the patches. This results in a reduction of the magnetic field inside the structure compared to the external field, which means that $\mu_z < 1$. The horizontal components of the permeability are shown to be $\mu_x = \mu_y = 1$.

3.3 Designing an ADL

The design process starts with the choice of a transformer design, for which the lengths L_n and impedances Z_n of a certain number of sections N are defined. Since the transformer will be constructed using ADLs, the impedances are converted to relative permittivities through

$$\varepsilon_{r,n} = \left(\frac{Z_0}{Z_n}\right)^2, \tag{3.36}$$

where $Z_0 = 120\pi$ is the impedance of free space.

Since changing the permittivity of a material also changes the wavelength inside this material, the lengths of the sections defined by the transformer must be scaled accordingly. The length L_n of each section is therefore scaled by the inverse of the square root of the permittivity, that is

$$L_{\text{ADL},n} = \frac{L_{\text{section},n}}{n}, \tag{3.37}$$

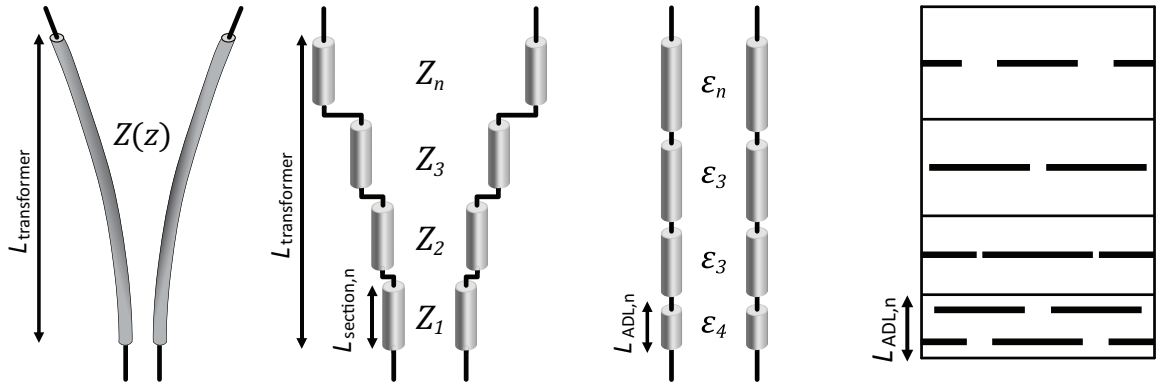

Figure 3.8: Steps to go from an ideal transmission line to an ADL. (a) Continuous impedance tapering. (b) Discretized version. (c) Homogeneous dielectric slabs, scaled vertically according to (3.37). (d) ADL version of the homogeneous slabs.

where n is the refractive index of the material which, since $\mu_x = \mu_y = 1$, is equal to $\sqrt{\varepsilon_x}$.

This is shown in Fig. 3.8, where the ideal tapered line is shown in Fig. 3.8a, which is discretized in N sections of length $L_{\text{section},n}$ in Fig. 3.8b. These transmission line sections are then implemented using homogeneous dielectric slabs in Fig. 3.8c, which are scaled vertically according to (3.37). Finally, the permittivities of these homogeneous dielectric slabs are implemented in ADL slabs as seen in Fig. 3.8d.

Using the method described in Section 3.2 the effective permittivity of an ADL slab can be determined. Using an iterative process, the parameters of an ADL slab can therefore be designed such that the slab behaves like a homogeneous dielectric with a given permittivity. As shown in the previous section, $\varepsilon_x = \varepsilon_y$. This enables the design of an ADL based on a single output value, being ε_x, which means that 1D error minimization techniques can be used.

3.3.1 Limitations on Design

The choice of transformer and slot unit cell fix several parameters prior to the design. The height of each section of the transformer fixes the distance between metal layers $d_z = H_{section}/N$ in the ADL for a given number of layers N. The unit cell size d_x of the slot limits the choice of unit cell size p of the ADL to $p = d_x/\alpha$, where $\alpha = 1, 2, \ldots$. The manufacturing process gives a lower limit to the gaps between the patches $w_{\min}$. It also sets an upper limit on the number of metal layers $N_{\max}$ based on the minimum thickness $t_{\min}$ of the dielectrics between the metal layers, $N_{\max} = L_{\text{ADL},n}/(2t_{\min})$. The maximum gap between the patches is chosen to be $w_{\max} = 0.7p$. Fig. 3.9 shows the effect of N and α on an example ADL.

3.3.2 Design Process

The design of the ADL is done iteratively using the Newton Raphson method. The process starts with a single layer $N = 1$, which is increased as needed. An arbitrary gap width $w = w_1$ is chosen, and the shift is set to its maximum value, $s = p/2$. The process described below is shown as a flow graph in Fig. 3.10. The S-parameters are simulated using the transmission line model given in Section 2.2, and the permittivity $\varepsilon_{x,1}$ is determined using the method described in Section 3.2. A second simulation is run for the same parameters except that $w_2 = w + \Delta w$, which gives the permittivity $\varepsilon_{x,2}$ for the point $w = w_2$. The error $|\varepsilon_{x,1} - \varepsilon_{\text{des}}|$ between the permittivity in $w = w_1$

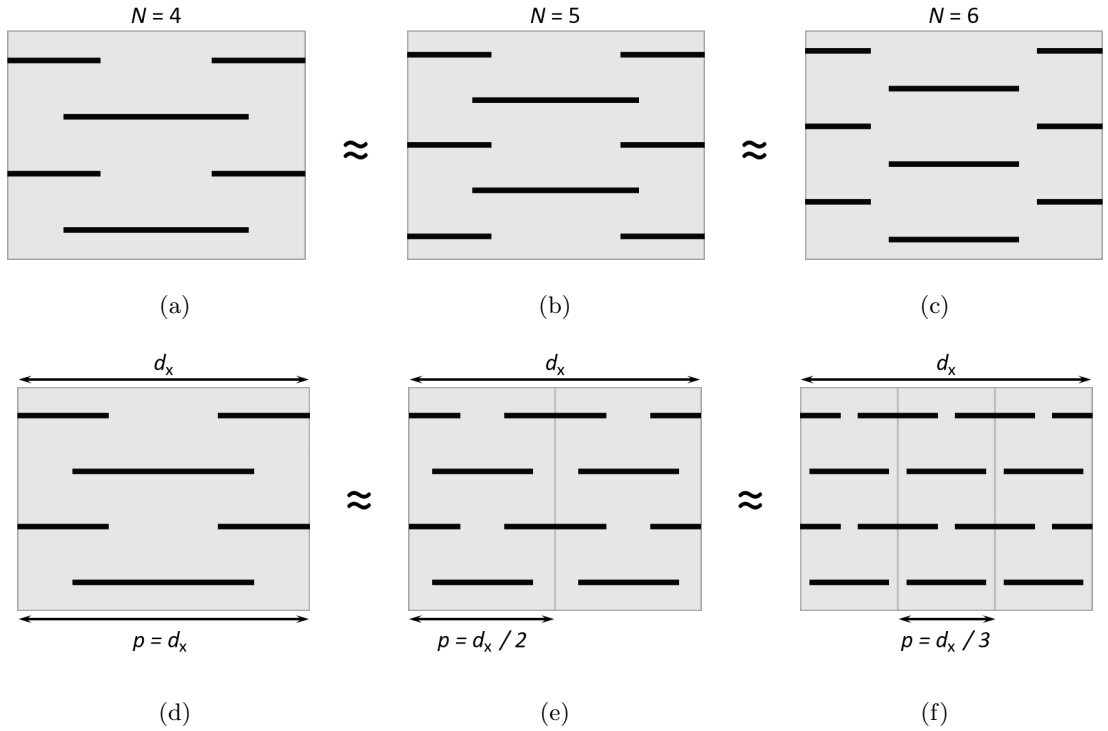

Figure 3.9: Illustration of the effect of N and α on the structure of the ADL when a given permittivity is realized. The number of layers N in the stack is varied from 4 to 6 in (a) to (c), respectively. The unit cell size $p = d_x/\alpha$ is shown for α varying from 1 to 3 in (d) to (f), respectively.

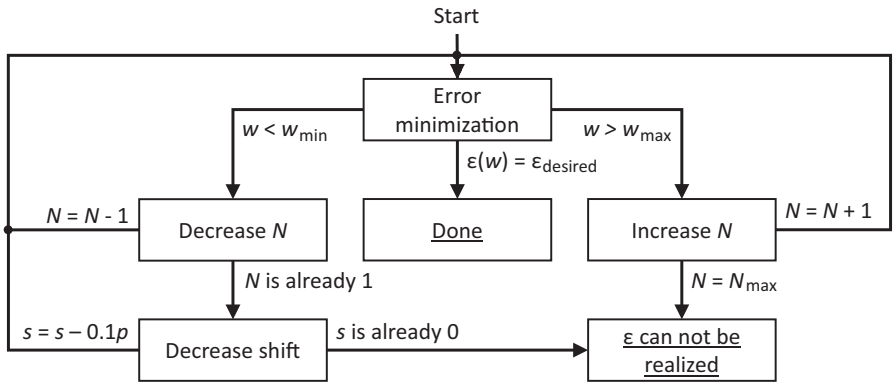

Figure 3.10: Flow graph showing the process of designing an ADL slab to have a certain given permittivity.

and the desired value ε_{des} is calculated and w is changed according to

$$w_{1,\text{new}} = w_{1,\text{old}} + \frac{\varepsilon_{x,1} - \varepsilon_{\text{des}}}{\varepsilon_{x,2} - \varepsilon_{x,1}} \Delta w. \tag{3.38}$$

This process repeats until either the desired epsilon is found or one of two scenarios is found. These scenarios are as follows

- A maximum is found, but it is still too low. In this case, the number of layers N is increased,

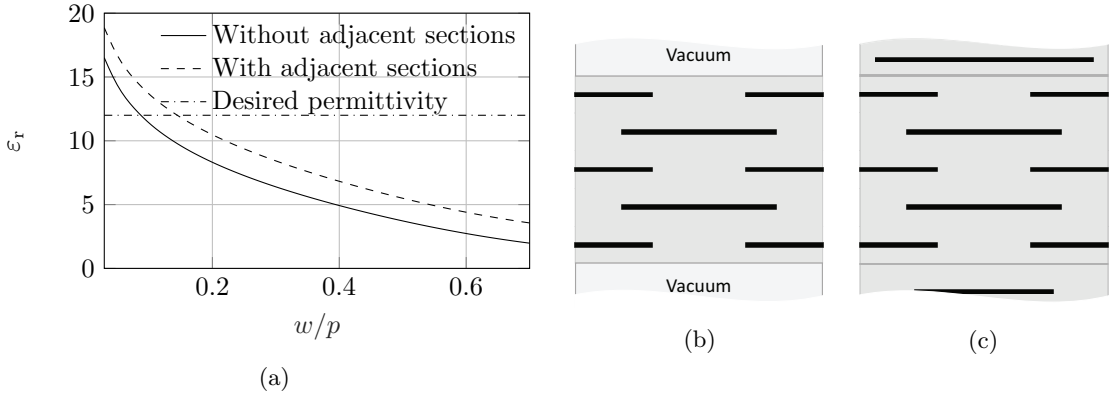

Figure 3.11: Effect of neighboring sections on the permittivity of an ADL section. (a) Behavior of permittivity as a function of gap width w. (b) ADL section in free space, and (c) ADL section with neighboring sections.

resulting in a lower distance between layers $d_z = h_{section}/N$. The process is restarted with the new N.

- The width w reaches the minimum width w_{min} defined by the manufacturing process. This means the desired permittivity is higher than what can be achieved with this number of layers. As before, the number of layers is increased and the process is restarted with the new N.
- A minimum is found, but it is still too high. In this case, either the number of layers N is decreased or, if it is already a single layer, the shift s is reduced to zero. The process is restarted with the new N or s.
- The width w reaches the maximum width w_{max}. This means the desired permittivity is lower than what can be achieved with this number of layers. As before, the number of layers or shift is reduced and the process is restarted.

If the desired permittivity is still lower than what can be achieved with a single layer and zero shift, the desired section cannot be realized without reducing the unit cell size p. Since the number of layers is only increased when the current number of layers is insufficient, the final design will have the minimum number of layers. This is advantageous as each layer adds extra fabrication costs.

3.3.3 Adjacent Sections

Since an impedance transformer often consists of multiple sections, each section is adjacent to one or two other sections. This means that, as follows from the equations in Section 2.2, the susceptances of the metal layers on the edges of each section are influenced by the edge layer in the next or previous section. The effect of the presence of neighboring sections on the behavior of the permittivity is shown in Fig. 3.11, where the permittivity is shown for a section is shown as a function of its gap width w. It is seen that for the desired permittivity, there is a large difference in gap width between the two scenarios. If the effect for the neighboring sections was not taken into account in the design, it is seen that there would be an error of 20% in the realized permittivity of this section.

The effect of the neighboring sections means that each section cannot be designed separately from the others. As such, two design iterations are performed on each section. First with only the previous section, since the rest is unknown. Then again with both the previous section the

previous iteration of the next section. If the number of layers in any section changes during this process, another iteration is done to ensure each layer is optimally close to the desired epsilon.

3.4 Design Performance

To show the accuracy of this method, it is applied to design an 8-section exponential transformer with an impedance transformation from 100 to 377 Ω. The height of the transformer is taken to be $L = 2\lambda_0$ and the unit cell is taken to be $p = 0.225\lambda_0$. Table 3.2 shows that the worst error in this design is approximately 0.1%, along with the parameters of the resulting ADL stack.

This design was generated in an average of 3.77 seconds over 10 runs[1]. In each run, over 14000 different designs are generated, simulated, and homogenized. In a commercial solver such as CST Microwave Studio, the time for a single-frequency simulation of the first section of the generated design is 9.5 seconds, averaged over 10 runs. This shows that it would be infeasible to do this design process in a commercial solver.

[1]Computer used: Dell Optiplex 7050, Intel® Core™ i5-7500 CPU, Intel® HD Graphics 630.

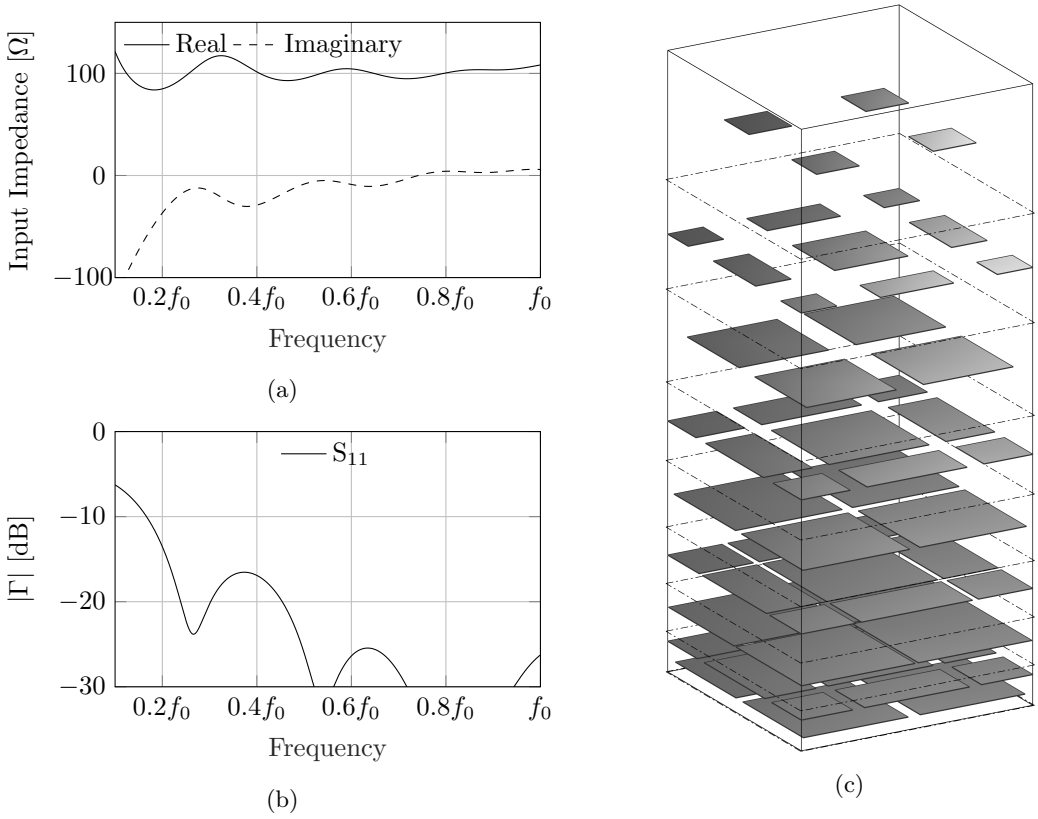

Figure 3.12: (a) Input impedance for a 377-100 Ω exponential transformer using 8 sections and a total electric height of $2\lambda_0$, implemented using 9 ADLs at broadside incidence. (b) Reflection coefficient when matched to 100 Ω. (c) Geometry of the ADL in the design example given in Table 3.2. The sections are shown using dashed lines, and the extent of the unit cell is shown with solid lines.

Table 3.2: Example of an 8-section exponential transformer from 100 to 377 Ω, implemented using ADLs.

Section	$Z_{section}$	$\varepsilon_{r,des}$	Error	d_z (λ_0)	w (λ_0)	s (p)	N
1	108.6597	12.03776	+0.0003%	0.0360	0.0234	0.5	2
2	128.3107	8.63290	+0.0099%	0.0850	0.0068	0.5	1
3	151.4762	6.19432	+0.0785%	0.1038	0.0116	0.5	1
4	178.7545	4.44804	+0.0303%	0.1185	0.0199	0.5	1
5	210.9786	3.19305	+0.0060%	0.1388	0.0327	0.5	1
6	249.0378	2.29166	+0.0014%	0.1651	0.0524	0.5	1
7	293.9625	1.64474	+0.0020%	0.1949	0.0842	0.5	1
8	347.0023	1.18036	-0.1122%	0.2301	0.1428	0.5	1

Chapter 4

Preliminary Design: Design Steps of a Unit Cell

This chapter will detail the steps used to design the wide-band wide-scan connected array antenna array. First, the design of the transformer is discussed in Section 4.1. Next, the design steps for the connected slot unit cell are shown in Section 4.2. After this, the scanning performance is assessed in Section 4.3. Finally, the change to a dual-polarized unit cell is shown in Section 4.4.

4.1 ADL Transformer Design

The design of the antenna array starts with the design of the ADL transformer. For the reasons given in Section 3.1 the exponential transformer is chosen. The feed impedance of the slot is chosen to be $Z_{slot} = 50\,\Omega$, an impedance commonly used for feeding lines.

Using the equations described in Section 3.1, it is found that to obtain a 0.2-1.0f_0 bandwidth, $N = 5$ sections are required. As seen in Fig. 3.6, the upper edge of the $-10\,\text{dB}$ passband is far above f_0, while the lower edge is right on $0.2f_0$. Therefore the height of the transformer is chosen slightly above the theoretical minimum of $1.7\lambda_0$, which moves both the upper and lower edge of the passband to a lower frequency. For this design, the electrical height is chosen to be $L = 2\lambda_0$. This transformer is first implemented in ideal transmission lines, and the reflection coefficient of this transformer when matching free space ($Z_L = 377\,\Omega$) to Z_{slot} is shown in Fig. 4.1a. The parameters of this transformer are shown in Table A.4 in Appendix A. It is seen that the implementation using ideal transmission lines reaches the desired bandwidth, but that the ADL-based implementation does not.

The reason that the ADL-based implementation does not reach the desired bandwidth is due to the frequency dispersive behavior of the metal patches in the ADL. A section consisting of only one or two layers cannot be described as a homogenized medium at all frequencies but only over a narrow bandwidth. The normalized error in the dielectric permittivity of each layer versus frequency is shown in Fig. 4.1b. In this figure, the error is given by

$$\text{Normalized error} = \frac{\varepsilon_{\text{ADL}} - \varepsilon_{\text{desired}}}{\varepsilon_{\text{desired}}}, \tag{4.1}$$

where ε_{ADL} is the permittivity given by the ADL and $\varepsilon_{\text{desired}}$ is the desired permittivity as given by the desired impedance of this section of the transformer. It is seen that the error is highest for the sections consisting of only a single metal layer, and that the error for a high-permittivity section is higher than that of a lower-permittivity section. The figure also shows that there is no error at the chosen design frequency of $0.6f_0$.

To improve the matching at higher frequency, the dispersion is to be reduced. This can be done by increasing the number of layers in a section. This is done in Fig. 4.2a, where the first two sections are now implemented using 1 extra layer each. The parameters of this transformer are

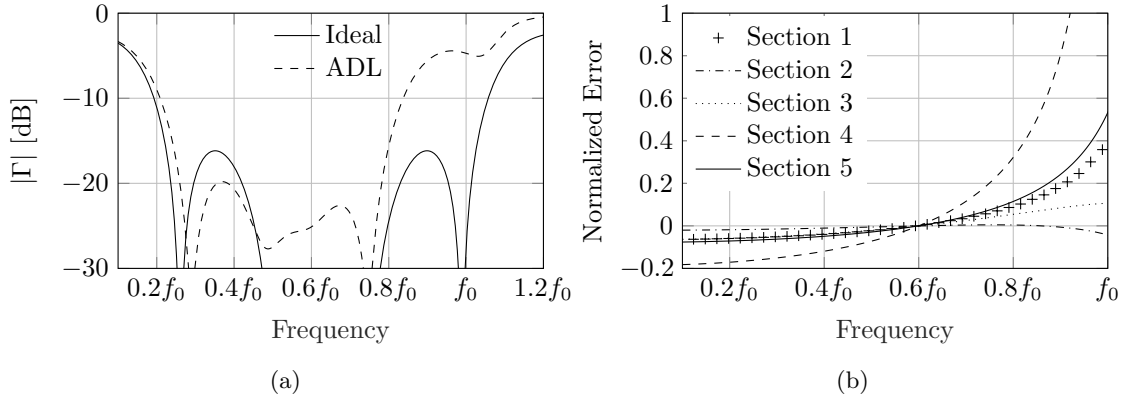

Figure 4.1: (a) Matching performance for a 377-50 Ω exponential transformer using 5 sections and a total electric height of $2\lambda_0$, implemented in ideal transmission lines and 11 ADLs at broadside incidence, matched to 50 Ω. (b) Normalized error between realized and desired permittivity for this transformer.

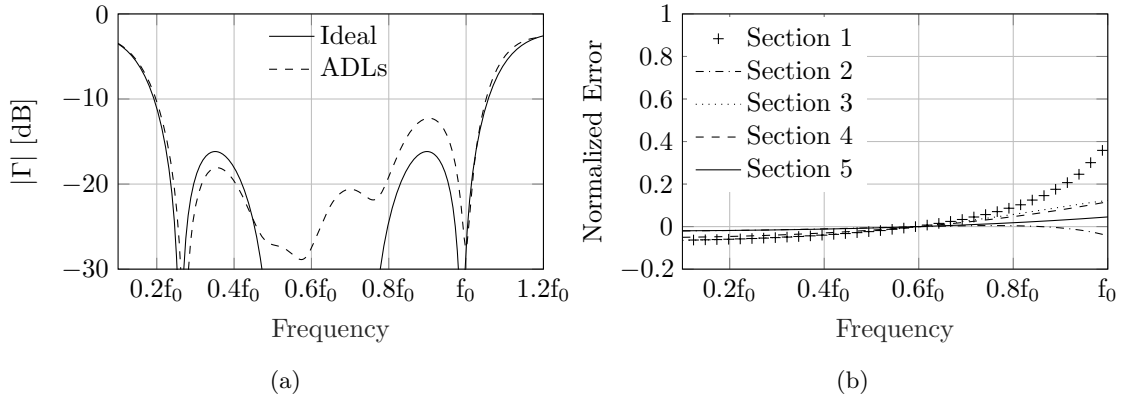

Figure 4.2: (a) Matching performance for a 377-50 Ω exponential transformer using 5 sections and a total electric height of $2\lambda_0$, implemented in ideal transmission lines and 13 ADLs at broadside incidence, matched to 50 Ω. (b) Normalized error between realized and desired permittivity for this transformer.

shown in Table A.5 in Appendix A. It is seen that the high-frequency performance is significantly improved. Fig. 4.2b shows that the dispersion of the first two sections is reduced.

Alternatively, using the same number of metal layers, the number of sections can be increased to 8. Fig. 4.3a shows the performance of this transformer. The parameters of this transformer are shown in Table A.6 in Appendix A. The matching at high frequencies is further improved, and Fig. 4.3b shows that the maximum dispersion is also reduced compared to both previous designs. The dispersion is reduced due to the lower distance between the patches, reducing the impact of frequency on the electric height of the intermediate transmission lines.

The number of layers can be reduced and the matching can be improved by designing the transformer to start from a higher impedance. This is done for Fig. 4.3c, where an 8-section 11-layer 377-80 Ω transformer is shown. The matching is shown to be improved both on the low- and on the high-end of the frequency band. The dispersion for this design, shown in Fig. 4.3d, is similar to the previous design. The parameters of this transformer are shown in Table A.7 in Appendix A. An issue with designing the transformer for this higher impedance is that the feeding network is generally realized using 50 Ω transmission lines, which means that another impedance transformer

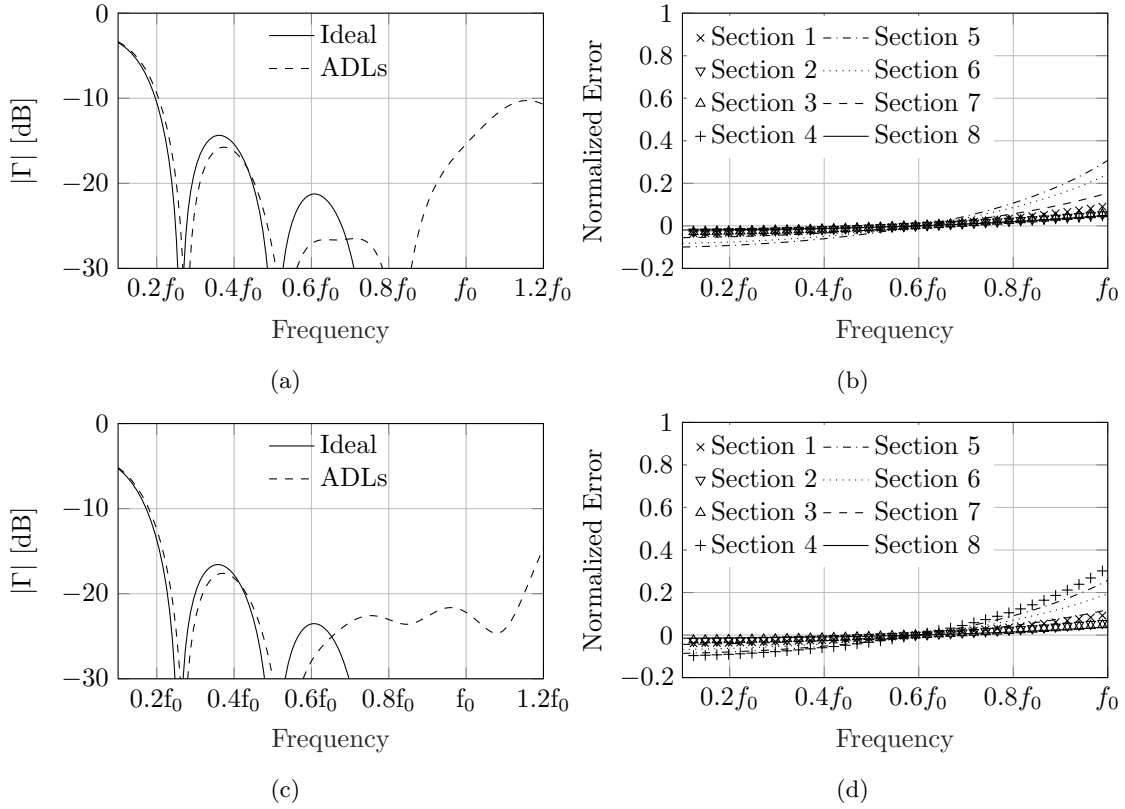

Figure 4.3: Matching performance for an exponential transformer with a total electric height of $2\lambda_0$, implemented in ideal transmission lines and ADLs at broadside incidence. (a)(b) A 377-50 Ω transformer using 8 sections and 13 metal layers, matched to 50 Ω. (c)(d) A 377-80 Ω transformer using 8 sections and 13 metal layers, matched to 80 Ω. (a)(c) Matching performance and (b)(d) normalized error between realized and desired permittivity for this transformer.

from 80-50 Ω is required.

4.2 Slot Design

Once the ADL transformer is designed, the slot itself can be optimized. The slot must be designed such that the input impedance seen from the feeding point is equal to that of the feeding network. The input impedance is a complex value, the slot is matched when the imaginary part is zero and the real part is equal to the impedance of the feeding network. There are several important parameters which impact the behavior of the slot. To show the impact of each of these parameters, the slot is combined with a backing reflector and the 377-80 Ω ADL designed in Section 4.1. The slot is chosen to have a unit cell of $d_x = d_y = 0.45\lambda_0$, with a slot width of $w_s = 0.1\lambda_0$ and a feed length of $d_s = 0.1\lambda_0$. The backing reflector is placed at a distance of $h_{back} = 0.2\lambda_0$. These parameters are summarized in Table 4.1. The parameters of the ADL are shown in Table A.7. The effect of each individual parameter is shown by varying it while keeping other parameters constant.

Backing Reflector Distance

Fig. 4.4a and Fig. 4.4b show the effect on the input impedance of the connected array from varying the distance to the backing reflector from $0.1\lambda_0$ to $0.25\lambda0$ in 4 steps. Several effects are visible as

Table 4.1: Parameters used for validation of implementation connected slot equations.

Parameter	Value	Description
d_x	$0.45\lambda_0$	Unit cell size
d_y	$0.45\lambda_0$	Unit cell size
w_s	$0.1\lambda_0$	Slot width
δ_s	$0.1\lambda_0$	Feed length
h_{BR}	$0.2\lambda_0$	Backing reflector distance

the distance to the backing reflector increases:

- The very low-frequency real impedance increases.
- The high-frequency real impedance decreases.
- The low-frequency imaginary impedance decreases.
- The very low-frequency imaginary impedance increases.

Slot Width

Fig. 4.4c and Fig. 4.4d show the input impedance for a slot width varying from 0.02 to $0.14\lambda_0$. Several effects are visible as the slot width increases:

- The high-frequency real impedance increases.
- The mid- to high-frequency imaginary impedance increases.

The imaginary part shows an inductive effect that appears due to the inductance associated with the feed.

Feed Length

Fig. 4.4e and Fig. 4.4f show the input impedance for a feed length varying from $0.04\lambda_0$ to $0.14\lambda0$ in 4 steps. Only one effect is visible as the feed length increases:

- The mid- to high-frequency imaginary impedance decreases.

The feed of the slot is described as an inductance in series to the fundamental Floquet wave impedance, its value does not affect the real part of the input impedance

Optimisation Process

Using the effects shown before, the array can be optimized such that is has an imaginary impedance close to 0 and a real impedance close to 80 across the $0.2f_0$ to f_0 band. The slot width is increased to increase the high-frequency real impedance, which increases the high-frequency imaginary impedance as well. To compensate for this, the feed length is increased, which again reduces the high-frequency imaginary impedance.

The resulting performance is shown in Fig. 4.5, where the real impedance is seen to closely follow $80\,\Omega$ and the imaginary impedance is close to zero at f_0. At lower frequencies, the imaginary impedance is still quite high, and while changing the backing reflector distance can improve this, it would also worsen the low-frequency real impedance and impact the mid to high frequency imaginary impedance. Instead, to correct this imaginary part, a lumped capacitance is placed in series with the feed. The input impedance to then given by

$$z_{\text{in}} = z_{\text{in,slot}} + \frac{1}{j\omega C}. \tag{4.2}$$

Fig. 4.5 shows the resulting input impedance and reflection coefficient, where a 2 pF capacitance is used. The real impedance is unaffected by the series capacitance and the imaginary impedance is close to $0\,\Omega$ across the 0.2-1.0f_0 band. The reflection coefficient is seen to be below $-14\,\mathrm{dB}$ across this band, meaning the array is well-matched. The parameters used in both of these designs are shown in Table A.1.

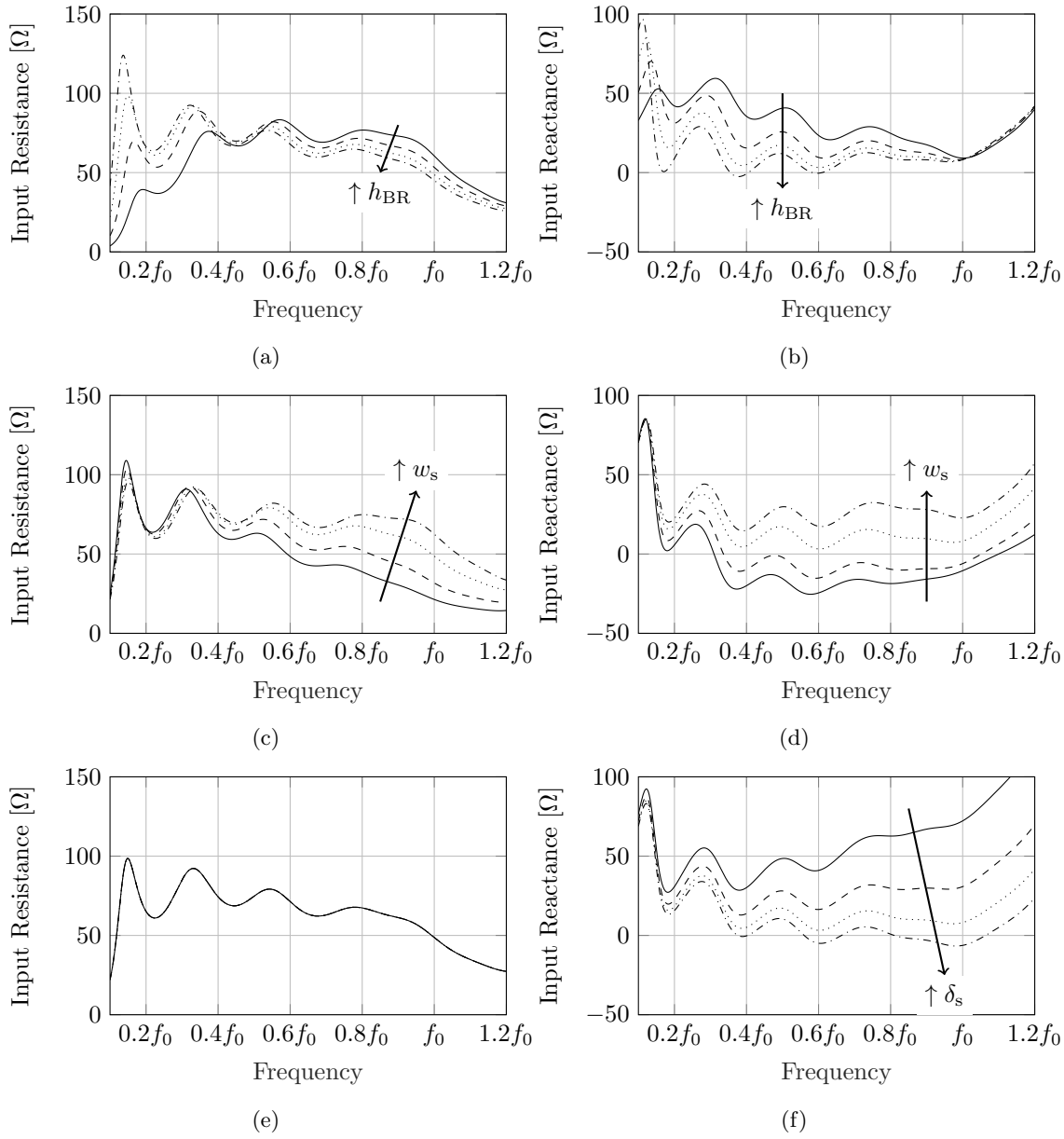

Figure 4.4: Input impedance of a connected slot array while varying (a)(b) backing reflector distance from $0.1\lambda_0$ to $0.25\lambda_0$, (c)(d) slot width from $0.02\lambda_0$ to $0.14\lambda_0$, and (e)(f) feed length from $0.02\lambda_0$ to $0.14\lambda_0$. (a)(c)(e) Real part and (b)(d)(f) imaginary part. Arrows denote the direction of increasing values.

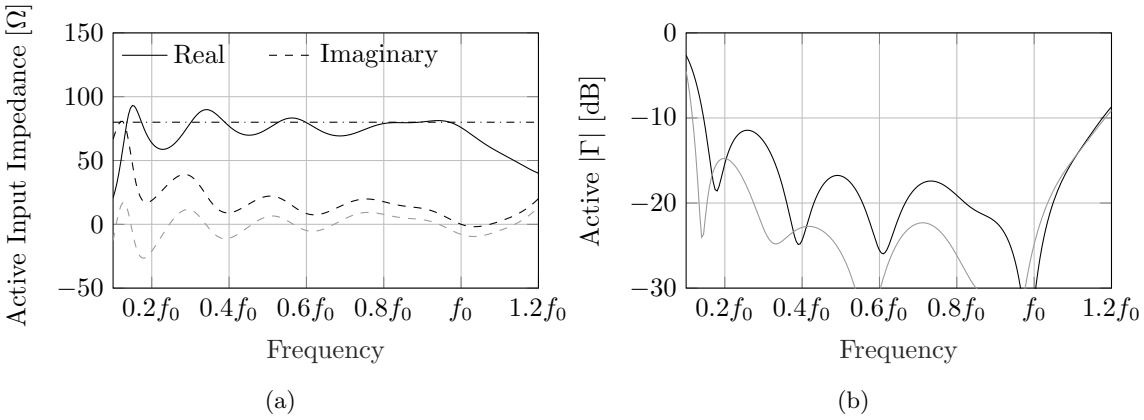

Figure 4.5: Simulated results of optimized design. (a) Input impedance and (b) reflection coefficient when matched to 80 Ω. Impedance and reflection coefficient for series feed capacitance shown in gray.

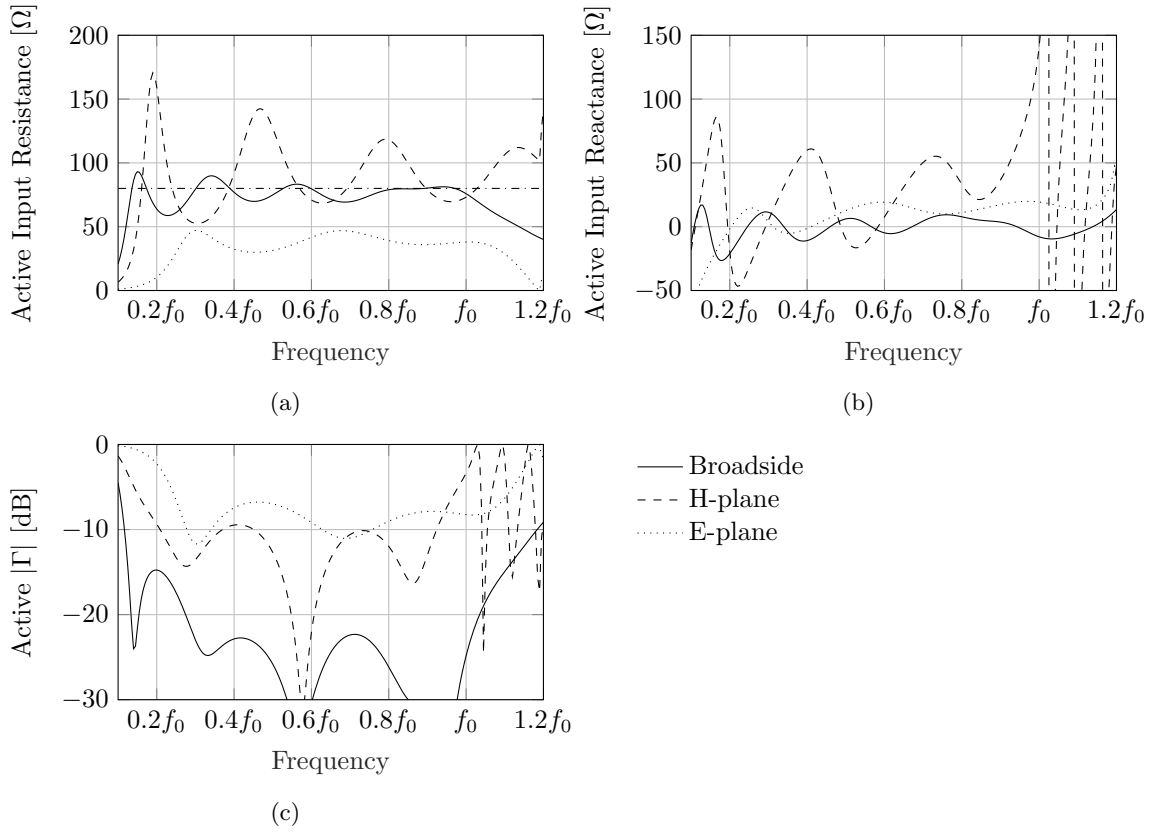

Figure 4.6: Simulated results from scanning the connected array loaded with an 377-80 Ω ADL transformer. (a) Real and (b) imaginary impedance, and (c) reflection coefficient when matched to 80 Ω.

4.3 Scanning the Array

Fig. 4.6 shows the effect of scanning the array described in Section 4.2 to 60°. The angular dependence of the characteristic impedance for the TE and TM polarization [16, app. A] are clearly visible in the real part of the input impedance of the H- and E-plane, respectively. The imaginary impedance is seen to increase for both planes, with oscillations increasing in the H-plane and decreasing in the E-plane due to the aforementioned angular dependence. It is seen that the real and imaginary impedance for both planes are often on opposite sides of the 80 Ω or 0 Ω lines. This means that if for example the high-frequency real impedance is increased, the matching for the E-plane is improved, but the matching for the H-plane deteriorates. As such, each change to the design is a trade-off between performance in the two planes.

The grating lobe is seen through the discontinuity or zero of the real input impedance for the E- and H-plane. It appears at a frequency of $1.19f_0$, which corresponds exactly to the frequency that is expected to appear at, based on the $0.45\lambda_0$ spacing.

H-plane

The H-plane is the plane where the scanning occurs along the slot. It shows three resonances between f_0 and $1.2f_0$, which cause the array to become mismatched. To determine the origin of this resonance, the poles of the dispersion equation of the slot D_∞ and the Green's function of the ADL $G_{xx,\mathrm{up}}$ are analyzed by taking their inverse. Fig. 4.7 shows their inverse as a function of

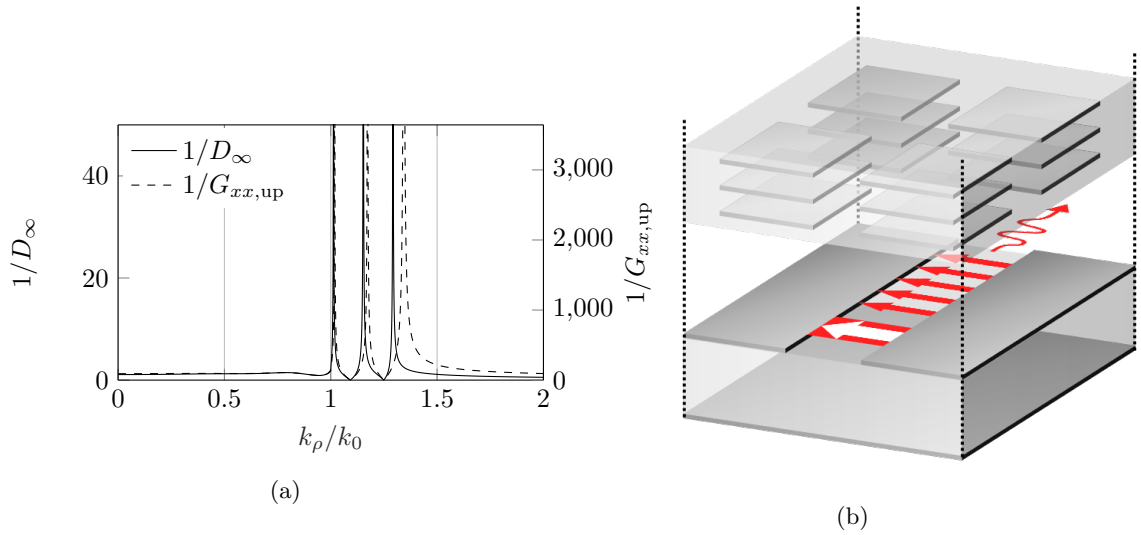

(a) (b)

Figure 4.7: (a) Poles in the stratified Green's function of the ADL stratification and the dispersion equation of the slot. Poles of the design used in Fig. 4.6 are shown, at a frequency of $1.03f_0$. (b) Illustration of the wave guided along the slot.

k_ρ/k_0, the ratio of the transverse propagation constant k_ρ and the propagation constant k_0.

It is seen that there are poles in the Green's function of the ADL $G_{xx,\mathrm{up}}$, and that these are slowed down by the interaction with the slot and backing reflector. The poles are shifted to $k_\rho/k_0 = [1.0130, 1.1528, 1.2924]$ and correspond to waves that are guided by the ADL along the slot, which will be excited when

$$k_0 \sin\theta = \frac{2\pi}{d_x} - k_{\rho,\mathrm{sw}}, \tag{4.3}$$

where θ is the scanning angle. This means that, for scanning to 60°, the surface waves corresponding to these poles are expected at $1.18f_0$, $1.10f_0$, and $1.03f_0$, respectively, which match the frequencies at which they are seen. These poles are not seen in the E-plane because the effective permittivity of the ADL for TM incidence goes to 1, as shown in Fig. 1.3.

E-plane

In the E-plane it is seen that the real impedance remains very low until $0.3f_0$, severely reducing the matching at those frequencies. This is due to the parallel plate waveguide mode between the slots and the backing reflector. This effect is removed by placing vertical metal walls between the slots, as shown in the top of Fig. 4.8, which stop this wave from reaching the next slot. The effect of this is that the scanning angle in the y-direction is no longer relevant for the medium below the slots, resulting in $k_{y0} = 0$ in (2.4). The $2\pi m_y/d_y$ periodicity remains, due to the appearance of virtual sources when the image theorem is applied to the vertical walls. Implementing this change in the equations used to model the slot enables simulation of the slots in the presence of these vertical metal walls. The resulting performance of the array is shown in Fig. 4.8, where it is seen that the real part of the input impedance has improved significantly at low frequencies on the E-plane.

Asymmetry Between Planes

Fig. 4.8b shows that there is an asymmetry between the matching performance of both planes. It is seen that inside the $0.2f_0$ to $0.9f_0$ band, the H-plane performs better than the E-plane, as it has a peak value of $-9.4\,\mathrm{dB}$ versus the $-6.7\,\mathrm{dB}$ of the E-plane. This asymmetry can be reduced by designing the ADL to transform to a higher impedance while still matching the slots to $80\,\Omega$. A

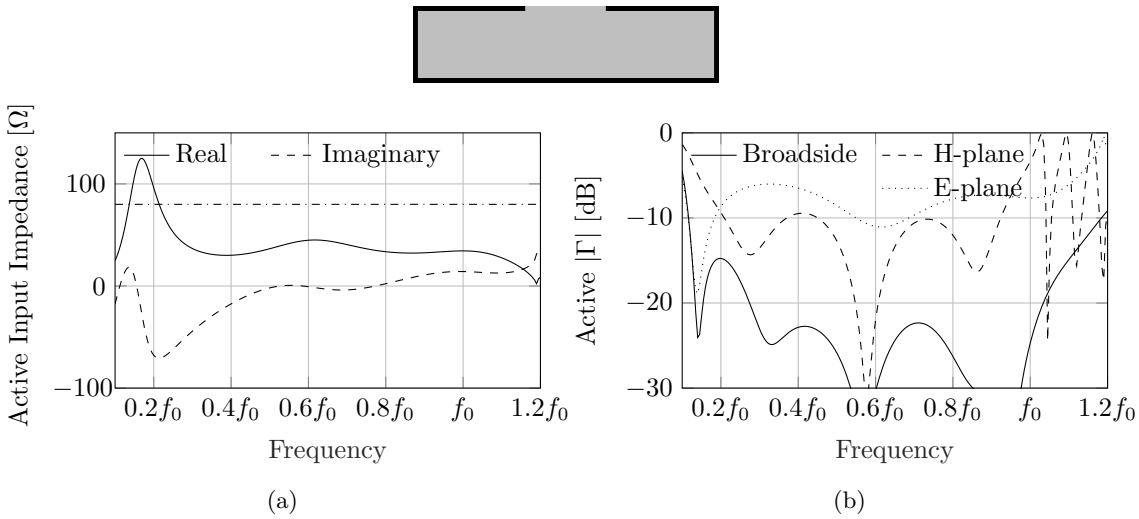

Figure 4.8: Simulated results from scanning the connected array loaded with an 8-section 11-layer 377-80 Ω ADL transformer in the presence of vertical metal walls between the slots in the y-direction. (a) Input impedance on the E-plane and (b) reflection coefficients when matched to 80 Ω.

design where a 377-100 Ω transformer is used is shown in Fig. 4.9. It is seen that the peak value in both planes is now −7.7 dB. The matching is slightly worse at broadside, but it is still well below −10 dB.

Improving Bandwidth

It is seen that the H-plane is mismatched at $0.95f_0$ as the resonance is approached. To improve the matching at this point, the ADL is adapted such that the best matching on the H-plane is achieved right before the resonance. For this, the matching of the ideal discretized exponential transformer is studied when an incident TE-polarized plane wave arrives at an angle of 60°. Fig. 4.10 shows that for the exponential transformer the best matching near f_0 is achieved at $0.72f_0$ and $1.07f_0$.

Due to the strong dependence of both the upper and the lower edge of the passband on the length of the transformer, it is difficult to place the points of optimal matching for an exponential transformer. For this reason, the transformer is changed to a 4-section $5\lambda_0/3$ Chebyshev transformer, which is shown to have its point of optimal matching at f_0 and a better matching across the band when scanning.

The change to the Chebyshev transformer has the additional advantage of having a lower permittivity in its first stage of $\varepsilon_r = 8$ versus $\varepsilon_r = 12$. This means that the guided wave sees a lower permittivity and therefore is excited only at a higher frequency. The matching performance of the slot loaded with this Chebyshev transformer is shown in Fig. 4.11. The matching is below −10 dB for broadside and below −6 dB when scanning on both planes across the $0.2f_0$ to f_0 bandwidth. The parameters used for the slot and the ADL transformer are shown in Appendix A in Table A.8 and Table A.9, respectively.

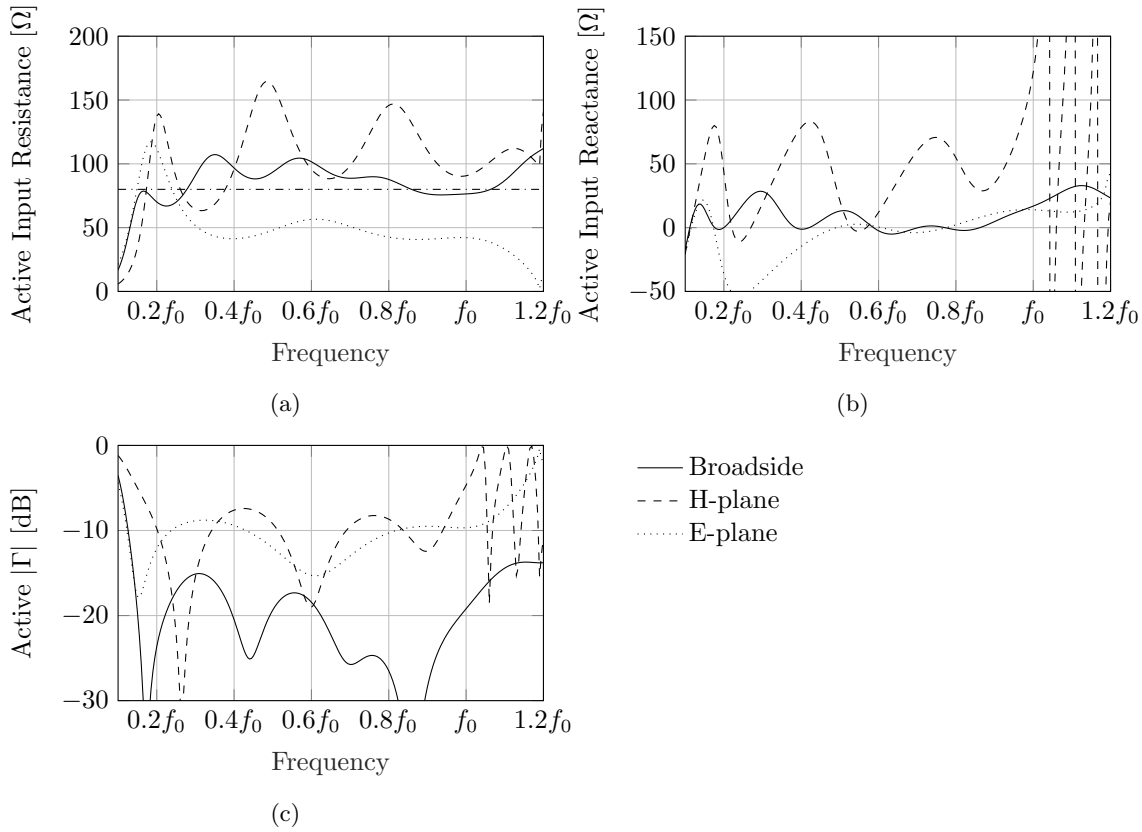

Figure 4.9: Matching performance when scanning the connected array loaded with an 8-section 10-layer 377-100 Ω discretized exponential ADL transformer in the presence of vertical metal walls between the slots in the y-direction. (a) Real and (b) imaginary input impedance, (c) reflection coefficients when matched to 80 Ω.

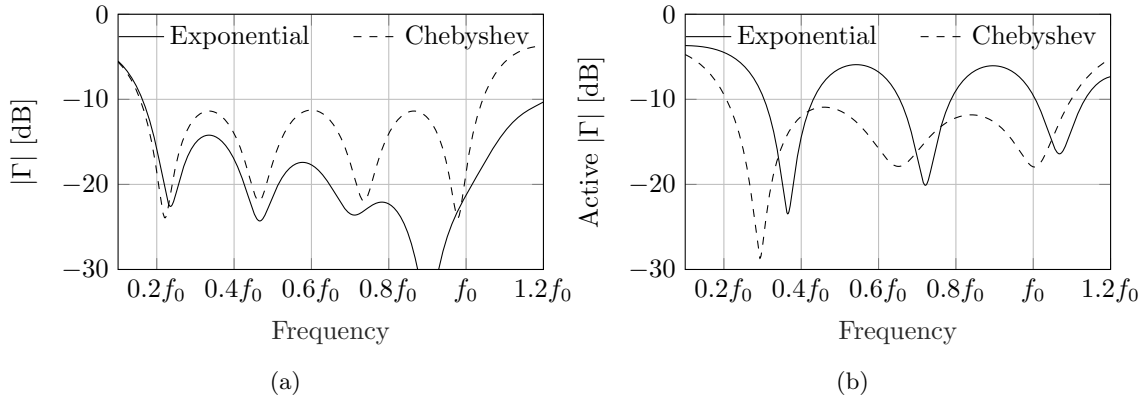

Figure 4.10: Matching performance for an ideal discretized 377-100 Ω $2\lambda_0$ exponential transformer and an ideal 377-94 Ω $5\lambda_0/3$ Chebyshev transformer when matched to 80 Ω. Reflection coefficient shown for TE incidence at (a) broadside and (b) at 60°.

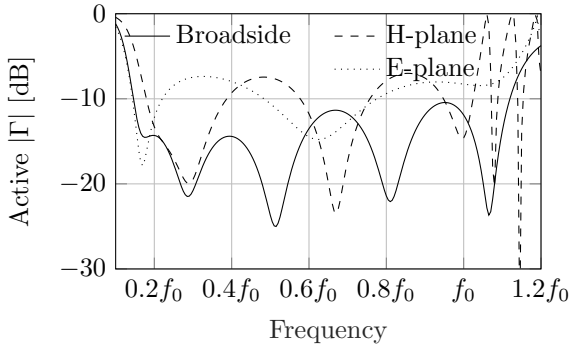

Figure 4.11: Matching performance for an ideal 377-94 Ω $5\lambda_0/3$ Chebyshev transformer when matched to 94 Ω. Reflection coefficient shown for TE incidence at (a) broadside and (b) at 60°.

4.4 Dual-Polarized Slot Design

The equations for the connected array as described in Section 2.1 only account for single-polarized, x-oriented slots. Since a dual-polarized operation is targeted, the design process must continue in a commercial solver. Here, CST Microwave Studio [27] will be used for the rest of the design process. First, the design shown in Fig. 4.9 is placed in CST with a dual-polarized slot layout. Here, the vertical walls present in the simulation of Fig. 4.9 can not be realized since they would interfere with the orthogonal slot. The layout that is used is shown in Fig. 4.12a, the gap between patches in the first layer of the ADL transformer is aligned with the slots, as shown at the top of the figure.

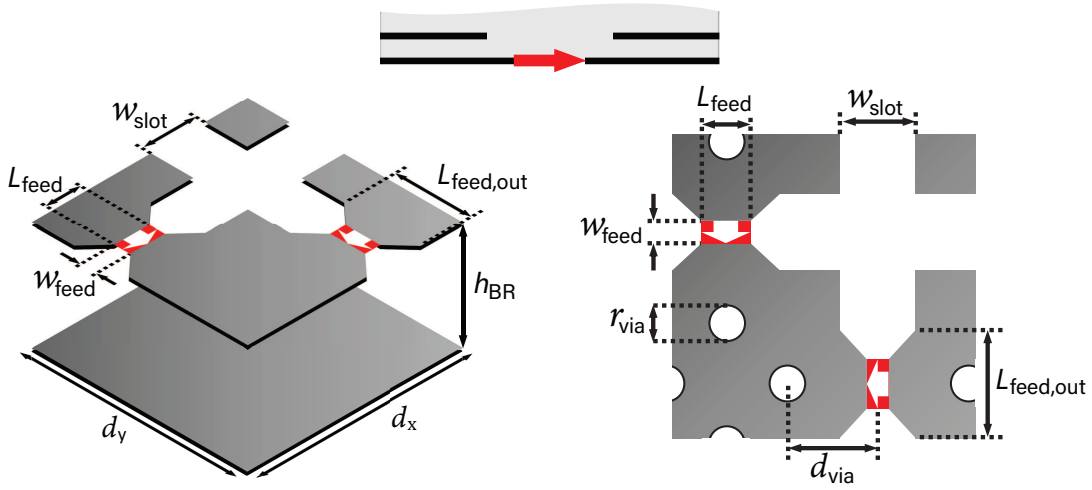

(a) (b)

Figure 4.12: Geometrical parameters of the dual-polarized unit cell (a) without and (b) with vias.

Fig. 4.13 shows the result of this simulation. The response of the x-oriented slot when scanning in its H-plane ($\phi = 0°$) is identical to the response seen by the y-oriented slot when scanning in its H-plane ($\phi = 90°$). The parameters used for the slot and the ADL transformer are shown in Appendix A in Table A.9 and Table A.10, respectively. It is seen that the results are similar to those obtained using the analytical expressions for a single-polarized slot array, except that the guided wave appears earlier than was previously seen, at $1.02f_0$ instead of $1.1f_0$. However, due to the steep slope achieved by placing the point of optimal matching using the Chebyshev transformer, the reflection coefficient is still below $-7\,\mathrm{dB}$ at f_0.

To emulate the effect of the vertical walls used in the previous design, vias are placed between the two orthogonal slots, as shown in Fig. 4.12b. To compensate for the change in reactance, both the width of the slot w_s and the feed length δ_s are reduced to $0.15\lambda_0$. The result of this is shown in Fig. 4.14, where it is seen that the E-plane is improved significantly at the low frequency. The parameters used for the slot and the ADL transformer are shown in Appendix A in Table A.9 and Table A.11, respectively. Both planes are below $-6.5\,\mathrm{dB}$ across the band.

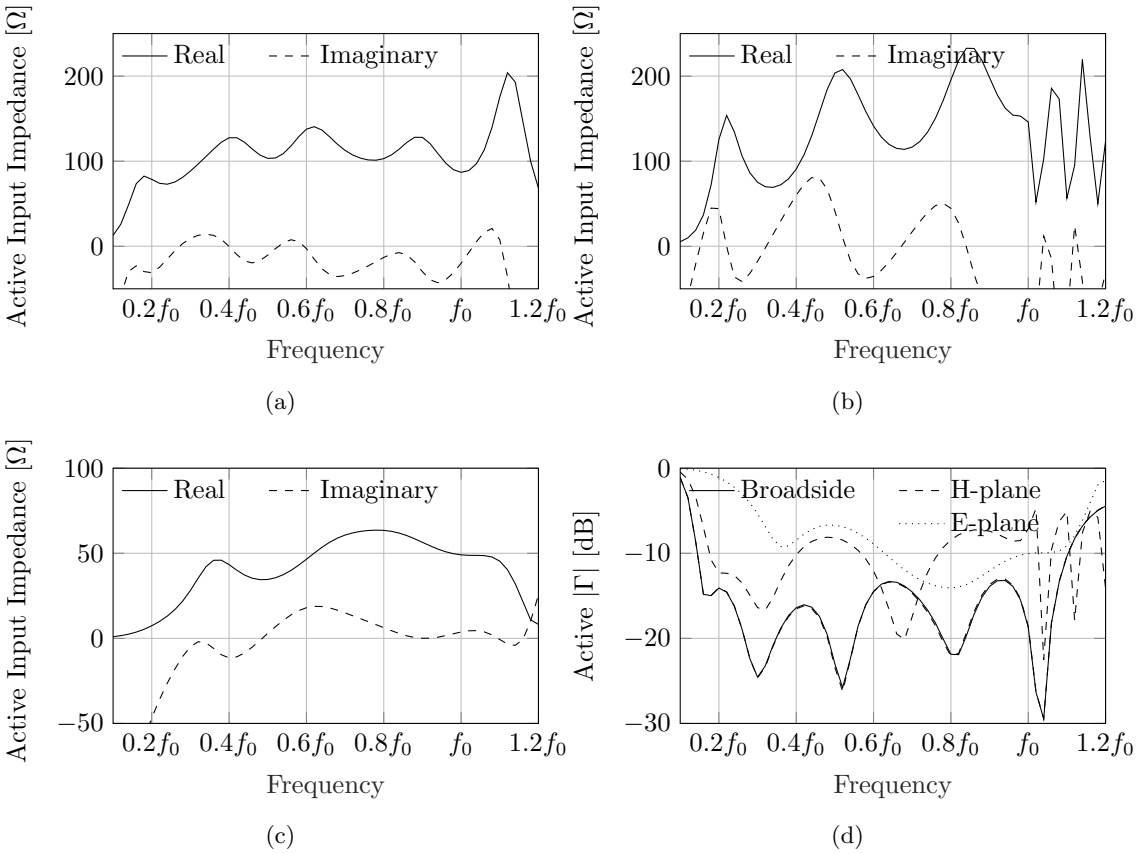

Figure 4.13: Simulation results of a dual-polarized slot loaded with a 4-section 8-layer 377-94 Ω Chebyshev ADL impedance transformer. Input impedance is shown for (a) broadside, scanning to 60° in the (b) H- and (c) E-plane. (d) Reflection coefficients when matched to 94 Ω.

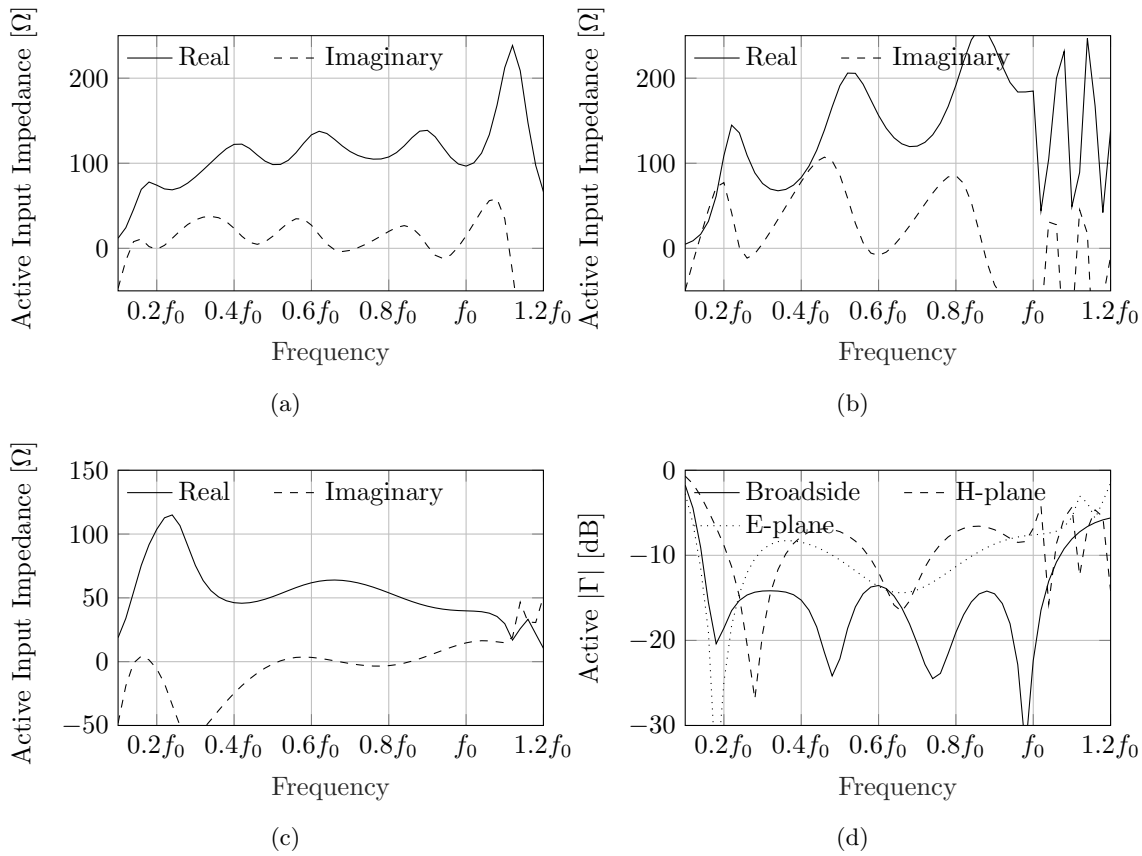

Figure 4.14: Simulation results of a dual-polarized slot loaded with a 4-section 8-layer 377-94 Ω Chebyshev ADL impedance transformer with vias of radius $\lambda_0/30$ at a distance of $d_x/2$ from the center of the slot. Input impedance is shown for (a) broadside, scanning to 60° in the (b) H- and (c) E-plane. (d) Reflection coefficients when matched to 94 Ω.

Chapter 5

Final Design: Realistic Materials and Feed Structure

This chapter will detail the impact of the fabrication process, which imposes limitations on the choice of materials and gives some minimum dimensions. First, the effect of realistic materials on the ADL is shown, and the transmission line model of the ADL is extended to include these materials in Section 5.1 Next, the tolerances in the manufacturing process are discussed in Section 5.2, where their impact on the matching performance is shown. After this, the impact of the PCB of the radiating slot elements is shown in Section 5.3. The design process of the feeding network is then shown in Section 5.4. Finally, the performance of the final design is shown in Section 5.5.

5.1 Fabrication of the ADL

In the previous Chapters, the ADL was modeled as metal patches floating in free space. However, for a realistic implementation, a dielectric stratification to support the patches is needed. A practical example of realization of the ADL was done in [14] using the materials shown in Table 5.1. Since the applicability of these materials to the fabrication of ADLs is proven, they will be used in this study. The foam ROHACELL® 31 HF [28] is used to emulate the free space currently used in the simulation. The copper cannot be placed on a foam substrate, so Dupont™ Pyralux® AP [29] is used upon which the copper is deposited. The layers of foam and substrate are then glued together with CuClad® 6250 [30].

In the derivation of the equations for the ADL, a homogeneous host medium was assumed. However, with the inclusion of the glue layers, the field between the patches will no longer see a constant host medium. This effect is illustrated in Fig. 5.1, where several field lines are drawn in a constant host medium (Fig. 5.1a) and in a layered host medium (Fig. 5.1b). The effective host permittivity seen by the field between the patches is taken as the effective permittivity seen by a wave propagating along the gap between the patches. This was determined for various gap widths w, after which a model was fit to the simulated points to obtain the effective permittivity for any

Table 5.1: Parameters of materials used in the realization of the ADLs.

Material	ε_r	Min. Thickness	Function
ROHACELL® 31 HF	1.045	100 µm	Foam between metal layers.
Dupont™ Pyralux® AP	3.4	25.4 µm	Substrate with copper patches.
CuClad® 6250	2.32	38 µm	Glue used to bond layers together.

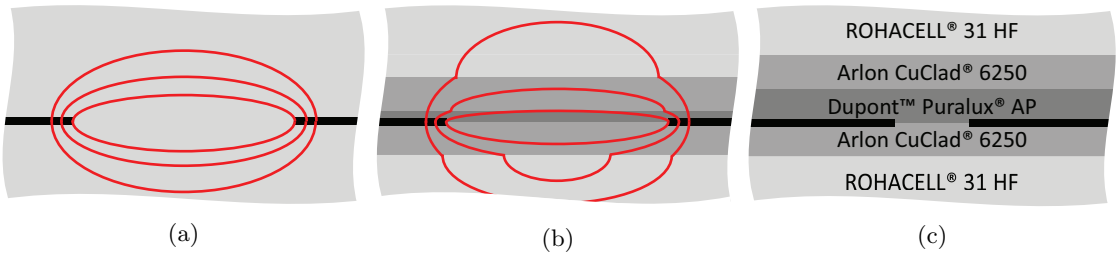

Figure 5.1: Illustration of several field lines in (a) a constant host medium and (b) a layered host medium. The foam-glue-substrate-glue-foam stack is illustrated in (c).

gap width w. The result of this is shown in Fig. 5.2, where the fitted model is of the form

$$\varepsilon_{\mathrm{r,eff}}(w) = aw^b + cw^d + e, \tag{5.1}$$

where the values of a, b, c, d, and e are defined in Table 5.2.

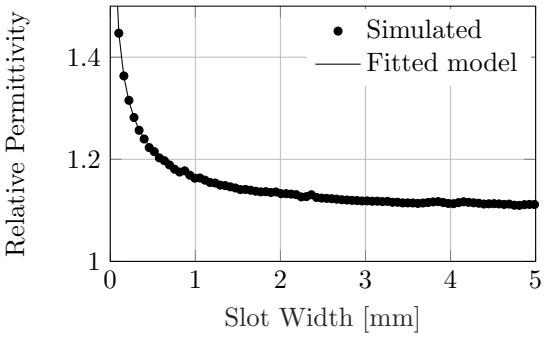

Figure 5.2: Simulated permittivity seen by a wave traveling along a slot inside the stratification shown in Fig. 5.1c.

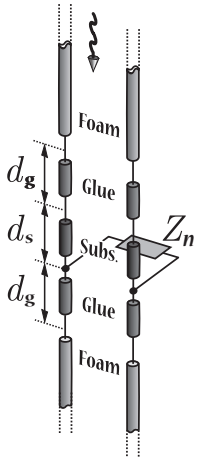

Figure 5.3: Transmission line model for a single layer of metal patches in the presence of the substrate and glue layers.

Using the permittivity found using this model in (2.35) allows calculation of the susceptance of the metal layers in the presence of the realistic stratification. To simulate the behavior of the ADL, the transmission line of the ADL as shown in Fig. 2.9 is adjusted to account for the layers of glue and substrate. This is done by replacing the transmission line for each layer with several sections of transmission lines for each of the layers that are introduced. This adjustment to the transmission line is shown for a single layer in Fig. 5.3, where the lengths d_g and d_s are the thicknesses of the glue and substrate layers, respectively.

Using the effective permittivity seen by the slot allows design of a transformer using the same steps as shown in Chapter 3. The 377-100 Ω discretized exponential transformer used in Fig. 4.9 is reproduced using the realistic materials and the result is shown in Fig. 5.4. It is seen that the matching has deteriorated for broadside, but has dramatically improved for the E-plane due to its higher real impedance across the band. The H-plane is similar at −6.5 dB, but the guided wave has moved to the lower frequency of $0.96f_0$. It is above −6.5 dB starting at $0.85f_0$ due to increase in imaginary impedance leading up to the resonance, but this can again be reduced by placing the point of optimal matching closer to the resonance. Due to the limited effect of the glue layers on the matching performance, and the significant effect on simulation time of the stratification in CST, the design is continued using the free-space version of the ADL transformer.

Table 5.2: Fit parameters of the model used to fit the simulated values shown in Fig. 5.2.

Parameter	Value
a	0.30602
b	-0.35028
c	0.54567
d	0.08426
e	0.31275

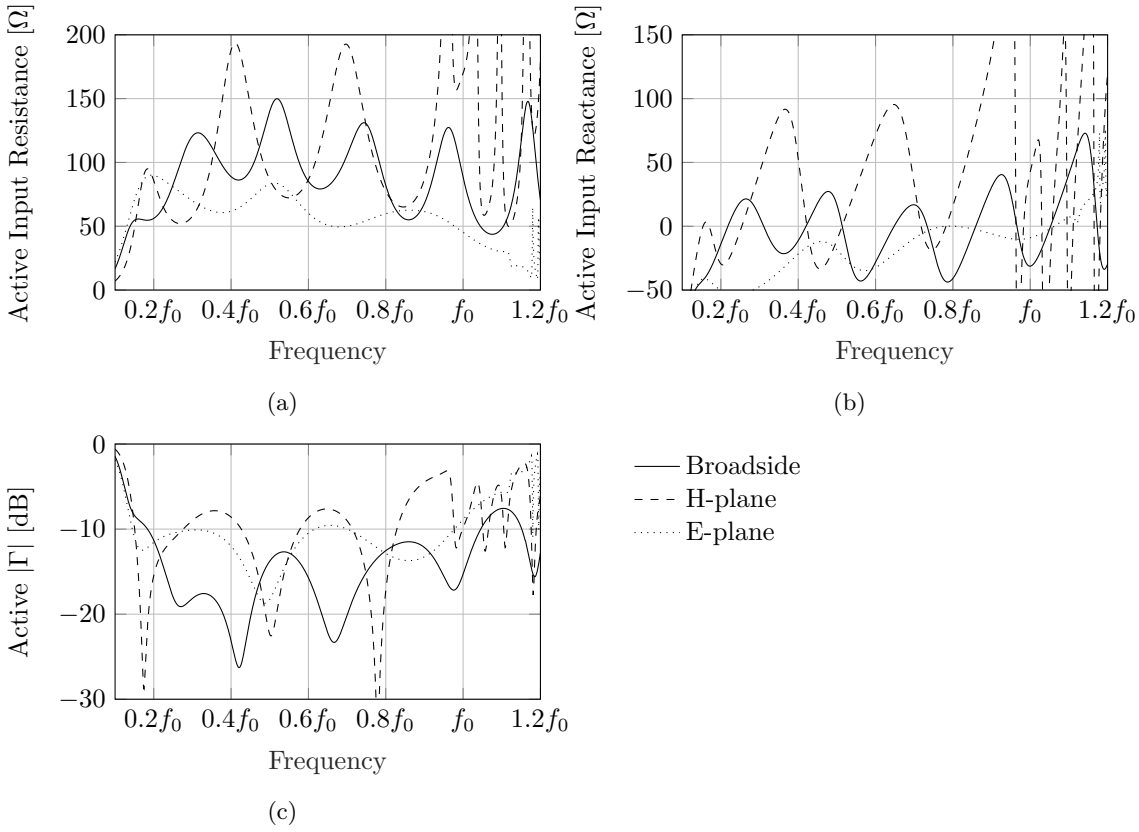

Figure 5.4: Simulation results of a single-polarized slot loaded with a 4-section 8-layer 377-100 Ω discretized exponential ADL impedance transformer in the presence of realistic material layers and vertical metal walls. (a) Real and (b) imaginary input impedance, (c) reflection coefficients when matched to 80 Ω.

5.2 Tolerance Study

To study the effect of inaccuracies in the manufacturing process, a tolerance study is performed on the ADL impedance transformer. The effect of these inaccuracies is determined by applying them on the parameters of the 377-100 Ω discretized exponential transformer in Fig. 4.9. Each parameter is randomly adjusted within the manufacturing tolerances and 100 simulations are run, of which the best and worst matching are shown for broadside and for scanning to 60° in the H- and E-plane. The tolerances used for the various parameter are as follows:

- The shift s is adjusted by up to 1 mm.
- The width w of the gap between patches is adjusted by up to 20 µm.
- The distance d_z between the metal layers is adjusted by up to 5%.

Layer Misalignment

Since the ADL is constructed using many alternating layers of foam and dielectric, the layers must be independently aligned and glued together. If the layers are misaligned, the shift between the layers of metal patches is affected, causing the susceptance of each metal layer to change. Fig. 5.5a shows the original matching performance and the range in which it will be when the alignment between each layer of metal patches has an error of up to 1 mm. It is seen that there is little effect on the matching performance at broadside or either of the scanning planes.

Patch Size Variation

The production process of the metal patches that make up the layers of the ADL may introduce an error on the size of each patch. This error in the size of the patches means there is a change in the gap width between the metal patches. The susceptance of each layer of metal patches will change as a result, changing the effective permittivity of the ADL. Fig. 5.5b shows the original matching performance and the range in which it will be when the gap between the metal patches has an error of up to 20 µm. It is seen that there is little effect on the matching performance at broadside or either of the scanning planes.

Layer Distance

The distance between the metal layers of the ADL is determined by the thickness of the foam layers between them. The thickness of these foam layers may vary slightly, causing the susceptance of each layer of metal patches to change, but also changing the length of the transmission line sections between the layers. Fig. 5.5b shows the original matching performance and the range in which it will be when the height of each foam layer has an error of up to 5%. It is seen that the effect of this is larger than the effect of the layer misalignment and gap width, but is still limited to within 1 dB on the E- and H-planes.

Aggregate Tolerance Effects

When combining all of the aforementioned tolerances, the number of permutations increases significantly. Due to this higher number of permutations, the number of simulations where all three of these parameters are adjusted randomly is increased to 1000. The best and worst-case changes in matching performance are shown in Fig. 5.5d, where it is seen that the matching at broadside may decrease significantly, but is still well below −10 dB across the $0.2f_0$ to f_0 band. The matching on the H-plane is still within 1.7 dB of the original matching at its point of worst matching, which is around $0.8f_0$. The E-plane is within 1.1 dB of the original matching at its point of worst matching, which is around $0.9f_0$.

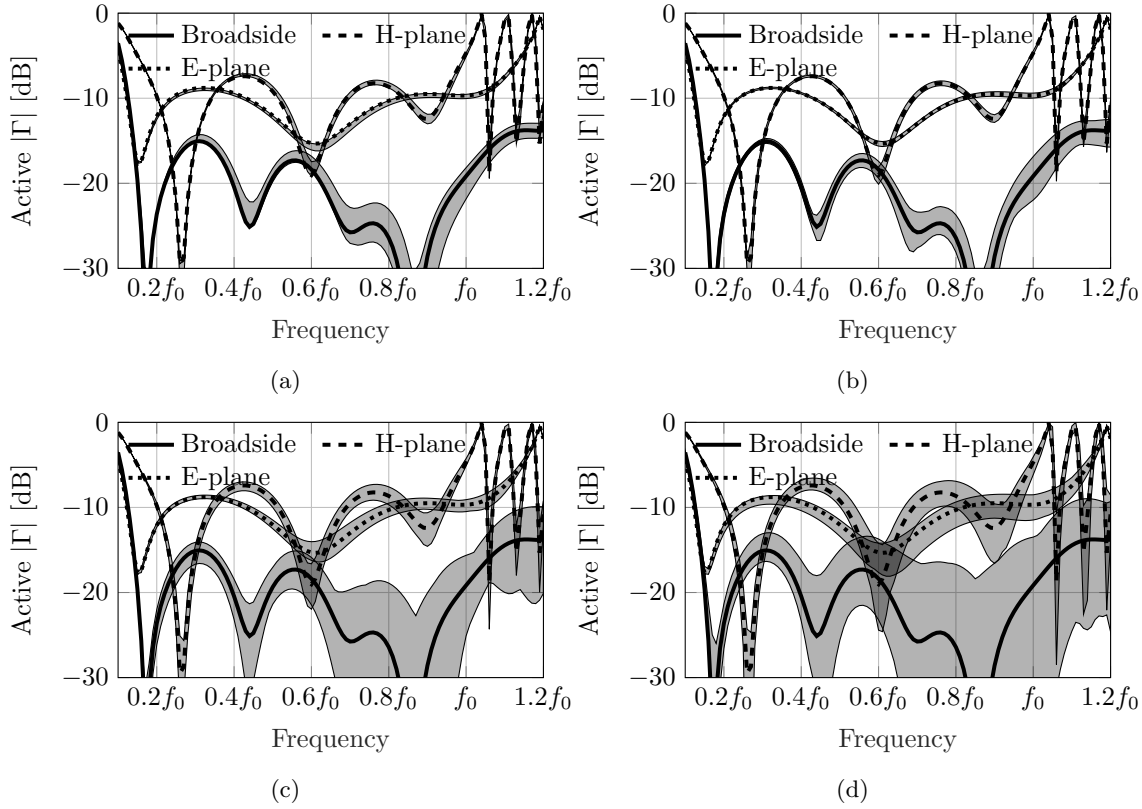

Figure 5.5: Effect of manufacturing tolerances on the active matching of a connected slot array with 377-100 Ω discretized exponential ADL impedance transformer. (a) Up to 1 mm error in the shift between layers. (b) Up to 20 µm error in the gaps between patches. (c) Up to 5% error in the distance between metal layers. (d) All of the errors combined.

5.3 PCB of Radiating Slot Elements

The substrate between the slot plane and the backing reflector is to be manufactured using Rogers RO4350B$^{\text{TM}}$ [31]. This material has a permittivity of $\varepsilon_r = 3.66$.

Cavity Resonance

Fig. 5.6a shows the effect of the substrate material, where the design from Fig. 4.8 is adjusted to include the substrate material below the slot. A narrow resonance is visible at $0.62f_0$, where the matching is severely impacted. This resonance is due to a standing wave that forms between the vertical walls between the slots, illustrated at the top of Fig. 5.6b. It can be shifted to a higher frequency by changing the horizontal electrical size of the cavity below the slot. The horizontal size of the cavity can be adjusted by increasing the thickness of the vertical metal walls, as is shown at the bottom of Fig. 5.6b. The result of the thicker walls is also seen in Fig. 5.6a, where it is seen that the resonance is shifted from $0.62f_0$ to $0.79f_0$. The parameters of the slot and the ADL transformer are found in Appendix A in Table A.12 and Table A.7, respectively.

The thickness of the walls can be chosen such that the resonance is outside of the frequency band of interest. However, to move the resonance shown in Fig. 5.6 beyond f_0 requires the width of the cavity to be reduced by 45%, where it will severely impact the matching obtained for the slot unit cell. The horizontal electric size can also be adjusted by lowering the effective dielectric constant of the substrate material. The effective dielectric constant is lowered by cutting away

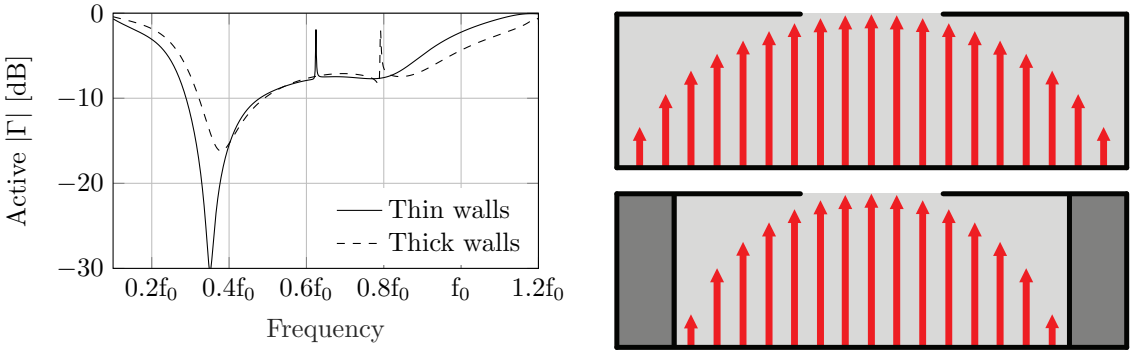

(a)

(b)

Figure 5.6: Response of a 377-80 Ω discretized exponential ADL transformer when the substrate material (Rogers 4350B$^{\text{TM}}$) is introduced. (a) Reflection coefficient for thin walls and walls that reduce the cavity width by 20%, when matched to 80 Ω. (b) Illustration of the standing wave at the frequencies of the resonances shown in (a).

part of the material below the slot. The cut shown in Fig. 5.7b is made in the substrate of the design shown in Fig. 5.6, with $w_{\text{cavity}} = 4\lambda_0/15$ and $d_{\text{ms}} = 0.0085\lambda_0$. The result of this is shown in Fig. 5.7a, where the resonance is seen to have shifted from $0.62f_0$ to $0.91f_0$.

In a dual-polarized design, the effect of the thicker walls is emulated by placing the vias closer to the feeds of the slots. The cavity in the dual-polarized design is shown in Fig. 5.7c. A bridge is introduced across the gap to ensure that the substrate is a continuous slab of material without islands.

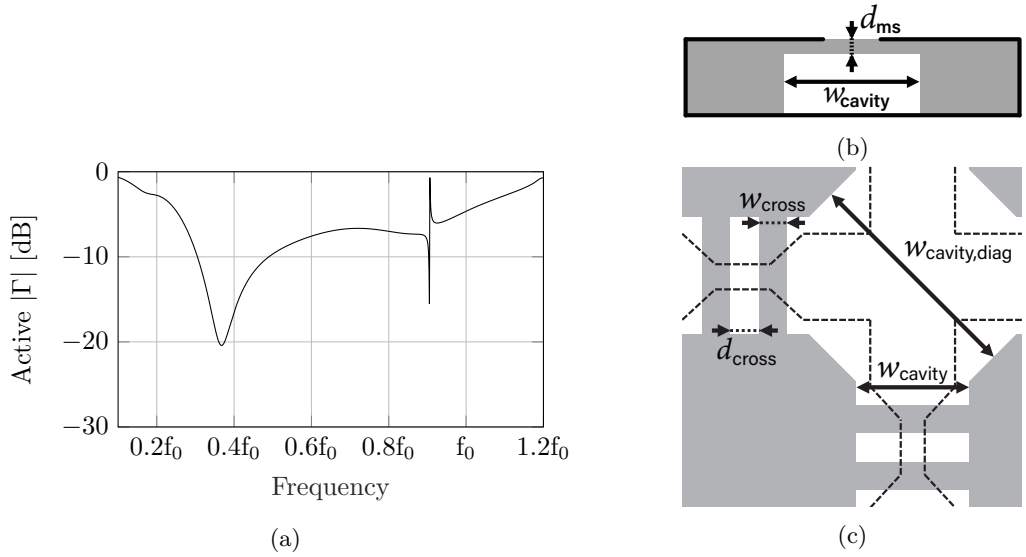

Figure 5.7: Response of a 377-80 Ω discretized exponential ADL transformer when the substrate material (Rogers 4350B^{TM}) is introduced which is partially cut away. (a) Reflection coefficients when matched to 80 Ω. (b) Shape of the cut in the substrate for a single-polarized slot. The substrate material is shown in grey, and the cut part is shown in white. (c) Shape of the cut in the substrate in a dual-polarized slot unit cell. The metal plane is shown in dashed lines.

5.4 Feed Design

The designs thus far have all used ideal feeding ports located in the slot plane. This is unphysical, so this section will detail the design process of the feeding structure that will implement a transition from a 50 Ω coaxial feeding cable to the feeding point in the slot plane. The feed consists of two sections, an integrated coaxial cable implemented using vias, and a microstrip section that feeds the slot itself. This structure is shown in Fig. 5.8, where the geometrical parameters are highlighted. The feed design is done separate from the slot and impedance transformer, and is designed such that it matches an 80 Ω impedance at the slot plane to the 50 Ω impedance of the port at the ground plane.

5.4.1 Narrowing of the Slot

Thus far, the feeding point has been as wide as the slot w_s and has had a feed length of δ_s. To approximate such a feed, a very wide microstrip would be necessary, which would have a very low

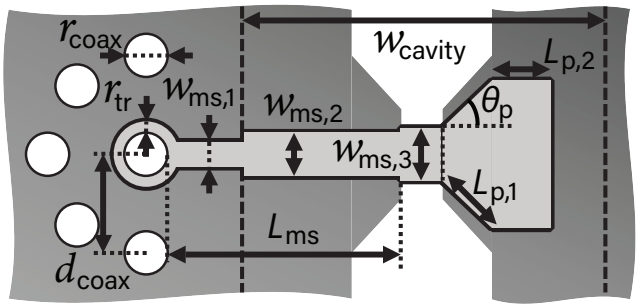

Figure 5.8: Illustration of the feed shape with geometrical parameters.

Table 5.3: Parameters used in the sweep of various patch areas.

Parameter	Value
$w_{\mathrm{ms},3}$	$0.0073\lambda_0$
$L_{\mathrm{p},1}$	$0.0667\lambda_0$
$L_{\mathrm{p},2}$	$0.0007\lambda_0 to 0.0292\lambda_0$
θ_{p}	55°
A_{patch}	$0.0024\lambda_0^2 to 0.0058\lambda_0^2$

line impedance. To be able to use a narrower microstrip, the slot is narrowed at the point where the feed is to be located. This narrowing was already shown in the geometry of the dual-polarized slot in Fig. 4.12a, where the slot width and feed width were separated into two parameters w_{slot} and w_{feed}, respectively. Similarly, the feed length and the length of the narrowing were separated into L_{feed} and $L_{\mathrm{feed,out}}$. This gives two more parameters to use in optimization of the design. Fortunately, the input impedance remains similar if the ratio of w_{feed} and L_{feed} is kept similar to the ratio of w_s and δ_s.

5.4.2 Microstrip Feed and Series Capacitance

The narrowing in the slot is fed using a microstrip, which is placed on the bottom of the top dielectric plane shown in Fig. 5.7b. The series capacitance that was introduced in the feed in Section 4.2 is implemented by placing a patch at the end of the feed microstrip, as illustrated in Fig. 5.8.

To see the effect of replacing the ideal feed with the microstrip and of replacing the lumped series capacitance with the patch, the 377-100 Ω discretized exponential transformer from Fig. 4.9 is placed over a dual-polarized slot plane of which the parameters are shown in Table A.13. In this simulation, the Rogers 4350B$^{\mathrm{TM}}$ substrate is present with the cavity cut shown in Fig. 5.7c. It is seen that the effect of the microstrip feed can be compensated by adjusting the slot parameters. Various patch areas are simulated, and it is seen that the area of the patch has limited influence on the real impedance, while it has the desired effect on the imaginary impedance. It is seen that the capacitance of the patch is frequency dependent, since the imaginary input impedance of the shorted microstrip with lumped capacitance crosses that of various patch areas. The parameters of the microstrip and the patch are shown in Table 5.3. In this simulation, only section 3 of the microstrip and the patch are present.

The area of the patch A_{p} replaces the parameter C in the design of the slot, and determines value of the series capacitance. The area of the patch A_{patch} is given in terms of the parameters that describe the geometry of the patch as

$$A_{\mathrm{patch}} = W_{\mathrm{ms},3} L_{\mathrm{p},1} \cos\theta_{\mathrm{p}} + L_{\mathrm{p},1}^2 \cos\theta_{\mathrm{p}} \sin\theta_{\mathrm{p}} + 2L_{\mathrm{p},1} \sin\theta_{\mathrm{p}} L_{\mathrm{p},2} \,. \tag{5.2}$$

The width $W_{\mathrm{ms},3}$ is fixed based on the design of the microstrip, and the angle θ_{p} and the length $L_{\mathrm{p},1}$ are chosen as $\theta_{\mathrm{p}} = 55^\circ$ and $L_{\mathrm{p},1} = \lambda_0/15$. With these parameters fixed, the final parameter of the patch $L_{\mathrm{p},2}$ is found as

$$L_{\mathrm{p},2} = \frac{A_{\mathrm{patch}} - W_{\mathrm{ms},3} L_{\mathrm{p},1} \cos\theta_{\mathrm{p}} + L_{\mathrm{p},1}^2 \cos\theta_{\mathrm{p}} \sin\theta_{\mathrm{p}}}{2L_{\mathrm{p},1} \sin\theta_{\mathrm{p}}} \,. \tag{5.3}$$

The widths of first two sections of the microstrip $W_{\mathrm{ms},1}$ and $W_{\mathrm{ms},2}$ are chosen based on the impedance that is to be realized in the microstrip. The width of the third section, $W_{\mathrm{ms},3}$, is chosen based on the length of the feeding gap L_{feed} and is chosen such that it approximates the constant field over the slot that was present with the delta-gap feed.

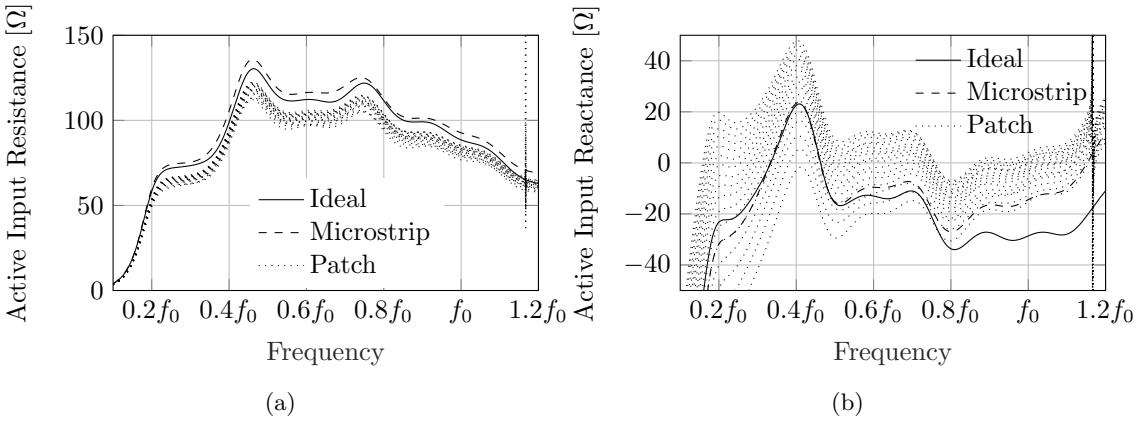

Figure 5.9: Simulation results of a single-polarized slot loaded with a 8-section 10-layer 377-100 Ω discretized exponential ADL impedance transformer. The slot is fed by an ideal port, a shorted microstrip feed or a microstrip terminated with a patch of increasing area.

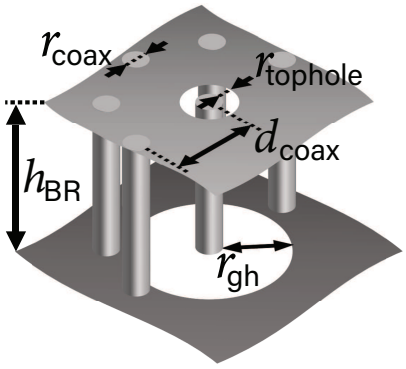

Figure 5.10: Illustration of the integrated coaxial line with geometrical parameters.

5.4.3 Feed Impedance Transformer

The antenna is to be fed at the ground plane using a 50 Ω coaxial line. This means that the energy must be guided from a hole in the ground plane to the slot plane. This is done using an integrated coaxial line, of which the shape is shown in Fig. 5.10. It is seen that all vias extend from the ground plane to the slot plane, and that the top of the central via is insulated from the slot plane using a hole. The hole in the ground plane that is to connect to the 50 Ω coaxial input line is also shown. This integrated coaxial line replaces one of the vias shown in Fig. 4.12b, as it has the same effect on the cavity resonance.

Design of the Integrated Coaxial Line

The integrated coaxial of the desired impedance is realized by adjusting the ratio between the diameter of the inner conductor and the radius of the circular via wall composing the out conductor. The parameters are selected such that the maximum aspect ratio for the fabrication of the via is not exceeded.

For a normal coaxial line, the impedance is given in [32] as

$$Z_{\text{coax}} = \frac{1}{2\pi}\sqrt{\frac{\mu}{\varepsilon}}\log\left(\frac{r_{\text{outer}}}{r_{\text{inner}}}\right), \tag{5.4}$$

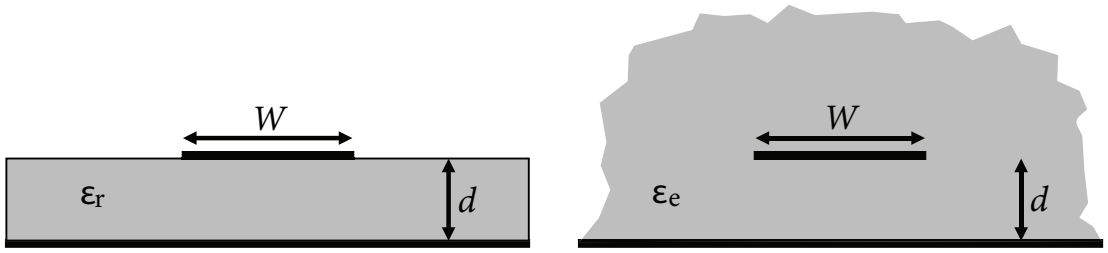

(a) (b)

Figure 5.11: Illustration of the geometry of a microstrip line. (a) Original geometry of a microstrip on a dielectric substrate with permittivity ε_r. (b) Equivalent geometry with a permittivity ε_r given by (5.6). Figure reproduced from [25].

where r_outer and r_inner are the radii of the inner and outer conductor, respectively, and μ and ε are the permeability and permittivity of the host medium. However, since the integrated coaxial line will only have vias that approximate a half outer conductor, the impedance of this line will be higher than that of a normal coaxial line. Conversely, the integrated coaxial line will be implemented near the edge of the cavity, where the permittivity is that of free space. This reduces the effective permittivity seen by a wave traveling on the coaxial line, which will lower the impedance. This second effect is much smaller, since most of the field is concentrated between the conductors, and only little will be near the boundary between the dielectric and the cavity. Overall, the impedance of the integrated coaxial line is approximately 15-20% higher than that of a normal coaxial line.

Design of the Microstrip Line

The impedance of the microstrip depends on the ratio of the width W of the microstrip and the distance from the strip to the ground plane d. It is given in [25] as

$$Z_0 = \begin{cases} \dfrac{60}{\sqrt{\varepsilon_e}} \log\left(\dfrac{8d}{W} + \dfrac{W}{4d}\right) & \text{for } W/d \leq 1 \\ \dfrac{120\pi}{\sqrt{\varepsilon_e}\left[W/d + 1.393 + 0.667 \log\left(W/d + 1.444\right)\right]} & \text{for } W/d > 1, \end{cases} \tag{5.5}$$

where ε_e is the dielectric constant of a homogeneous medium that replaces the interface between the host medium and free space, and is given by

$$\varepsilon_e = \frac{\varepsilon_r + 1}{2} + \frac{\varepsilon_r - 1}{2} \frac{1}{\sqrt{1 + 12d/W}}\,. \tag{5.6}$$

It is shown in Fig. 5.8 that the microstrip consists of three sections, sections 1-3. Section 1 is fully buried in the dielectric of the substrate, and will see $\varepsilon_e = \varepsilon_{r,\mathrm{substrate}}$. Section 2 is on a dielectric-air interface and will see a ε_e as given by (5.6). Section 3 is used to feed the slot, and its width is not determined by a desired impedance but by the desired length of the feeding point in the slot L_feed.

Chebyshev Impedance Transformer

Since the feed will consist of two main sections - the integrated coaxial and the microstrip - a 2-section Chebyshev transformer is designed to transform from the $80\,\Omega$ port on the slot plane to the $50\,\Omega$ port on the ground plane. The distance to the backing reflector is fixed by the design of the slot array, which means that the height of the integrated coaxial cable may not be exactly quarter-wave.

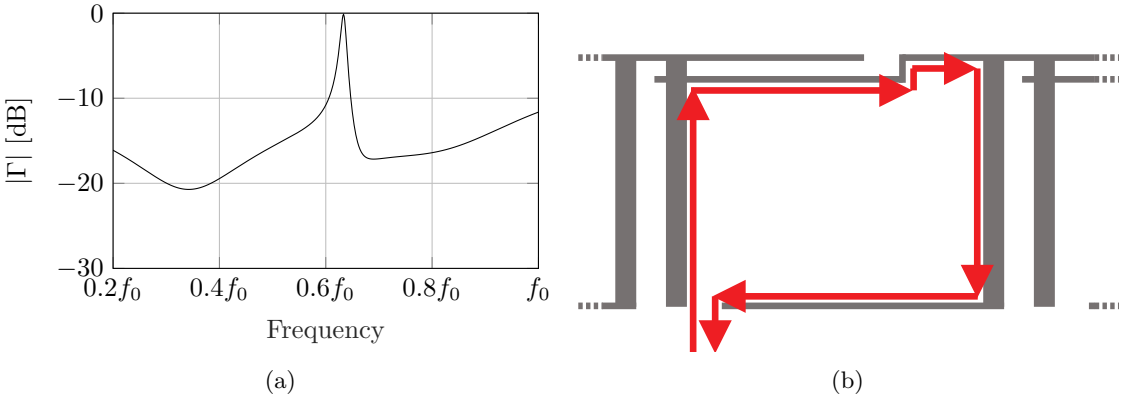

Figure 5.12: (a) Response of a two-section 80-50 Ω Chebyshev impedance transformer when loaded with 80 Ω and matched to 50 Ω. (b) Illustration of the loop current that causes the resonance visible in (a).

An initial design was done for this transformer, where line impedances of 71 Ω and 57 Ω are realized in the coaxial and microstrip sections, respectively. The lengths of the sections are given by $h_{\mathrm{BR}} = L_{\mathrm{ms}} = 0.4\lambda_d$, where λ_d is the wavelength in the dielectric of the substrate, this makes them quarter-wave at $0.62\lambda_0$. The resulting performance is shown in Fig. 5.12, where it is seen that it is below −11.5 dB across the $0.2f_0$ to f_0 band. The parameters used in this simulation are shown in Table A.14. However, a resonance is visible at $0.63f_0$, which appears because the current in the feeding network approaches a loop antenna with a length of λ_0. This loop antenna is illustrated in Fig. 5.12b, where the current enters through the inner conductor of the coaxial cable at the ground plane, travels up along the inner via of the integrated coaxial line, then travels right along the microstrip and slot plane, then down along the outer conductor of the feed in the next unit cell, and back left along the ground plane.

This loop resonance can be shifted out of the band of interest by shortening the path of this current, which can be done in several ways:

1. Reduce the size of the unit cell.
2. Introduce the vias for the cavity resonance and move them closer to the slot.
3. Move the integrated coaxial line closer to the slot.
4. Shorten the length of the coaxial line.
5. Shorten the microstrip.

Option 1 is impossible as it conflicts with the requirements set on the project. Option 2 is limited due to the distance of the via affecting the matching if it is placed very close to the slot. Option 3 can be achieved by curving the microstrip, but only has limited effect on the length of the current path due as the length along the microstrip remains the same. Option 4 is infeasible since this parameter is fixed by the optimization of the slot parameters. Option 5 cannot be used if the 80-50 Ω impedance transformation is to be done using two sections. To move this loop resonance out of the desired bandwidth, the path of the current has to be reduced by 40%, which cannot be achieved within the limits on the options discussed above.

Quarter-wave Impedance Transformer

To sufficiently shorten the current path, the impedance transformation is done using a single quarter-wave section implemented in the integrated coaxial line. This allows it to be moved to

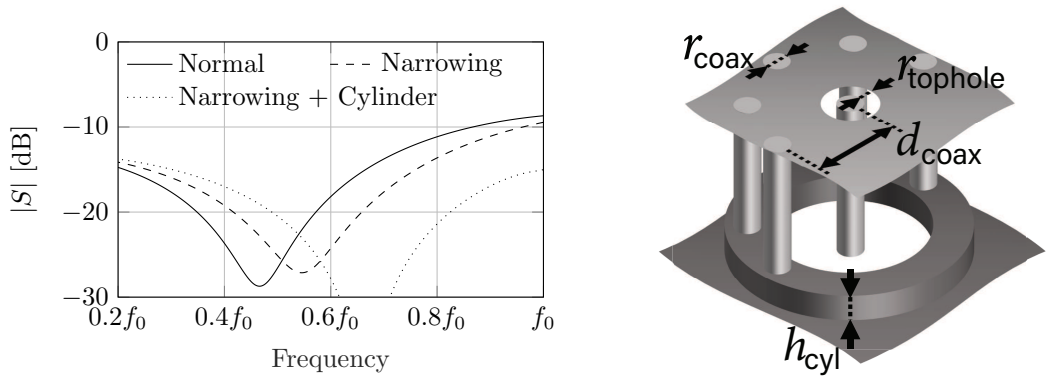

Figure 5.13: (a) Response of a 63 Ω quarter-wave impedance transformer when loaded with 80 Ω and matched to 50 Ω. The transformer is quarter-wave at $0.6f_0$. (b) Illustration of the cylinder that shortens the integrated coaxial impedance transformer.

right on the edge of the cut in the substrate, and removes the restrictions on the length of the microstrip.

The impedance of the quarter wave matching section is chosen as $Z_{\text{qw}} = \sqrt{Z_1 Z_2} = \sqrt{50 \cdot 80} = 63\,\Omega$. This is implemented in the integrated coaxial line, which has a length of $0.41\lambda_d$, which makes it quarter wave at $0.6f_0$. The microstrip is designed such that it has a line impedance of 80 Ω and has a length of $L_{\text{ms}} = 2\lambda_0/15$. In this simulation, the vias that are used to move the cavity resonance are included at a distance of $d_{\text{via}} = 2\lambda_0/15$, as they also reduce the current path length. Fig. 5.13a shows the reflection coefficient when this feed is loaded with 80 Ω and matched to 50 Ω. It is seen that the best matching is obtained at $0.46f_0$ instead of the expected $0.6f_0$. The parameters used in this simulation are shown in Table A.15. The patch and third section of the microstrip are not present in this simulation.

This shift is caused by the discontinuity at the transition from the integrated coaxial line to the microstrip line, where the field must squeeze from the wide coaxial line to the narrow microstrip line. To compensate for this, the microstrip section from the coaxial to the edge of the cavity is narrowed to $\lambda_0/300$. The effect of this is shown in Fig. 5.13a, where the best matching is now obtained at $0.55f_0$. However, it is seen that the matching at f_0 is still poor, which can be improved by shifting the point of best matching to an even higher frequency. This is done by extending the 50 Ω coaxial line at the ground plane, which is illustrated in Fig. 5.13b.

The effect of adding this cylinder is shown in Fig. 5.13a, where $L_{\text{cyl}} = 0.121\lambda_d$, reducing the length of the integrated coaxial section by 30%. This shifts the point of optimal matching to $0.66f_0$ and makes it so that the matching of the feed when loaded with 80 Ω and matched to 50 Ω is now below −13.8 dB across the band. The parameters used in this simulation are shown in Table A.16.

5.5 Final Design

The final design is obtained by following the steps towards a dual-polarized design in Chapter 4, and then introducing the Rogers RO4350B™ substrate, from which part is removed, as shown in Fig. 5.7c. The matching at this point, when the array is still without feeding structure, is shown first to allow comparison of the performance of the design with and without feeding structure. After this, feeding structure is introduced in three steps, starting with the section of the microstrip that is in the feeding gap, then the capacitive patch, and finally the rest of the microstrip and the integrated coaxial impedance transformer.

Between each of these steps the design is optimized such that the obtained matching is balanced

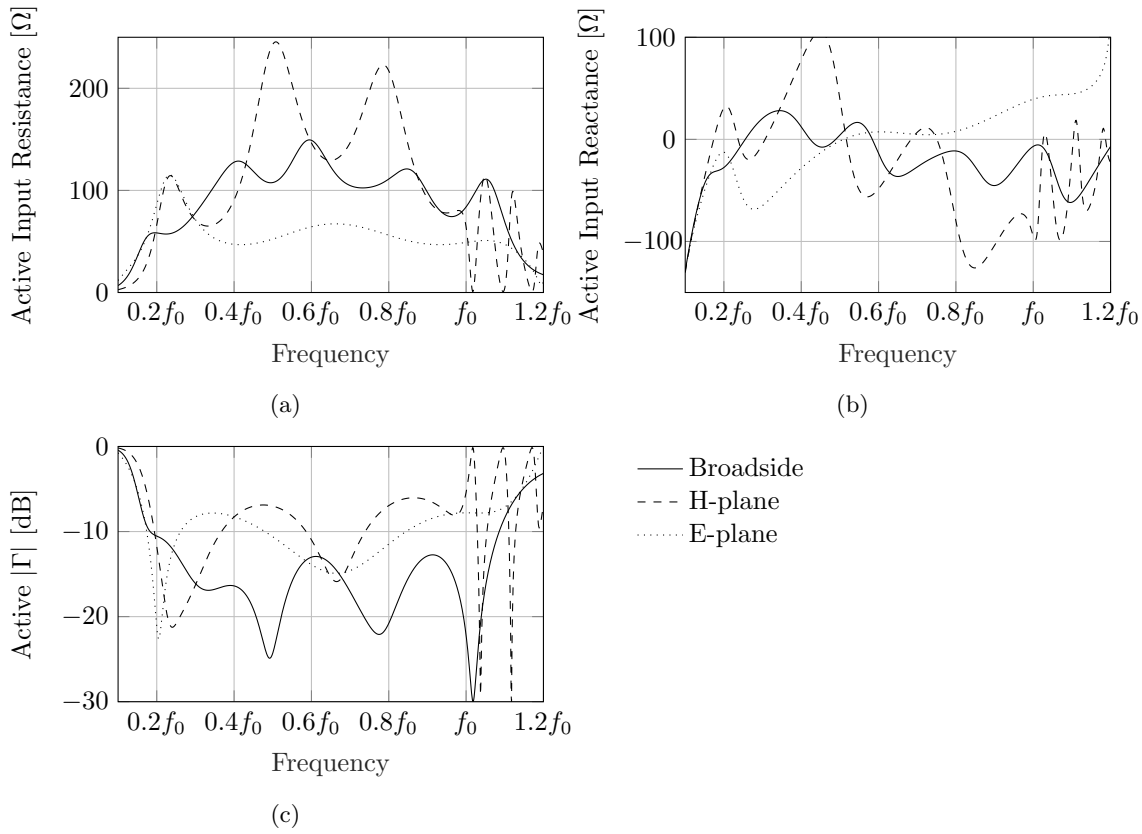

Figure 5.14: Matching performance when scanning the connected array loaded with a 4-section 8-layer 377-94 Ω Chebyshev ADL transformer with a Rogers 4350B$^{\text{TM}}$ substrate with cavity and vias. (a) Real and (b) imaginary input impedance, (c) reflection coefficients when matched to 96 Ω.

across both planes, and is below −10 dB across the band at broadside. This is done to ensure that the optimization process for the next step starts as close as possible to its optimal, reducing the complexity of each optimization step.

The final design uses the 377-94 Ω Chebyshev ADL impedance transformer introduced in Section 4.3, for which the parameters are shown in Table A.9 in Appendix A. The parameters of the slot and substrate are shown in Table A.17, and the parameters of the feeding structure are shown in Table A.18.

5.5.1 With Ideal Delta-Gap Feed

The final design is first shown without feed to show the difference that the introduction of the feeding structure makes on the matching performance for broadside and scanning along the H- and E-plane. Fig. 5.14 shows the active input impedance and the active reflection coefficient that is achieved at this point in the design process.

At broadside the reflection coefficient is seen to be below −10.5 dB across the $0.2f_0$ to f_0 bandwidth, whereas the H- and E-plane are below −6 dB and −7.8 dB, respectively. It can be noted that the matching is not well-balanced between the two planes, which is due to the fact that improving the H-plane matching at the low frequency worsens the high-frequency matching of the H-plane.

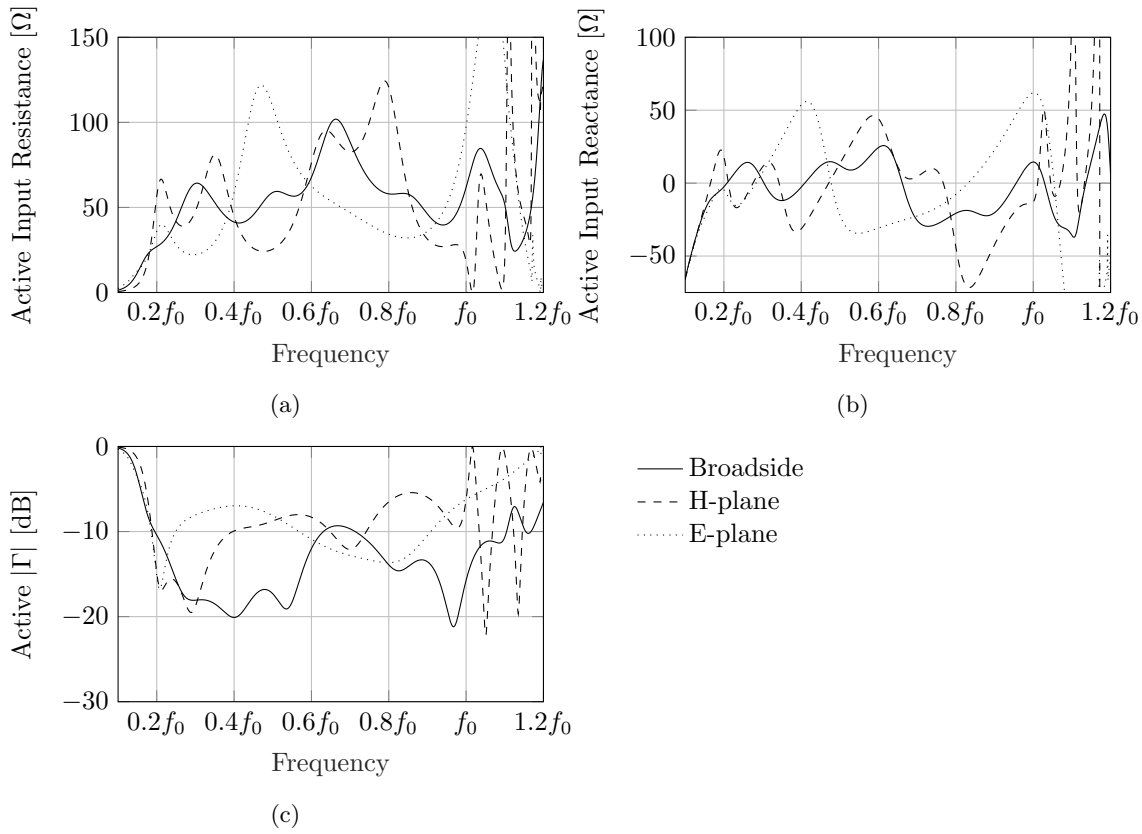

Figure 5.15: Matching performance when scanning the connected array loaded with a 4-section 8-layer 377-94 Ω Chebyshev ADL transformer with a Rogers 4350B^{TM} substrate with cavity, vias and the feeding network. (a) Real and (b) imaginary input impedance, (c) reflection coefficients when matched to 50 Ω.

5.5.2 With Feeding Structure

With the parameters for the ADL, the slot plane, the cavity and the vias known, the feeding structure that was shown in Section 5.4 is introduced. This feeding structure will transform the impedance seen at the slot (around 80 Ω) plane to the impedance of the 50 Ω coaxial feeding line.

The behavior of this antenna array is first shown in terms of its matching performance, where the active input impedance seen at the ground plane is shown, as well as the active reflection coefficient when the array is matched to 50 Ω. This is shown in Fig. 5.15, where it is seen that the reflection coefficient is below −10 dB across most of the band, but hits −9.3 dB at $0.67f_0$. The H- and E-plane are below −5.4 dB and −6 dB across the $0.2f_0$ to f_0 bandwidth, respectively.

Realized Gain

Fig. 5.16 shows The broadside realized gain, based on the infinite array simulations of the unit cell, is plotted as a function of the frequency in Fig. 5.16. A windowing technique is used to estimate the patterns of a finite array with 32x32 elements. In the same figure, the maximum directivity from the array aperture is also shown, to quantify the efficiency. It is seen that the realized gain of the array is very close the theoretical maximum.

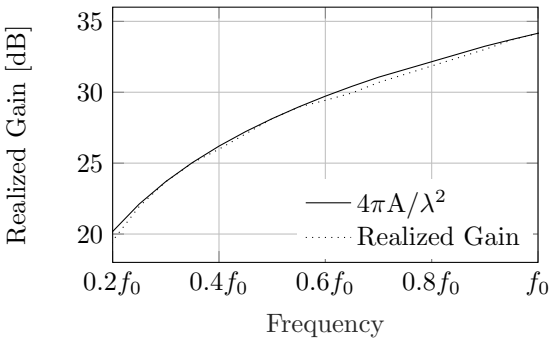

Figure 5.16: Broadside realized gain versus frequency of an array with 32x32 elements, based on the infinite array simulation of the unit cell in Fig. 5.15c. The maximum theoretical directivity is also shown for comparison.

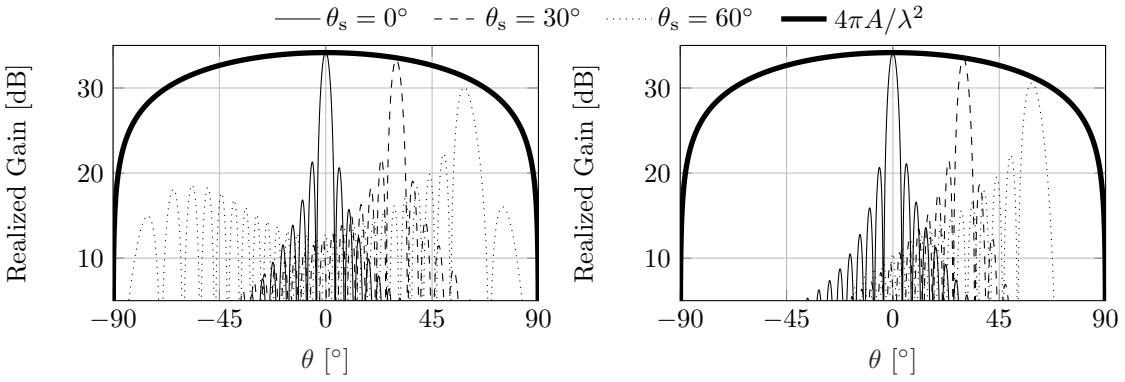

Figure 5.17: Realized gain patterns for an array with 32x32 elements, for scanning in the (a) H- and (b) E-plane of the x-oriented slot, based on the infinite array simulation in Fig. 5.15c. The maximum theoretical directivity, accounting for the $\cos\theta$ dependence of the projected aperture, is also shown for comparison.

Realized Gain Patterns

The behavior of the array when it is scanned is evaluated in Fig. 5.17, which shows the realized gain patterns for broadside and scanning to 30 and 60 degrees in the H- and E-planes. The scan loss is less than 1.5 dB below the ideal $\cos\theta$ profile, which is also shown in the figure.

Cross-Polarization

The cross-polarization in the far field of the array is the ratio of the amount of power that is radiated orthogonal to the desired polarization and the amount radiated in the desired polarization. It is evaluated at a scanning angle of 60° in the diagonal plane ($\phi = 45°$), where the worst cross-polarization is found. It is shown in Fig. 5.18a for both of the orthogonal slots in the array, where it is seen that the cross-polarization starts low and increases with frequency. The cross-polarization increases to 3 dB at f_0, which appears to make the array unsuitable for applications where the polarization purity of signals is important, such as communications. Fortunately, the cross-polarization can be reduced by applying cancellation.

If the array is to be used for polarization-sensitive applications in the $0.8f_0$ to f_0 band, can-

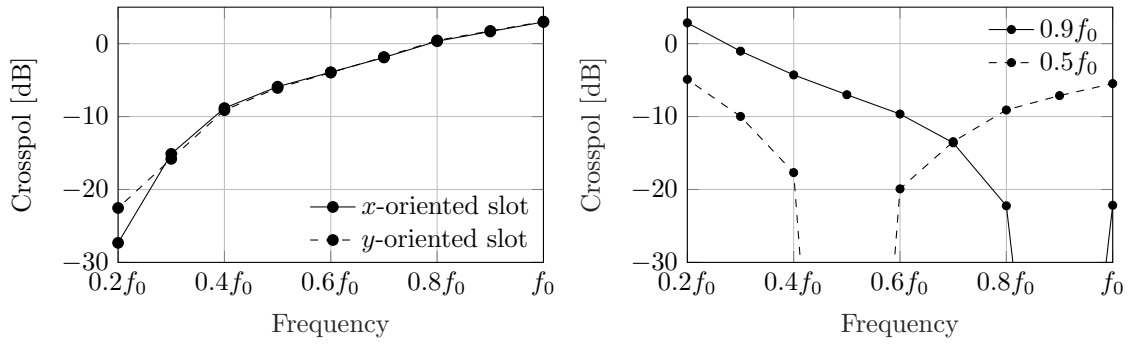

Figure 5.18: Cross-polarization of the array unit cell, given as horizontal/vertical of the Ludwig 3 field components. Cross-polarization is shown (a) without and (b) with cancellation at $0.9f_0$ or $0.5f_0$.

cellation can be applied at $0.9f_0$ to ensure that the cross-polarization in that band is very low. Cross-polarization cancellation can be done in post-processing, where the received signal from the two orthogonal slots is combined such that the co-polarized component of one slot nullifies the cross-polarized component of the other. This requires complete knowledge of the polarization and phase of the emitted field at the frequency at which the cancellation is to be performed. Suppose that it is desired to cancel the horizontally-polarized field component of slot 1 using the horizontally-polarized component of slot 2, assuming a Ludwig 3 coordinate system. Let $a_{1,\mathrm{h}}$ and $\phi_{1,\mathrm{h}}$ be the amplitude and phase of the horizontally-polarized field component of slot 1 at the desired scanning angle, and $a_{2,\mathrm{h}}$ and $\phi_{2,\mathrm{h}}$ those of slot 2. The signal where the cross-polarized component is canceled is the given by

$$s_{\text{canceled}} = s_1 + s_2 \frac{a_{1,\mathrm{h}}}{a_{2,\mathrm{h}}} e^{j(\pi - (\phi_{1,\mathrm{h}} - \phi_{2,\mathrm{h}}))}, \tag{5.7}$$

where s_1 is the signal received by slot 1, and s_2 the signal received by slot 2.

The result of this is shown in Fig. 5.18b, where this cancellation is done at $0.9f_0$. It is seen that the cross-polarized component of the x-oriented slot is below $-22\,\mathrm{dB}$ across the $0.8f_0$ to f_0 bandwidth. This means that the array can be used for polarization-sensitive applications as well.

The origin of this cross-polarization is the rotation of the wave due to the different propagation velocity of the TE- and TM-component of the wave, which follows from the different angular behavior of the permittivity of the ADLs.

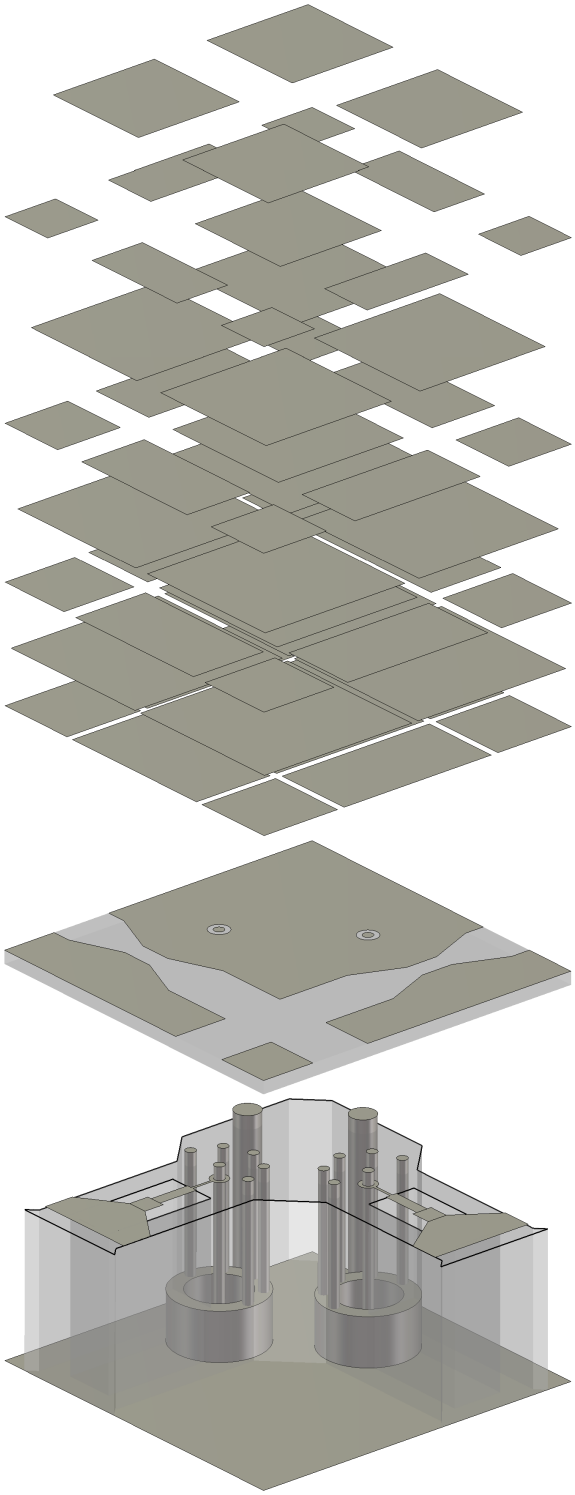

Figure 5.19: Exploded view of the final design, shown in three stages, starting with the ADL, then the slot plane, and finally the substrate with feeding structure.

Chapter 6

Conclusion

6.1 Summary and Conclusions

The objective of this thesis was to further improve and optimize the performance of wideband phased arrays based on the concept of connected slot elements with artificial dielectric superstrates. More specifically the target performance was characterized by an impedance bandwidth of 5:1 and scan range up to 60 degrees for all azimuths.

One of the main advantages of this phased array concept is the availability of closed-form analysis tools for both the radiating connected slots and the artificial dielectric structure. In Chapter 2, all the equations used for the modeling are reported and validated by comparison with commercial solvers.

The analytical tools allow for fast simulations, with minimal computational resources. This enables a synthesis procedure for the design of the artificial dielectric that would be otherwise impractical. This synthesis procedure, described in Chapter 3, is able to create impedance transformers using artificial dielectrics with impedances within 0.2% of the desired values in seconds.

A single-polarized antenna array for a 5:1 bandwidth using such an impedance transformer can be rapidly developed and extended to dual-polarized operation with only minor changes to the geometrical parameters of the slot array. Chapter 4 shows the required steps to obtain this array, as well as the method used to suppress the parallel-plate waveguide mode between the backing reflector and the slot plane.

It is shown in Chapter 5 that the inclusion of the glue layers has little impact on the broadside and E-plane performance, but limits the bandwidth for scanning to 60° on the H-plane to 4.7:1. The inclusion of the PCB material between the backing reflector and the slot plane is shown to not significantly impact performance of the array. The design process of an integrated feeding network with is shown through the design of an impedance transformer with a reflection coefficient of under $-13.8\,\text{dB}$ across the 5:1 bandwidth.

Finally, a complete design is presented of an array with a reflection coefficient below $-5.4\,\text{dB}$ and $6\,\text{dB}$ across the 5:1 bandwidth for scanning to 60° on the H- and E-planes, respectively. For a 32x32 array, based on the infinite array simulations, the broadside realized gain vs frequency is shown to be on average within $0.2\,\text{dB}$ of theoretical maximum directivity. The realized gain is shown to be within $1.5\,\text{dB}$ of the ideal gain when scanning to 60° on the H- or E-plane. The cross-polarization of the array is shown to increase up to $3\,\text{dB}$, and a cancellation strategy is shown to reduce this to below $-20\,\text{dB}$ across part of the bandwidth.

6.2 Future Work

This thesis shows a design methodology using the analytical expressions developed by the TeraHertz Sensing Group, and uses a commercial solver to extend this design to allow for dual-polarized operation. There are several possible future analyses that could improve both this design process and the design that is offered:

- The cross-polarization of the shown design reaches up to 3 dB, which makes cancellation a necessity for polarization sensitive applications. The development of an ADL that has equal angular behavior of the permittivity for the TE- and TM-component would make this cross-polarization closer to that of a homogeneous material. An option for this would be to introduce a vertical component to the metal that is used in the ADL, such that the vertical component of the TM-wave for high scanning still interacts with the metal.
- The analytical model used to design the ADL and the slot array is currently only suitable for a single-polarized array, and commercial solvers are required to continue the design. It would be useful if a model were developed that can be used to design a dual-polarized connected slot array.
- The guided wave that appears just beyond f_0 is the main limiting factor of the bandwidth in the current design. Further investigation into the appearance of this guided wave could yield insights into how to alter the design such that the guided wave is pushed to a higher frequency. This would facilitate development of an array with a higher bandwidth.
- The current design assumes that the array is infinite along the x- and y-axis, and a windowing technique is used to obtain the patterns and realized gain. A study into the effect of having a finite number of finite slots is required.
- A graphical design tool could be implemented based on the methodologies described in this report, enabling the design of a connected slot array loaded with ADLs without requiring implementation of all the equations that are used to model the array and ADLs.

Bibliography

[1] J. Langley, P. Hall, and P. Newham, "Balanced antipodal vivaldi antenna for wide bandwidth phased arrays," *IEE Proceedings-Microwaves, Antennas and Propagation*, vol. 143, no. 2, pp. 97–102, 1996.

[2] Y. Yao, M. Liu, W. Chen, and Z. Feng, "Analysis and design of wideband widescan planar tapered slot antenna array," *IET microwaves, antennas & propagation*, vol. 4, no. 10, pp. 1632–1638, 2010.

[3] E. W. Reid, L. Ortiz-Balbuena, A. Ghadiri, and K. Moez, "A 324-element vivaldi antenna array for radio astronomy instrumentation," *IEEE Transactions on Instrumentation and Measurement*, vol. 61, no. 1, pp. 241–250, Jan 2012.

[4] Y. Lubin and A. Hessel, "Wide-band, wide-angle microstrip stacked-patch-element phased arrays," *IEEE transactions on antennas and propagation*, vol. 39, no. 8, pp. 1062–1070, 1991.

[5] A. T. Wang, K. M. Lee, and R. S. Chu, "Planar low profile, wideband, wide-scan phased array antenna using a stacked-disc radiator," Mar. 9 1999, uS Patent 5,880,694.

[6] A. A. Eldek, "Design of double dipole antenna with enhanced usable bandwidth for wideband phased array applications," *Progress In Electromagnetics Research*, vol. 59, pp. 1–15, 2006.

[7] H. Wheeler, "Simple relations derived fom a phased-array antenna made of an infinite current sheet," *IEEE Transactions on Antennas and Propagation*, vol. 13, no. 4, pp. 506–514, July 1965.

[8] B. A. Munk, *Finite antenna arrays and FSS*. John Wiley & Sons, 2003.

[9] J. P. Doane, K. Sertel, and J. L. Volakis, "A wideband, wide scanning tightly coupled dipole array with integrated balun (tcda-ib)," *IEEE Transactions on Antennas and Propagation*, vol. 61, no. 9, pp. 4538–4548, 2013.

[10] D. K. Papantonis and J. L. Volakis, "Dual-polarized tightly coupled array with substrate loading," *IEEE Antennas and Wireless Propagation Letters*, vol. 15, pp. 325–328, 2016.

[11] D. Cavallo, A. Neto, G. Gerini, A. Micco, and V. Galdi, "A 3- to 5-ghz wideband array of connected dipoles with low cross polarization and wide-scan capability," *IEEE Transactions on Antennas and Propagation*, vol. 61, no. 3, pp. 1148–1154, March 2013.

[12] Y. Chen, S. Yang, and Z.-P. Nie, "A novel wideband antenna array with tightly coupled octagonal ring elements," *Progress In Electromagnetics Research*, vol. 124, pp. 55–70, 2012.

[13] J. A. Kasemodel, C. Chen, and J. L. Volakis, "Wideband planar array with integrated feed and matching network for wide-angle scanning," *IEEE Transactions on Antennas and Propagation*, vol. 61, no. 9, pp. 4528–4537, Sep. 2013.

[14] W. H. Syed, D. Cavallo, H. Thippur Shivamurthy, and A. Neto, "Wideband, wide-scan planar array of connected slots loaded with artificial dielectric superstrates," *IEEE Transactions on Antennas and Propagation*, vol. 64, no. 2, pp. 543–553, Feb 2016.

[15] G. Oltman, "The compensated balun," *IEEE Transactions on Microwave Theory and Techniques*, vol. 14, no. 3, pp. 112–119, March 1966.

[16] D. Cavallo, "Connected array antennas: Analysis and design," 2011.

[17] W. Syed, "On the control of surface waves in integrated antennas: Analysis and design exploiting artificial dielectric layers," 2015.

[18] D. Cavallo, W. H. Syed, and A. Neto, "Closed-form analysis of artificial dielectric layers—part i: Properties of a single layer under plane-wave incidence," *IEEE Transactions on Antennas and Propagation*, vol. 62, no. 12, pp. 6256–6264, Dec 2014.

[19] ——, "Closed-form analysis of artificial dielectric layers—part ii: Extension to multiple layers and arbitrary illumination," *IEEE Transactions on Antennas and Propagation*, vol. 62, no. 12, pp. 6265–6273, Dec 2014.

[20] D. Cavallo and C. Felita, "Analytical formulas for artificial dielectrics with nonaligned layers," *IEEE Transactions on Antennas and Propagation*, vol. 65, no. 10, pp. 5303–5311, Oct 2017.

[21] D. Cavallo and R. M. van Schelven, "Closed-form analysis of artificial dielectric layers with non-periodic characteristics," in *2019 13th European Conference on Antennas and Propagation (EuCAP)*, March 2019, pp. 1–5.

[22] A. Neto, D. Cavallo, G. Gerini, and G. Toso, "Scanning performances of wideband connected arrays in the presence of a backing reflector," *IEEE Transactions on Antennas and Propagation*, vol. 57, no. 10, pp. 3092–3102, 2009.

[23] A. Neto and J. J. Lee, "Ultrawide-band properties of long slot arrays," *IEEE Transactions on Antennas and Propagation*, vol. 54, no. 2, pp. 534–543, Feb 2006.

[24] C. Felita, "Analytical study of artificial dielectrics composed of non-aligned layers," 2017.

[25] D. M. Pozar, *Microwave engineering.* John Wiley & Sons, 2009.

[26] D. Cohen and R. Shavit, "Bi-anisotropic metamaterials effective constitutive parameters extraction using oblique incidence s-parameters method," *IEEE Transactions on Antennas and Propagation*, vol. 63, no. 5, pp. 2071–2078, May 2015.

[27] Cst microwave studio. [Online]. Available: http://www.cst.com/

[28] "Rohacell® 31 hf," https://www.rohacell.com/product/rohacell/en/products-services/rohacell-hf/.

[29] "Dupont™ pyralux® ap," https://www.dupont.com/products/pyralux-ap.html.

[30] "Cuclad® 6250," https://www.rogerscorp.com/acs/products/1096/CuClad-6250-Bonding-Film.aspx.

[31] "Rogers ro4350b™," https://www.rogerscorp.com/acs/products/55/RO4350B-Laminates.aspx.

[32] "Coaxial cable: It's not just a piece of wire." https://www3.nd.edu/ wzech/CoaxialTransmissionLine.pdf.

Appendix A

Simulation Parameters

This appendix lists the parameters used in the simulations done in this thesis.

Table A.1: Parameters used in the optimized design shown in Fig. 4.5.

Parameter	Value	Description
d_x	$0.45\lambda_0$	Unit cell size
d_y	$0.45\lambda_0$	Unit cell size
w_s	$0.18\lambda_0$	Slot width
δ_s	$0.2\lambda_0$	Feed length
h_{BR}	$0.2\lambda_0$	Backing reflector distance
C	2 pF	Series capacitance

Table A.2: Parameters of the connected slot array used to validate the combination of the connected slots and an ADL transformer, which is shown in Fig. 2.12.

Parameter	Value	Description
d_x	$0.45\lambda_0$	Unit cell size
d_y	$0.45\lambda_0$	Unit cell size
w_s	$0.18\lambda_0$	Slot width
δ_s	$0.2\lambda_0$	Feed length
h_{BR}	$0.2\lambda_0$	Backing reflector distance
C_{feed}	1.5 pF	Series feed capacitance
Walls	Yes	Vertical walls between slots

Table A.3: Parameters of an 8-section 9-layer 377-100 Ω exponential transformer with a total electric height of $2\lambda_0$. The ADL unit cell size is $p = 0.225\lambda_0$.

Section	$Z_{section}$	$\varepsilon_{r,des}$	d_z (λ_0)	w (λ_0)	s (p)	N
1	108.6477	12.0398	0.0360	0.0269	0.5	2
2	128.2514	8.6405	0.0850	0.0068	0.5	1
3	151.3922	6.2009	0.1004	0.0116	0.5	1
4	178.7084	4.4501	0.1186	0.0199	0.5	1
5	210.9533	3.1937	0.1398	0.0327	0.5	1
6	249.0162	2.2920	0.1652	0.0524	0.5	1
7	293.9470	1.6448	0.1950	0.0842	0.5	1
8	346.9848	1.1804	0.2302	0.1431	0.5	1

Table A.4: Parameters of a 5-section 377-50 Ω exponential transformer with a total electric height of $2\lambda_0$. The ADL unit cell size is $p = 0.225\lambda_0$.

Section	$Z_{section}$	$\varepsilon_{r,des}$	d_z (λ_0)	w (λ_0)	s (p)	N
1	61.1936	37.9533	0.0162	0.0399	0.5	4
2	91.6597	16.9163	0.0324	0.0160	0.5	3
3	137.2937	7.5398	0.0728	0.0097	0.5	2
4	205.6472	3.3606	0.2182	0.0114	0.5	1
5	308.0314	1.4979	0.3268	0.0691	0.5	1

Table A.5: Parameters of a 5-section 377-50 Ω exponential transformer with a total electric height of $2\lambda_0$, where each section has at least 2 metal layers. The ADL unit cell size is $p = 0.225\lambda_0$.

Section	$Z_{section}$	$\varepsilon_{r,des}$	d_z (λ_0)	w (λ_0)	s (p)	N
1	61.1936	37.9533	0.0162	0.0399	0.5	4
2	91.6597	16.9163	0.0324	0.0160	0.5	3
3	137.2937	7.5398	0.0728	0.0097	0.5	2
4	205.6472	3.3606	0.1091	0.0335	0.5	2
5	308.0314	1.4979	0.1634	0.1013	0.5	2

Table A.6: Parameters of an 8-section 377-50 Ω exponential transformer with a total electric height of $2\lambda_0$. The ADL unit cell size is $p = 0.225\lambda_0$.

Section	$Z_{section}$	$\varepsilon_{r,des}$	d_z (λ_0)	w (λ_0)	s (p)	N
1	56.7290	44.1623	0.0125	0.0661	0.5	3
2	73.0256	26.6509	0.0242	0.0174	0.5	2
3	94.0037	16.0832	0.0312	0.0244	0.5	2
4	121.0084	9.7058	0.0401	0.0321	0.5	2
5	155.7708	5.8572	0.1032	0.0087	0.5	1
6	200.5187	3.5347	0.1330	0.0211	0.5	1
7	258.1223	2.1331	0.1712	0.0493	0.5	1
8	332.2701	1.2873	0.2204	0.1163	0.5	1

Table A.7: Parameters of an 8-section 377-80 Ω exponential transformer with a total electric height of $2\lambda_0$. The ADL unit cell size is $p = 0.225\lambda_0$.

Section	$Z_{section}$	$\varepsilon_{r,des}$	d_z (λ_0)	w (λ_0)	s (p)	N
1	88.1389	18.2948	0.0292	0.0153	0.5	2
2	106.9850	12.4170	0.0355	0.0297	0.5	2
3	129.8607	8.4277	0.0431	0.0356	0.5	2
4	157.6279	5.7200	0.1046	0.0091	0.5	1
5	191.3322	3.8823	0.1268	0.0179	0.5	1
6	232.2433	2.6350	0.1540	0.0348	0.5	1
7	281.9022	1.7884	0.1870	0.0658	0.5	1
8	342.1792	1.2138	0.2270	0.1300	0.5	1

Table A.8: Parameters of the slot used in Fig. 4.11.

Parameter	Value	Description
d_x	$0.45\lambda_0$	Unit cell size
d_y	$0.45\lambda_0$	Unit cell size
w_s	$0.1\lambda_0$	Slot width
δ_s	$0.2\lambda_0$	Feed length
h_{BR}	$0.2\lambda_0$	Backing reflector distance
C_{feed}	1 pF	Series feed capacitance
Walls	Yes	Vertical walls between slots

Table A.9: Parameters of a 4-section 8-layer 377-94 Ω Chebyshev transformer with a total electric height of $5\lambda_0/3$. The ADL unit cell size is $p = 0.225\lambda_0$.

Section	$Z_{section}$	$\varepsilon_{r,des}$	d_z (λ_0)	w (λ_0)	s (p)	N
1	128.34	8.63	0.0709	0.0094	0.5	2
2	164.33	5.26	0.0908	0.0202	0.5	2
3	215.65	3.06	0.1192	0.0417	0.5	2
4	276.14	1.86	0.1526	0.0771	0.5	2

Table A.10: Parameters of the slot used in Fig. 4.11.

Parameter	Value	Description
d_x	$0.45\lambda_0$	Unit cell size
d_y	$0.45\lambda_0$	Unit cell size
w_{slot}	$0.1\lambda_0$	Slot width
L_{feed}	$0.2\lambda_0$	Feed length
w_{feed}	$0.1\lambda_0$	Feed width
$L_{\text{feed,out}}$	$0.2\lambda_0$	Feed tapering length
h_{BR}	$0.2\lambda_0$	Backing reflector distance
C_{feed}	1 pF	Series feed capacitance

Table A.11: Parameters of the slot used in Fig. 4.14.

Parameter	Value	Description
d_x	$0.45\lambda_0$	Unit cell size
d_y	$0.45\lambda_0$	Unit cell size
w_{slot}	$0.105\lambda_0$	Slot width
L_{feed}	$0.14\lambda_0$	Feed length
w_{feed}	$0.105\lambda_0$	Feed width
$L_{\text{feed,out}}$	$0.14\lambda_0$	Feed tapering length
h_{BR}	$0.2\lambda_0$	Backing reflector distance
C_{feed}	1.5 pF	Series feed capacitance
r_{via}	$0.033\lambda_0$	Via radius
d_{via}	$0.133\lambda_0$	Distance from via to center of slot

Table A.12: Parameters of the slot used in Fig. 5.6.

Parameter	Value	Description
d_x	$0.45\lambda_0$	Unit cell size
d_y	$0.45\lambda_0$	Unit cell size
w_s	$0.165\lambda_0$	Slot width
δ_s	$0.165\lambda_0$	Feed length
h_{BR}	$0.1\lambda_0$	Backing reflector distance
C_{feed}	N/A	Series feed capacitance
Walls	Yes	Vertical walls between slots

Table A.13: Parameters used for the slot plane in the sweep of various patch areas.

Parameter	Value	Description
d_x	$0.45\lambda_0$	Unit cell size
d_y	$0.45\lambda_0$	Unit cell size
w_{slot}	$0.09\lambda_0$	Slot width
L_{feed}	$0.0433\lambda_0$	Feed length
w_{feed}	$0.0225\lambda_0$	Feed width
$L_{\text{feed,out}}$	$0.1733\lambda_0$	Feed tapering length
h_{BR}	$0.1867\lambda_0$	Backing reflector distance
r_{via}	$0.033\lambda_0$	Via radius
d_{via}	$0.133\lambda_0$	Distance from via to center of slot

Table A.14: Feed parameters for the Chebyshev transformer implemented using the combination of the integrated coaxial line and the microstrip line.

Parameter	Value
r_{tr}	$0.0067\lambda_0$
r_{coax}	$0.0090\lambda_0$
d_{coax}	$0.0533\lambda_0$
$w_{\text{ms,1}}$	$0.0083\lambda_0$
$w_{\text{ms,2}}$	$0.0110\lambda_0$
L_{ms}	$0.2010\lambda_0$
r_{tophole}	$0.0067\lambda_0$
r_{gh}	$0.04\lambda_0$

Table A.15: Feed parameters for the quarter-wave transformer implemented using the integrated coaxial line.

Parameter	Value
r_{tr}	$0.0050\lambda_0$
r_{coax}	$0.0067\lambda_0$
d_{coax}	$0.05\lambda_0$
$w_{\mathrm{ms},1}$	$0.0033\lambda_0$
$w_{\mathrm{ms},2}$	$0.0153\lambda_0$
L_{ms}	$0.0867\lambda_0$
r_{tophole}	$0.0067\lambda_0$
r_{gh}	$0.04\lambda_0$

Table A.16: Feed parameters for the quarter-wave transformer implemented using the integrated coaxial line, which is shortened by introducing a cylinder.

Parameter	Value
r_{tr}	$0.0050\lambda_0$
r_{coax}	$0.0067\lambda_0$
d_{coax}	$0.05\lambda_0$
$w_{\mathrm{ms},1}$	$0.0033\lambda_0$
$w_{\mathrm{ms},2}$	$0.0153\lambda_0$
L_{ms}	$0.0867\lambda_0$
r_{tophole}	$0.0067\lambda_0$
r_{gh}	$0.04\lambda_0$
h_{cyl}	$0.0633\lambda_0$

Table A.17: Slot and substrate parameters for the final design.

Parameter	Value
d_x	$0.45\lambda_0$
d_y	$0.45\lambda_0$
L_{feed}	$0.0433\lambda_0$
$L_{\mathrm{feed,out}}$	$0.1733\lambda_0$
w_{slot}	$0.0800\lambda_0$
w_{feed}	$0.0266\lambda_0$
h_{BR}	$0.2166\lambda_0$
d_{ms}	$0.0169\lambda_0$
w_{cavity}	$0.1666\lambda_0$
$w_{\mathrm{cavity,diag}}$	$0.3666\lambda_0$
w_{cross}	$0.0333\lambda_0$
d_{cross}	$0.0666\lambda_0$
r_{via}	$0.0333\lambda_0$
d_{via}	$0.1333\lambda_0$
C	0.8 pF

Table A.18: Feed parameters for the final design.

Parameter	Value
r_{tr}	$0.0050\lambda_0$
r_{coax}	$0.0067\lambda_0$
d_{coax}	$0.05\lambda_0$
$w_{\mathrm{ms},1}$	$0.0033\lambda_0$
$w_{\mathrm{ms},2}$	$0.0153\lambda_0$
$w_{\mathrm{ms},3}$	$0.0267\lambda_0$
L_{ms}	$0.0867\lambda_0$
$L_{\mathrm{p},1}$	$0.0667\lambda_0$
$L_{\mathrm{p},2}$	$0.0393\lambda_0$
θ_{p}	$55°$
A_{patch}	$0.0084\lambda_0^2$
r_{tophole}	$0.0067\lambda_0$
r_{gh}	$0.04\lambda_0$
h_{cyl}	$0.0633\lambda_0$

Appendix B

Homogenization of a Structure

Homogenization is the process of determining the equivalent permittivity and permeability of a given structure such that a homogeneous dielectric material with those parameters exhibits the same behavior. The permittivity of an arbitrary structure can be determined from its S-parameters [26]. The behavior of a material for plane waves of different polarizations and incident from different angles varies with the permittivity and permeability of the material. Using this relation and the S-parameters of a structure for the TE- and TM-polarization for incident plane waves from broadside and a certain angle θ.

$$\eta^{TE} = \pm\sqrt{\frac{\left(1+S_{11}^{TE}\right)^2 - \left(S_{21}^{TE}\right)^2}{\left(1-S_{11}^{TE}\right)^2 - \left(S_{21}^{TE}\right)^2}}\sec\theta \tag{B.1}$$

$$\eta^{TM} = \pm\sqrt{\frac{\left(1+S_{11}^{TM}\right)^2 - \left(S_{21}^{TM}\right)^2}{\left(1-S_{11}^{TM}\right)^2 - \left(S_{21}^{TM}\right)^2}}\cos\theta \tag{B.2}$$

$$n^{TE} = \sqrt{\left(\frac{\log|\zeta^{TE}| + j\left[\angle\left(\zeta^{TE}\right) + 2\pi m\right]}{-jk_0 d}\right)^2 + \sin^2\theta} \tag{B.3}$$

$$n^{TM} = \sqrt{\left(\frac{\log|\zeta^{TM}| + j\left[\angle\left(\zeta^{TM}\right) + 2\pi \bar{m}\right]}{-jk_0 d}\right)^2 + \sin^2\theta}, \tag{B.4}$$

where m and $\bar{m}$ are integers, d is the height of the structure, and

$$\zeta^{TE} = \frac{S_{21}^{TE}}{1 - S_{11}^{TE}\left(\eta^{TE}\cos\theta - 1\right)/\left(\eta^{TE}\cos\theta + 1\right)} \tag{B.5}$$

$$\zeta^{TM} = \frac{S_{21}^{TM}}{1 - S_{11}^{TM}\left(\eta^{TM}/\cos\theta - 1\right)/\left(\eta^{TM}/\cos\theta + 1\right)}. \tag{B.6}$$

From these values, the permittivity and permeability are extracted using

$$\varepsilon_x = \left.\frac{n^{TE}}{\eta^{TE}}\right|_{\theta=0} \tag{B.7}$$

$$\varepsilon_y = \left.\frac{n^{TM}}{\eta^{TM}}\right|_{\theta=0} \tag{B.8}$$

$$\mu_x = \left.\left(n^{TE}\eta^{TE}\right)\right|_{\theta=0} \tag{B.9}$$

$$\mu_y = \left.\left(n^{TM}\eta^{TM}\right)\right|_{\theta=0}. \tag{B.10}$$

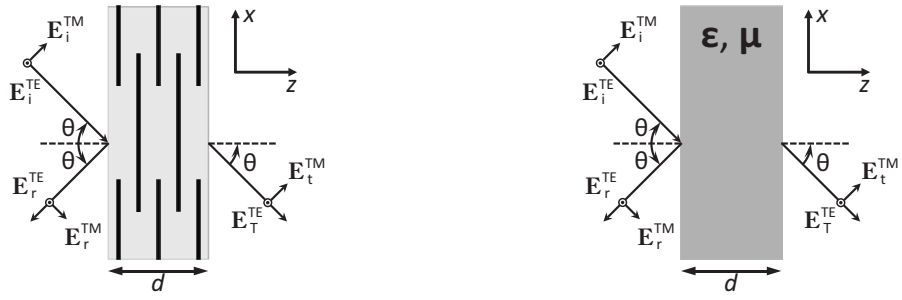

Figure B.1: Example of (a) an ADL slab and (b) its homogeneous equivalent dielectric. Fig. 3.7, repeated here for clarification.

These can not yet be evaluated, as the values of m and $\bar{m}$ are still unknown. These branch indices are chosen by determining two sets of longitudinal parameters, for both ε_z and μ_z given by

$$\varepsilon_z^{(1)} = \varepsilon_x \frac{\sin^2\theta}{\sin^2\theta - \left(n^{TM}\right)^2 + \left(n^{TM}|_{\theta=0}\right)^2} \tag{B.11}$$

$$\varepsilon_z^{(2)} = \frac{\sin^2\theta}{\left(n^{TM}\eta^{TM}\right)|_{\theta=0} - \varepsilon_x / \left(\eta^{TM}\right)^2} \tag{B.12}$$

$$\mu_z^{(1)} = \frac{\sin^2\theta}{\left(n^{TE}/\eta^{TE}\right)|_{\theta=0} - \mu_x / \left(\eta^{TE}\right)^2} \tag{B.13}$$

$$\mu_z^{(2)} = \mu_x \frac{\sin^2\theta}{\sin^2\theta - \left(n^{TE}\right)^2 + \left(n^{TE}|_{\theta=0}\right)^2}. \tag{B.14}$$

The correct value of m and $\bar{m}$ are found by equating the two sets of expressions

$$\varepsilon_z^{(1)} = \varepsilon_z^{(2)} \tag{B.15}$$

$$\mu_z^{(1)} = \mu_z^{(2)}. \tag{B.16}$$

List of Figures

List of Tables